Modeling AMPA receptor trafficking dynamics during long-term potentiation

Dissertation

zur

Erlangung des Doktorgrades (Dr. rer nat.)

der

Mathematisch-Naturwissenschaftlichen Fakultät

der

Rheinischen Friedrich-Wilhelms-Universität Bonn

vorgelegt von

Surbhit Wagle

aus

Khategaon, Indien

Bonn 2025

Angefertigt mit Genehmigung der Mathematisch-Naturwissenschaftlichen Fakultät der Rheinischen Friedrich-Wilhelms-Universität Bonn

Gutachterin/Betreuerin: Prof. Dr. Tatjana Tchumatchenko

Gutachter: Prof. Dr. rer. nat. Michael Pankratz

Tag der Promotion: 12.05.2025

Erscheinungsjahr: 2025

Summary

Neurons are excitable cells with a highly complex morphology. Their dendritic arbors stretch across thousands of micrometers and house tiny protrusion-like structures called "Spine", where they receive signals from other neurons. This signal transfer occurs when the neurotransmitters released from the presynaptic neuron bind to the receptors localized in the post-synaptic density in the spine head. One of the most essential types of receptors is the α-amino-3-hydroxy-5-methyl-4-isoxazolepropionic acid receptor (AMPAR)s. They mediate fast-excitatory currents necessary for information transfer from one neuron to another. Given the extensive dendritic structure, localizing AMPARs and modulating their copy numbers at each spine pose a tremendous logistical challenge for the neuron to ensure its function. This thesis aims to provide novel insight into how neurons solve this logistical challenge throughout the dendrite and how their copy numbers are regulated to change information transfer efficiency via synaptic plasticity.

Modern microscopy techniques and advanced labeling methods allow the investigation of molecular composition and visualization of individual molecules in neuronal compartments such as dendrites and spines. However, analyzing this data is a challenging task. Tracking molecules over large distances and determining their precise location within specific cellular compartments remains algorithmically complex. This thesis also provides a new data analysis pipeline to tackle these challenges by comprehensive and reproducible analysis of fluorescent-based imaging data.

In Chapter 2, I introduce a novel tool we call "SpyDen", which I built to efficiently and robustly analyze neuronal imaging data and extract biologically meaningful information from them. I developed this tool with a former master's student, Jean Philip Heino Filling, and a former Postdoc, Maximilian Eggl. In section 2.1, I describe the data analysis pipeline that SpyDen uses for systemic data analysis. In section 2.2 and section 2.3, I discuss the algorithmic solutions I implemented to trace the dendritic tree and analyze fluorescently bright puncta-like signals from images. These punctated singles originate from mRNA or protein of interest.

In Chapter 3, I introduce trafficking processes, such as diffusion, active transport, and degradation, utilized by a neuron to distribute AMPAR throughout the dendritic tree in section 3.1. Then, in section 3.2, I discuss the results from the analysis of fluorescent in-situ hybridization data imaged by my collaborators, Dr. Anne-Sophie Hafner, for AMPAR subunits *Gria1* and

Gria2 and show that the new AMPARs subunits are produced predominantly in the cell somata. In section 3.3, I analyze the protein antibody labeling data on the AMPAR subunit GluA2 and observe a uniform distribution of this subunit in the first $100\mu m$. Initially, these results are surprising as proteins predominantly synthesized in the soma show a decreasing protein density in the dendrites. In section 3.4, I introduce a new mathematical model that includes the global trafficking mechanism to explain the differences between mRNA and protein density of AMPARs. Mainly, I find that biased active transport of these receptors can lead to a uniform distribution in the first $100\mu m$ and an increase in their density, a phenomenon termed distance-dependent scaling of AMPARs, which is reported in the literature but never fully understood mechanistically. Next, in section 3.5, I extend my model, introduced in section 3.4, to model the three functionally separate populations of AMPARs, namely, the AMPARs in the neuronal plasma membrane, intracellular stores, and the post-synaptic density (PSD). Then, I analyze the protein antibody labeling data imaged by my collaborator, Maximilian Ken Kracht, where the surface and intracellular population of GluA2-containing AMPARs were labeled separately in the same neurons. My analysis reveals that 70% of the total GluA2-containing AMPARs are stored in an intracellular pool. Moreover, half of the GluA2 receptors on the neuronal surface are immobilized at the PSD, serving a functional role, while the other half is a mobile pool in the extra-synaptic space.

In Chapter 4, I introduce the experimental observation highlighting the differences in responses of two main AMPAR subtypes: the GluA1-homomeric AMPAR and GluA2-containing AMPARs. I re-analyze the reported data from two published studies that utilized comparable chemical LTP induction methods to quantify their behavior. In Section 4.1, I show that the response of GluA1-homomeric AMPARs can be explained by a fast change in their exocytosis rate. However, the same changes do not explain the slow response of GluA2-containing AMPARs. An extensive literature review suggests that AMPAR auxiliary, Cornichon family AMPA receptor auxiliary protein 2 (CNIH-2) can be the key to explaining these differences in AMPAR subtype responses. In sections 4.2 and 4.3, I discuss the analysis of fluorescent in-situ hybridization for *Cnih2* mRNA and FUNCTA-PLA against CNIH-2 protein imaged by my collaborator, Dr. Anne-Sophie Hafner. My analysis shows that, unlike the mRNA for AMPAR itself, the mRNA for auxiliary subunit CNIH-2 gets locally translated in the neuronal dendrites, and the rate of its local translation in the dendrite increases upon plasticity induction. In section 4.4, I show that when CNIH-2 transcripts are knocked down using the shRNA strategy, hence

reducing its protein level, the surface insertion of GluA2-containing AMAPR reduces while that of GluA1-homomer remains unaffected. In section 4.5, I introduce a model of CNIH-2 protein density to study their steady-state distribution and response to an increase in local and somatic translation rates. Finally, in section 4.6, I integrate the model for CNIH-2 with my three-population mathematical model of AMPARs (introduced in section 3.5) to explain the changes in GluA2-containing AMPARs. I show that only a prolonged increase in the local synthesis rate of CNIH-2 could match the slow and persistent increase in GluA2-containing AMPAR, as reported in published experimental works.

Zusammenfassung

Deutsche Übersetzung

Neuronen sind erregbare Zellen mit einer sehr komplexen Morphologie. Ihre dendritischen Verzweigungen erstrecken sich über mehrere tausend Mikrometer und enthalten winzige, vorstehende Strukturen, die Dorn (Spines) genannt werden, an denen sie Signale von anderen Neuronen empfangen. Diese Signalübertragung erfolgt, wenn die vom präsynaptischen Neuron freigesetzten Neurotransmitter an den Rezeptoren anbinden, die in der postsynaptischen Dichte am Kopf des Dornes lokalisiert sind. Eine der wesentlichen Arten von Rezeptoren sind die α-Amino-3-Hydroxy-5-Methyl-4-Isoxazolpropionsäure-Rezeptoren (AMPA-Rezeptoren). Sie vermitteln schnelle exzitatorische Ströme, die für die Informationsübertragung von einem Neuron zum anderen notwendig sind. Angesichts der stark verzweigten Struktur der Dendriten stellt die Lokalisierung von AMPARs und die Regulierung ihrer Kopienzahl an jedem Dorn eine enorme logistische Herausforderung für das Neuron dar, um seine Funktion zu gewährleisten. Ziel dieser Arbeit ist es, neue Einblicke zu bieten, wie Neuronen diese logistische Herausforderung im gesamten Dendriten lösen und wie ihre Kopienzahl reguliert wird, um die Effizienz der Informationsübertragung durch einen Prozess, der als synaptische Plastizität bezeichnet wird, zu verändern. Moderne Mikroskopietechniken und fortgeschrittene Markierungsverfahren ermöglichen die Untersuchung der molekularen Zusammensetzung und die Visualisierung einzelner Moleküle in neuronalen Kompartimenten wie Dendriten und Dornen. Die Analyse dieser Daten stellt jedoch eine groSSe Herausforderung dar. Die Verfolgung von Molekülen über groSSe Entfernungen und die Bestimmung ihrer genauen Position innerhalb spezifischer zellulärer Kompartimente bleibt algorithmisch komplex. In dieser Arbeit wird eine neue Datenanalyse-Pipeline entwickelt, um diese Herausforderungen durch eine umfassende und reproduzierbare Analyse von Fluoreszenz-basierten Bildgebungsdaten zu bewältigen. Im zweiten Kapitel wird ein von mir entwickeltes neuartiges Tool namens SpyDen vorgestellt, um neuronale Bildgebungsdaten effizient und robust zu analysieren und biologisch aussagekräftige Informationen aus ihnen zu extrahieren. Dieses Tool wurde in Zusammenarbeit mit einem ehemaligen Masterstudenten, Jean Philip Heino Filling, und einem ehemaligen Postdoktoranden, Maximilian Eggl, entwickelt. Im Abschnitt 2.1 beschreibe ich die Datenanalyse-Pipeline, die SpyDen für die systemische Datenanalyse verwendet. In den Abschnitten 2.2 und 2.3 er-

läutere ich die von mir entwickelten algorithmischen Lösungen zur Verfolgung des dendritischen Baums und zur Analyse fluoreszierende punktartige Signale aus Bildern. Diese punktartigen Einzelsignale stammen von der mRNA oder dem Protein von Interesse. Im dritten Kapitel, im Abschnitt 3.1 wurden Traffickingprozesse wie Diffusion, aktiven Transport und Abbau vorgestellt, die ein Neuron nutzt, um AMPAR im gesamten dendritischen Baum zu verteilen. Im Abschnitt 3.2 werden die Daten der fluoreszierenden In-situ-Hybridisierung analysiert, die von meiner Kollaboratorin Dr. Anne-Sophie Hafner für die AMPAR-Untereinheiten Gria1 und Gria2 aufgenommen wurden, und die Analyse zeigt, dass die neuen AMPAR-Untereinheiten vorwiegend in Zellsomata produziert werden. Im Abschnitt 3.3 werden die Daten zur Markierung der AMPAR-Untereinheit GluA2 mit Protein-Antikörpern analysiert und dabei wird eine gleichmäSSige Verteilung dieser Untereinheit in den 100 μm beobachtet. Diese Ergebnisse sind zunächst unerwartet, denn Proteine, die überwiegend im Soma synthetisiert werden, zeigen eine abnehmende Proteindichte in den Dendriten. Im Abschnitt 3.4 wird ein neues mathematisches Modell eingeführt, das den globalen Trafficking-Mechanismus einbezieht, um die Unterschiede zwischen mRNA- und Proteindichte von AMPARs zu erklären. Vor allem kommt dabei heraus, dass ein einseitiger aktiver Transport dieser Rezeptoren zu einer gleichmäSSigen Verteilung in den ersten 100 μm und einer Zunahme ihrer Dichte führen kann, ein Phänomen, das als entfernungsabhängige Skalierung von AMPARs bezeichnet wird und über das in der Literatur bereits berichtet wird, das aber mechanistisch nie vollständig verstanden wurde. Als Nächstes wird im Abschnitt 3.5 das im Abschnitt 3.4 vorgestellte Modell erweitert, um die drei funktionell getrennten Populationen von AMPARs zu modellieren, nämlich die AMPARs in der neuronalen Plasmamembran, den intrazellulären Speichern und der postsynaptischen Dichte (PSD). Dann analysiere ich Daten zur Markierung von Protein-Antikörpern, die von meinem Kollaborator Maximilian Ken Kracht aufgenommen wurden, wobei die Oberfläche und die intrazelluläre Population von GluA2-haltigen AMPARs in denselben Neuronen getrennt markiert wurden. Meine Analyse ergibt, dass 70 % der gesamten GluA2-haltigen AMPARs in einem intrazellulären Pool gespeichert sind. Darüber hinaus ist die Hälfte der GluA2-Rezeptoren auf der neuronalen Oberfläche an der PSD immobilisiert und erfüllt dort eine funktionelle Aufgabe, während die andere Hälfte ein mobiler Pool im extra-synaptischen Raum ist. Im vierten Kapitel stelle ich die experimentellen Beobachtungen vor, die die Unterschiede in den Reaktionen der beiden wichtigsten AMPAR-Subtypen, nämlich der GluA1-homomeren AMPARs und der GluA2-haltigen AMPARs, hervorheben. Um ihr Verhalten zu quantifizieren, analysiere

ich erneut die Daten aus zwei bereits veröffentlichten Studien, die vergleichbare chemische LTP-Induktionsmethoden verwendet haben. Im Abschnitt 4.1 zeigt sich, dass die Reaktion der GluA1-homomeren AMPARs durch eine schnelle Änderung ihrer Exozytoserate erklärt werden kann. Die gleichen Veränderungen erklären jedoch nicht die langsame Reaktion von GluA2-haltigen AMPARs. Eine umfassende Literaturrecherche ergibt, dass der AMPAR-begleitendes Protein CNIH-2 der Schlüssel zur Erklärung dieser Unterschiede in den Reaktionen der AMPAR-Subtypen sein kann. In den Abschnitten 4.2 und 4.3 beschreibe ich die Analyse von fluoreszierender In-situ-Hybridisierung für *Cnih2* mRNA und FUNCTA-PLA gegen das CNIH-2-Protein analysiert, das von meiner Kollaboratorin Dr. Anne-Sophie Hafner abgebildet wurde. Meine Analyse zeigt, dass die mRNA für die Hilfsuntereinheit CNIH-2 im Gegensatz zur mRNA für AMPAR selbst lokal in den neuronalen Dendriten translatiert wird, und dass die Rate ihrer lokalen Translation im Dendriten bei einer Plastizitätsinduktion zunimmt. In Abschnitt 4.4 wird gezeigt, dass, wenn CNIH-2-Transkripte mit Hilfe der shRNA-Strategie ausgeschaltet werden, was zu einer Verringerung des Proteingehalts führt, die Oberflächeninsertion von GluA2-enthaltenden AMAPR reduziert wird, während die des GluA1-Homomers unbeeinflusst bleibt. Im Abschnitt 4.5 wird dann ein Modell der CNIH-2-Proteindichte eingeführt, um ihre Steady-State-Verteilung und ihre Reaktion auf eine Erhöhung der lokalen und somatischen Translationsraten zu untersuchen. AbschlieSSend werden im Abschnitt 4.6 durch die Integration des Modells für CNIH-2 mit dem mathematischen Drei-Populations-Modell für AMPARs (eingeführt in Abschnitt 3.5) die Veränderungen bei GluA2-haltigen AMPARs erklärt. Durch die Analyse wird sichtbar, dass nur ein anhaltender Anstieg der lokalen CNIH-2-Syntheserate mit dem langsamen und anhaltenden Anstieg der GluA2-enthaltenden AMPARs übereinstimmen kann, sowie es auch in veröffentlichten experimentellen Arbeiten berichtet wird.

Acknowledgements

Embarking on this doctoral journey has been a transformative and wonderful experience for me, and it would not have been so without the support, guidance, and motivation of many individuals and institutions. It is with earnest gratitude that I utilize this opportunity to acknowledge their valuable contributions.

First and foremost, I express my deepest gratitude to my supervisor, Prof. Dr. rer. nat. Tatjana Tchumatchenko, whose patience, expertise, and unfaltering support guided me through the complexities of this research. Your insightful feedback and encouragement throughout the 4 years of my PhD have been vital in shaping both this thesis and my growth as a research scholar. I am equally grateful to my co-supervisor, Prof. Dr. rer. nat. Michael Pankratz, for their valuable input, mentorship, and constructive criticism throughout this journey. I am also greatly grateful to Dr. Nataliya Kraynyukova and Dr. Anne-Sophie Hafner for their dedicated scientific supervision and insightful contributions.

I feel greatly indebted to the faculty and the staff of the Mathematics and Natural Sciences Department at the University of Bonn. Your guidance, encouragement, and provision of resources created an ideal environment for academic growth and excellence. Special thanks to the Promotionsbüro for always being there to assist with administrative duties and to address my queries promptly. I am deeply grateful to the previous host institutions, the Max Planck Institute for Brain Research (MPIBR) and the University of Mainz, where I worked for my PhD project.

To my lab members (current and past), I am immensely grateful for your camaraderie, collaboration, and support. The countless hours we spent discussing ideas, troubleshooting code, and celebrating breakthroughs have been some of the most rewarding and memorable moments of my PhD journey. Your friendship and shared passion for science made even the most exigent days more manageable and inspiring. I am particularly grateful to Ulzii, Janko, Kanaan, Pierre, Cornelius, Jean, Max, Lorenzo, Dario, Albert, Carlos, Rohan, Alexandra, Nestor, Maria, and Sabine for their guidance, humor, and encouragement, which have left a lasting impression on me.

My sincere thanks go to my fellow researchers and colleagues, especially Prof. Dr. Erin Schuman, Prof. Dr. Amparo Acker-Palmer, Maximilian Ken Kracht, for their thought-provoking

discussions and collaborative efforts. I am also thankful to Prof. Dr. Simon Rumpel, Prof. Dr. Stefan Bittner, who served as the members of my thesis committee during my stay at University of Mainz. Your perspectives have broadened my understanding and enriched my academic journey.

I am profoundly grateful to the Collaborative Research Center 1080 for the financial support provided during my PhD. This funding enabled me to carry out my research and attend conferences to share my findings with the academic community.

On a more personal note, I want to express my deepest gratitude to my family. To my parents, Prof. Dr. Pariksha Wagle, my mother, and Prof. Dr. Sunil Wagle, my father, thank you for instilling in me the value of education and for your unconditional love and support throughout my life. To my brothers, Dr. Swapnil Wagle and Susmit Wagle, I thank you for your unwavering belief in my abilities and your unlimited encouragement and understanding during this journey.

A special thanks go to Aishwarya Ketkar for her unreserved faith in my capabilities, which have kept me going, and for helping me with the German translation.

Lastly, I wish to acknowledge the countless hours spent in reflection and perseverance, the moments of doubt that led to growth, and the personal and academic evolution I have undergone during this process. To all who have contributed, directly or indirectly, to this accomplishment, know that your support has left an indelible mark on my life and this thesis.

Thank you all for being part of this journey. This milestone is as much a celebration of your support and encouragement as it is of my academic achievement.

Contents

1. Introduction

Biological neurons are the fundamental building blocks of the nervous system, playing a critical role in information transmission in living organisms. These excitable cells in the brain, peripheral nerves, and spinal cord are responsible for generating and relaying electrical signals that control various physiological processes like sensory perception, motor activity, thoughts, and emotions.

Neuronal signaling occurs through changes in the electrical potential across the cell membrane, such that at resting state, the interior of the cells is maintained at a lower electric potential of -65 mV compared to the exterior of the cell. The exchange of cations by the sodium-potassium (Na^+/K^+) pump helps maintain this voltage gradient. Upon stimulation of excitatory nature, positive current flows in the cell, leading to its depolarization. On the contrary, stimulation of inhibitory nature leads to hyperpolarization of the membrane potential. Naturally, the combined effect of excitatory and inhibitory currents is balanced at the resting state. However, upon external stimulation, an imbalance in the dendritic currents alters the membrane potential at the soma and the Axon initial segment (AIS), a region dense with voltage-gated ion channels critical for action potential, also called spike generation.

As the membrane potential rises at the AIS and crosses a threshold near - 50 mv, the voltage-gated sodium channels open, allowing a rapid influx of Na+ ions that further depolarizes the neuron. As the membrane potential increases, the voltage-gated Na+ channels become inactive after a certain threshold, and the voltage-gated potassium channels open, causing the outflux of K+ ions. This restores the membrane potential to its resting state. This sequence of sharp increase, followed by a sharp decrease in membrane potential, generates an action potential or "spike", which serves as a fundamental electrical signal (Fig. 1.1.B). Once initiated, the action potential propagates along the axons. Local depolarizing triggers voltage-gated channels in the vicinity, ensuring efficient relay of the signal down the long axon. The Myelin sheaths, an insulating coating enabling saltatory conduction, enhance the speed of action potential propagation. Additionally, the action potential jumps between the gaps in the myelin, also known as nodes of Ranvier.

Once an action potential reaches the axon terminals, it triggers the activation of axonal boutons, which facilitates the transfer of information onto the downstream neurons via synapses.

In section section 1.1, I describe the three main neuronal compartments in more detail.

1.1. Neuronal compartments

Neurons typically consist of three major parts. At the cell's core is its cell body or soma, which contains the nucleus and many organelles that manage the cellular function. The second major part of a neuron is its dendrites, which are extensive branches that receive the signals from other neurons. Third are axons, which are long, thin, tube-like processes called the axons that transmit the signals to other neurons or non-neuronal cells such as glands or muscles (Fig. 1.1.A). The signal transmission occurs mainly via two types of connections. First, Synaptic terminals or chemical synapses, where chemical messengers or neurotransmitters are released into the synaptic cleft (the small gap between the presynaptic neuron and the postsynaptic neuron, Fig. 1.1.C)) to communicate with neighboring neurons. The second and less abundant type is electrical synapses, or gap junctions, that are formed at thin gaps between pre- and postsynaptic neurons. The flow of ions in electrical synapses is usually bidirectional.

► The Soma

The soma, or cell body, plays the role of a central compartment of a neuron. Typically, it is spherical with a radius of about $10\mu m$. A bilipid layer surrounds the intracellular milieu in the soma to separate it from the extracellular space. The cell cytoplasm is a solution rich in nutrients, proteins, and various neuronal structures and organelles. The nucleus, smooth and rough endoplasmic reticulum, and the Golgi apparatus are key among these structures. The endoplasmic reticulum plays a crucial role in synthesizing lipids and proteins, with the rough endoplasmic reticulum being particularly notable for its ribosome-studded exterior. For many years, the soma was believed to be the sole site of protein production in neurons. However, this view shifted in the late 1990s when emerging evidence suggested that protein assembly also occurs within the dendritic arbor, challenging the long-held understanding of neuronal protein synthesis [16].

▶ The Dendrites

Dendrites serve as the neuron's primary apparatus for receiving signals from other neurons. These structures exhibit a remarkably diverse and stereotyped morphology, which has been instrumental in classifying different neuron types. Dendritic arbors' unique branching patterns and characteristics provide a basis for categorizing neurons, reflecting their specialized functions and roles within the nervous system. Dendritic trees vary greatly across neuron types, ranging from extensive arbors in pyramidal neurons spanning a few thousand microns to very compact structures, limited to $\approx 100\mu m$ in granule cells. Dendrites are cylindrical structures with a bilipid layer encasing cytoplasm, and mature dendrites feature spine protrusions ($1-2$ per μm) that host synapses [119].

Dendritic radii typically range from $0.1\mu m$ in granule cells to a few micrometers in basal pyramidal dendrites, with some exceptions like crab stomatogastric ganglia neurons reaching $50\mu m$. Dendritic length can refer to the soma-to-tip distance or the inter-branch distance, with this thesis using the latter definition.

The dendritic surface comprises a bilipid layer similar to the soma's, enclosing cytoplasm with various organelles. The endoplasmic reticulum is the largest internal structure, followed by mitochondria. Ribosomes, lysosomes, and proteosomes also play crucial roles in dendritic function.

Dendrites serve to integrate signals from presynaptic neurons arriving within a time window and transmit them to the axon hillock, where action potentials or a spike originate. The diverse morphologies of neurons result from balancing two key factors: maximizing signal transmission efficiency from synapses to the soma and minimizing the metabolic cost associated with dendritic wiring. This balance can explain the variety of dendritic structures observed across different neuron types.

▶ The Axons

Axons are responsible for conducting the action potential generated at the axon hillock to the presynaptic boutons, where the single is transmitted to postsynaptic neurons. Axons are surrounded by a protective myelin sheath formed by oligodendrocytes in the Central Nervous System (CNS) and Schwann cells in the Peripheral Nervous System (PNS). Given the extremely long lengths of the axons, the action potential tends to decrease in strength even in the presence

of a protective myelin sheath. Hence, evolution led to gaps in myelinations, called Node of Renevier (Fig. 1.1.A), rich in voltage-gated ion channels to enable amplification of the electrical signal. These mechanisms support the reliable transmission of information from one neuron to another.

1.2. Synapse and synaptic plasticity

Synapses are specialized structures that enable communication between two neurons. Typically, a synapse comprises a presynaptic axonal bouton that emits the signals in response to spiking in the presynaptic neuron and a postsynaptic neuron that receives the signals, inducing a change in the postsynaptic membrane potential (PSP). The gap between the two neurons, typically in the order of 20-30 nanometers, is called synaptic cleft (Fig. 1.1.C). Upon a presynaptic spike arriving at the axon terminal, voltage-gated Ca^{2+} channels activate, causing a fast influx of Ca^{2+}, triggering the fusion of presynaptic vesicles and leading to neurotransmitter release (Fig. 1.1.C). The released neurotransmitters diffuse across the cleft and bind to specific receptors on the postsynaptic membrane. The binding of neurotransmitters leads to the activation of receptors via conformational change from a closed to open state. Opening of ion channels either directly alters the ion flow or initiates secondary messenger pathways to open other ion channels, allowing either negative (Cl^- causing hyperpolarization, or positive Na^+, causing depolarization) currents to flow.

The resulting local electrical changes spread along the dendrite and reach the axonal initial segment where the cumulative effect of simultaneously arriving signal is sensed. Several factors can modify the signal. For example, Shunting inhibition modifies the signal when current leaks due to ion channel opening caused by overlapping synaptic activation. Attenuation weakens the voltage as it travels due to dendritic resistance, making signals from distal synapses less effective. Temporal dynamics also play a role, as signals from distant dendrites take longer to reach the soma, and the precise timing of multiple depolarizations is critical for triggering a spike. Additionally, voltage-gated ion channels in dendrites can lead to localized dendritic spikes, amplifying synaptic input.

This spatial and temporal transformation of synaptic signals collectively form dendritic computations, which integrate complex inputs and determine neuronal outcomes [108, 144].

Synaptic plasticity refers to synapses' ability to strengthen or weaken over time in response

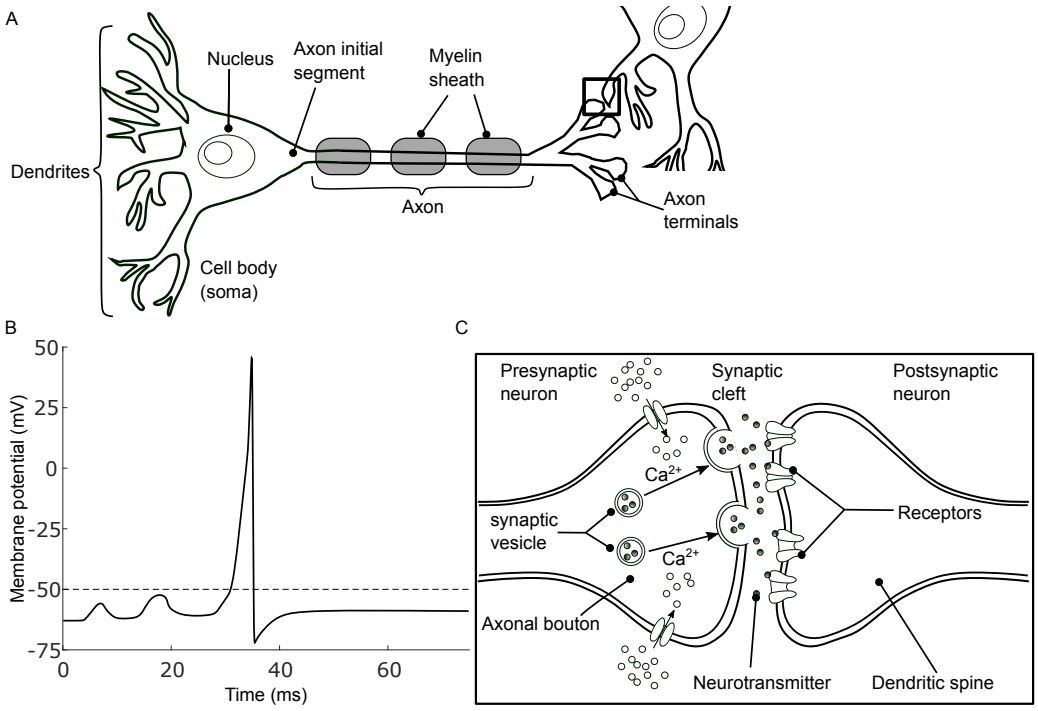

Figure 1.1.: **Structure of a pyramidal neuron and excitability. A)** The neuronal anatomy is designed for efficient and fast signal processing and transmission. The extensive network of dendritic arbors collects synaptic inputs in the form of voltage fluctuations across the cell membrane. When these voltage changes reach the AIS, they can trigger an action potential or spike if the depolarization is above a threshold. This spike then propagates along the axon and reaches the axon terminals, where it activates synapses, facilitating signal transmission to other neurons. These processes collectively form the basis of neural communication and information processing in the nervous system. **B)** Membrane voltage is shown as a function of time. If the depolarization fails to reach the critical threshold needed for opening voltage-gated channels (illustrated by the dashed line), the voltage returns to its resting state without triggering a response, as seen at 10ms and 20ms in the example. However, if the depolarization surpasses this threshold, it initiates a positive feedback loop, resulting in an action potential, as demonstrated at 30ms. This voltage trace is based on simulations using the Hodgkin-Huxley model, which mathematically describes the initiation and propagation of action potentials in neurons. **C)** Detailed structure of a synapse, zoomed in from the highlighted box in panel A. Key features include: *i)* Pre- and postsynaptic neurons in close proximity, *ii)* Synaptic cleft separating the two neurons, *iii)* Neurotransmitter release from the presynaptic neuron due to presynaptic calcium influx, *iv)* Specific receptors on the postsynaptic membrane that neurotransmitters bind to, *v)* Ion channels in the postsynaptic neuron. The image demonstrates how neurotransmitters released into the synaptic cleft bind to receptors on the postsynaptic side, triggering the opening of ion channels. This process results in voltage changes in the postsynaptic compartment, facilitating neural communication. Figures A and C are adapted from templates on `BioRender.com`.

to increases or decreases in their activity. The term "Synaptic plasticity" was first coined in 1894. Later, Donald Hebb postulated that neurons that "fire together, wire together," which indicates that if two neurons consistently fire at the same time, the connection between them is strengthened. This model is referred to as Hebbian learning [77]. In 1973, Terje Lømo and Tim Bliss, in their seminal study, showed that a burst of tetanic (100 Hz) stimulation of the perforant pathway fibers from the entorhinal cortex onto dentate gyrus (DG) led to a significant and long-lasting increase in postsynaptic responses of DG granule cells [13]. They called this phenomenon Long-term potentiation (LTP). The reverse of this process is called Long-term depression (LTD), which weakens synapses. Since the discovery of LTP (and LTD), a key question has remained the focus of researchers that is: what are the molecular processes that enable LTP?

In the section section 1.3, I describe the key mechanisms and experimental methods to study synaptic plasticity mechanisms.

1.3. Molecular players and synaptic plasticity models

Biologically, the adaptability of synaptic connections results from the dynamic of molecular processes occurring in various neuronal compartments. For example, the rapid lateral diffusion of glutamate receptors within the neuronal plasma membrane enables swift adjustments in postsynaptic currents during LTP [29].

Activity-dependent alterations in synaptic protein composition are widely believed to determine the neurobiological mechanisms of learning and memory formation. Fully understanding the molecular dynamics of neurons, including the roles of mRNAs and proteins, would require the development of techniques capable of simultaneously achieving high spatial resolutionto localize and identify every molecule in a neuron preciselyand high temporal resolution to capture the intra- and intermolecular dynamics of these molecules. However, such a comprehensive method does not yet exist. In the meantime, neurobiologists continue to amass a wealth of data using a diverse array of advanced techniques, each offering unique strengths and presenting certain limitations.

For example, *in-situ* hybridization techniques have been instrumental in mapping profiles of mRNA transcripts in neurons [154, 114]. These methods reveal two distinct types of mRNA localization: (1) somatic mRNA, confined to the cytoplasm near the nucleus, and (2) mRNA

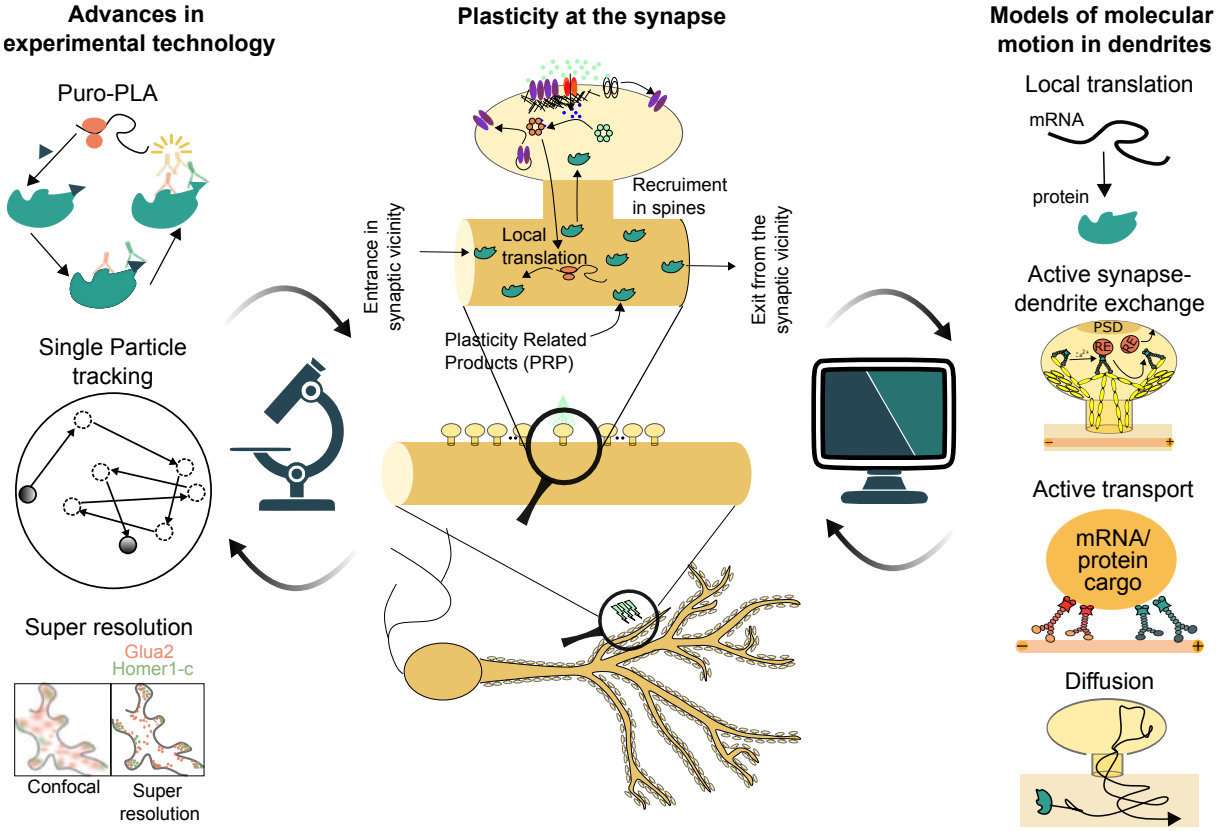

Figure 1.2.: **Linking experimental data and models of protein and mRNA motion in neurons to understand emerging synaptic plasticity** *Left panel:* Examples of modern techniques that enable investigation of dynamics or localization of proteins; *Middle panel:* These techniques allow studying changes in protein density and synaptic plasticity; *Right panel:* Computation models constrained with physiological parameters allow linking molecular motion to protein dynamics and synaptic plasticity. Figure adapted from [177].

distributed in the cytoplasm of both soma and dendrites or axons. While highly informative, *in-situ* hybridization provides a snapshot-like static visualization of mRNA distributions. However, these techniques

Over the past two decades, breakthroughs in single mRNA molecule live-imaging have transformed our understanding of mRNA dynamics [124, 100]. By tracking the motion of individual mRNAs and mRNPs in living neurons, researchers have unraveled new insights into behavior. For instance, the movement of mRNPs in dendrites and axons is primarily driven by active, motor-based transport and follows an aging Levy walk model [152]. These particles exhibit bidirectional, traveling in both anterograde and retrograde directions, and have high mobility. Quantitative analyses suggest that mRNAs are not present in sufficient numbers to populate every synapse individually but are instead local, shared resource [22, 160]. It has been hypothesized that mRNA molecules slow down their motion near active synapses [153], enabling localized translation into proteins precisely where and when they are needed. This targeted mechanism ensures that protein synthesis occurs on demand, supporting synaptic functions. Understanding the dynamics of mRNA trafficking in neurons, including these transport and localization mechanisms, is crucial for advancing our knowledge of how neurons adapt and regulate protein synthesis in response to activity.

Among the most thoroughly studied synaptic proteins are Ca2+ calmodulin-dependent protein kinase II (CaMK2a), Postsynaptic density protein 95 (PSD-95), and AMPAR. CaMK2a is the most abundant synaptic protein, PSD-95 serves as the primary organizer of the Postsynaptic density (PSD), and AMPARs mediate fast excitatory currents. Despite their critical roles at the synapse, interestingly, all three proteins display high mobility in extrasynaptic regions and are only transiently anchored at the synaptic site. However, their dynamics at the synapses differ significantly, as revealed by live-imaging techniques such as Fluorescence recovery after photobleaching (FRAP) and Single Particle Tracking (SPT) Fig. 1.2Left column. For instance, most AMPAR remain within synapses for only seconds to minutes [164], whereas CaMK2a and PSD-95 are more effectively trapped and remain immobilized for tens of minutes [158, 102].

This stochasticity in synaptic protein dynamics highlights the complexity of molecular behavior at synapses and underscores the need to study additional protein species. Characterizing a broader range of synaptic proteins is crucial for uncovering the rules governing synaptic plasticity and neuronal adaptation.

Notably, both the mRNAs encoding for synaptic proteins and synaptic proteins themselves

live for a finite lifetime. Typically, mRNAs live for hours, while proteins can last for days. This rapid turnover is striking, especially considering human memories can last for decades. To explore this dynamic turnover, modern techniques have been developed to track newly synthesized RNA and proteins within cells. Metabolic labeling methods, such as those described by Rabani et al. (2011), Russo et al. (2017), and Akbalik et al. (2017), enable the visualization of newly synthesized RNA molecules. When combined with RNA sequencing techniques like SLAMseq, these methods can track the synthesis and degradation kinetics of nearly all mRNA transcripts [132, 137, 4, 82].

Similarly, several advanced methods now allow the localization and quantification of newly synthesized proteins. One approach involves combining metabolic labeling of proteins with microscopy, often incorporating additional co-detection steps, as seen in Puromycin labeling with Proximity Ligation Assay (Puro-PLA) and Fluorescence non-canonical amino acid tagging (FUNCAT)-Proximation ligation assay (PLA) methods [167]. Another approach involves tagging the endogenous locus of a gene with a fast-folding fluorescent protein, such as superfolder GFP or VENUS, enabling real-time visualization of protein synthesis [45]. These tools facilitate the study of protein expression dynamics at synapses, providing valuable insights into the spatial and temporal regulation of synaptic protein synthesis.

Despite these advancements, imaging techniques typically focus on the distribution and dynamics of only a limited number of molecules at a time. While three decades of research using various imaging approaches have provided critical insights into the behavior of synaptic proteins, only a small fractionjust a few dozenof the 2,700 protein types identified at excitatory pre- and postsynaptic sites have been characterized in detail [43].

To tackle the challenges of current methods, computational models offer a powerful alternative for investigating the complex inter-dependencies of RNA and protein dynamics across spatial and temporal scales. By integrating experimental data and simulating molecular behaviors, these models provide a framework for exploring the complex processes underlying synaptic function and plasticity, advancing our understanding of neuronal systems. In addition, computational models help yield predictions about the speed, spatial distribution, and localization of molecules involved in synaptic plasticity that can be experimentally tested.

In neurons, molecular movements occur through two primary models: (1) Passive diffusion, which involves soluble molecules in the cytoplasm or within organelles membranes, as well as transmembrane and membrane-associated molecules at the cell surface or in organelle mem-

branes, and (2) active transport, where molecules and molecular complexes are transported by binding directly or indirectly to molecular motors, which interact with cytoskeletal networks to drive intracellular movement. Consequently, the spatiotemporal dynamics of proteins and mRNA at synapses are shaped by these trafficking mechanisms, both in the cytoplasm and along the neuron's surface.

Several influential theoretical frameworks have been developed to model molecular dynamics within neurons. These include the tug-of-war model [115], which describes competition among molecular motors; the sushi-belt model [183], which depicts active transport along cytoskeletal tracks; the active synapse-dendrite exchange model [49], which explains the dynamic redistribution of molecules between synapses and dendrites; and the passive diffusion model [19], which captures the random movement of molecules driven by concentration gradients.

Next, I provide an overview of key modeling approaches that describe diffusive and active transport and discuss how these models have deepened our understanding of the role of molecular dynamics in neuronal function.

Diffusion is a prominent mode of molecular motion inside the cytoplasm and along the plasma membrane. Based on experimental observations, several factors determine the rate of diffusion. For instance, protein crowding in neuronal compartments can slow down molecular kinetics [104]. Another factor is the bulkiness of molecular complexes or organelles. Models describing the diffusive movement of mRNAs, mRNPs, and proteins include Brownian motion [18] and anomalous diffusion [152]. One bottleneck revealed by diffusion models is trafficking speed. Modeling studies report that if diffusive movement is considered alone, resources reach the distal dendritic site with long delays, which can alter synaptic outcome [18]. Another problem with pure diffusion is that delivering to spines farther than a few hundred microns is impossible, especially for mRNAs and proteins with shorter half-lives. Interestingly, modeling studies have suggested that intracellular passive diffusion is slower than surface diffusion, further complicating the resource distribution [138]. Facing the delivery delays typical for slow intracellular diffusion, experimental and theoretical studies emphasized the importance of mRNA and protein's active transport along microtubules to ensure fast, long-distance redistribution of resources [18, 183].

To address limitations of only diffusive movement, several computational models considered active microtubule-based molecular transport [84, 115, 183, 11]. Microtubules (MTs) serve as railroads, enabling quick distribution of cargoes containing mRNAs, proteins, and macromolec-

ular complexes across dendrites and axons. Motor proteins serve as intermediaries connecting and moving cargoes on these microtubule tracks [83]. Individual motor proteins can move at fast velocities in a range of 0.2 to 1.5 $\mu m/sec$. However, the motion of a single cargo can typically be described by two phases: fast runs, both anterograde and retrograde, and pauses. The initial hypothesis suggested that these pauses or interruptions resulted from competition at the molecular level between motor proteins traveling in opposite directions. This hypothesis was modeled as the "tug-of-war" between opposing forces, resulting in a much slower net speed ranging from 0.01 to 0.05 $\mu m/sec$ [84]. Müller and colleagues mathematically formulated the tug-of-war mechanism for intracellular motor transport, which proved to be an effective model for studying mRNA and protein cargo motion [115]. However, recent experimental work depicted a more complicated picture of bidirectional intracellular trafficking than initially thought [71].

To capture these additional complex cargo movements in the dendrites, one of the leading hypotheses is that cargo movement is mainly controlled by local demand-driven signaling pathways for cargo in the nearby vicinity [17, 118]. A contemporary model named the "sushi-belt" model [48] was proposed to explain the mRNA motion and its localization to active synaptic sites for local translation. More recently, [183] formalized the sushi-belt model mathematically and showed that this model could capture the complex spatial distribution of protein cargo in the branched dendritic trees. In contracts to diffusion, active transport ensures cargo delivery to distal sites. Interestingly, however, despite using physiological transport and kinetic parameters, the sushi belt model equally results in significant time delays for cargo delivery. Thus, additional mechanisms are needed to ensure the fast delivery of molecules on demand to their target destinations. One of the mechanisms that has been the focus of research for the past three decades is local translation.

Many mRNA have been shown to localize in neurites [22, 171]. It has been hypothesized that those mRNAs serve the demand for synaptic proteins in response to activity [161]. Local protein synthesis could provide protein in suitable time scales matching observed synaptic adaptations. Fonkeu and colleagues recently constructed a computational model to capture diffusive movement and active transport of *Camk2*α mRNA and proteins in dendrites [58]. Their model predicted that local translation bursts can boost CaMKIIα density, which lasts for ≈ 10 hours, and this elevation can span across a distance of 100 microns. Their model also predicted that a similar translation burst in soma has no effect at distal sites because of the restricted diffusive

movement of CaMKIIα protein is [58]. Thus, it is essential for future computational models to include dendritic synthesis of synaptic proteins to predict spatio-temporal scales of synaptic plasticity.

Distributing newly synthesized proteins across the cytoplasm and the plasma membrane to ensure the right copy numbers of synaptic proteins per synapse is a primary focus for computational neuroscience. As I have discussed, long-range cargo transport can be ensured by combining diffusion, active transport, and local protein synthesis. Nonetheless, for transmembrane proteins such as AMPA receptors, local delivery requires an additional step of exocytosis of intracellular vesicles transporting the protein of interest. Reversely, transmembrane proteins are removed/recycled from the plasma membrane via endocytosis. Modulating the exocytosis-to-endocytosis ratio can directly impact the local copy number of transmembrane proteins and, thus, dictates opportunities for local synapses to capture transmembrane proteins. This has been captured by a series of models addressing synaptic trapping of AMPA receptors [49, 159]. Recently, [159] proposed a model to study the bidirectional synaptic plasticity LTP/LTD as a consequence of the relative balance between AMPARs endocytosis and exocytosis. Counterintuitively, the model in [159] predicts that both LTP and LTD increase endocytic flux. In fact, LTP induces a considerably higher endocytic flux than LTD. However, the exocytic flux generated upon LTP induction outweighs the endocytic flux, resulting in an overall synaptic potentiation.

Next, I discuss the role of AMPA receptors in synaptic plasticity and how synaptic activity regulates their accumulation at the synapse.

1.4. Decoding Synaptic plasticity: the role of AMPA Receptors

The majority of LTP observed in the brain results from increased AMPAR density at the post-synaptic membrane or AMPAR single-channel conductance or both [81, 89, 42]. The AMPAR concentration is increased within PSD through a cascade of trafficking and molecular events like diffusion of AMPARs in the extrasynaptic space and exocytosis of AMPAR from the intracellular storage. The direct interaction of GluA1 with scaffold proteins such as 4.1N through the C-terminal domains promotes their activity-driven exocytosis. Several post-translational modi-

fications (PTMs) promote their lateral diffusion, exocytosis, and single-channel conductance. I have summarized the most important PTM in Table 1.1.

Posttranslational modification	Subunit: Residue	Effect	Ref(s)
Palmitoylation	GluA1: C811	limits exocytosis and S818 phosphorylation	[105]
Nitrosylation	GluA1: C875	enhances S831 phosphorylation	[145]
Phosphorylation	GluA1: S845 and S831	enhances interaction with PSD and surface retention, Synergetic enhancement of LTP	[99]
Phosphorylation	GluA1: S818	increases interaction with 4.1N and activity-dependent exocytosis	[105]

Table 1.1.: Impact of Post-translational modifications of AMPAR on their regulation during LTP. For more details, see [42].

Other than the PTM, interaction with auxiliary subunits can also alter the trafficking of AMPAR under basal and activity-dependent. The known AMPARs auxiliary subunit families are Transmembrane AMPA receptor regulatory protein (TARP)s, $\gamma-2$ (stargazin), $\gamma-3, \gamma-4, \gamma-5, \gamma-7$, and $\gamma-8$ [168], the cornichon homologs (CNIH-2/3), GSG1L and CKAMPS (CKAMP44 and CKAMP44-like proteins). These auxiliary subunits can impact the single-channel properties and trafficking [156, 12, 42]. For example, $\gamma-2$ or stargazin interacts with AMPARs and PSD complex proteins including SAP97 and PSD-95, and regulate AMPAR trafficking including their surface diffusion, exocytosis [173], endocytosis [111] and synaptic targeting [27, 94], [12] provides detailed information on auxiliary subunits and their role.

Another factor that can impact AMPAR response to plasticity is the subunit composition of the pore-forming complex. For example, the majority of AMPARs in the adult brain are tetramers of GluA1 and GluA2 subunits [182], and most of the previous studies investigated their regulation in plasticity induction. However, the role of another type of AMPAR, which is permeable to calcium (CP-AMPAR, most likely GluA1 homomers), is controversial. Firstly, at most synapses in glutamatergic neurons, the CP-AMPAR concentrations are very low. However, research has shown that these CP-AMPARs are more abundant in perisynaptic areas. Interestingly, upon the induction of LTP, these receptors can be quickly and temporarily mobilized to the synaptic sites. This rapid recruitment of CP-AMPARs to synapses immediately following LTP induction suggests a dynamic role for these receptors in synaptic plasticity and potentially in the early stages of memory formation [76, 131, 67]. These findings are refuted by another

study [64, 2]. These findings warrant further characterization of the CP-AMPAR role in plasticity induction protocols.

While evidence most clearly elucidated involvement of GLuA1 in LTP, GluA2/GluA3 AMPAR also partake. Most of the work suggests that the GluA2/3 AMPAR are constitutively recruited into synapses and replace the GluA1/A2 AMPAR and possibly GluA1 homomers [148].

Overall, the AMPAR subunit composition, PTMs, and interactions with auxiliary subunits are important for expressing synaptic plasticity and basal activity.

Next, I briefly introduce the different computational models proposed to study AMPAR trafficking under basal and synaptic plasticity.

1.4.1. Models of AMPAR trafficking

Several computational studies have proposed investigating AMPAR dynamics under basal and plasticity conditions by modeling the trafficking processes. In this section, I have described some of the modeling efforts.

Earnshaw and Bressloff a two-compartment model that included the endo-and exocytosis exchange of surface and intracellular AMPARs coupled with the diffusional trapping of surface receptors at the postsynaptic density [50]. Using this minimalistic model, they could replicate many experimental observations at the time, including the effect of blocking endocytosis and exocytosis on synaptic strength, the time course of LTP and LTD expression, and the constitutive exchange of GluA1/2 receptor with GLuA2/3 receptors. However, their model had several limitations, such as the diffusion rate used in their model lay outside observed physiological ranges [50]. In addition, they also did not take the spine and dendritic neck geometry that is known to influence AMPAR trafficking [87, 56]. In a later study, authors modeled individual AMPARs diffusing in and out of PSDs along with their surface diffusion and recycling rates and could reproduce changes in the synaptic AMPA receptor numbers observed experimentally during plasticity [35]. In addition, the authors also showed the contribution of exocytosis and synaptic trapping on AMPAR accumulation at the PSD. However, both models focused on modeling the trafficking within a spine and could not predict the long-range distribution of AMPARs in dendrites and distal spines.

Plasticity induction at a single synapse can also lead to interactions with stimulation synapses and change their synaptic strengths. These changes in unstimulated synapses are termed Het-

erosynaptic plasticity. See [25, 177] for more details on heterosynaptic plasticity. These heterosynaptic changes are attributed to competition in a common pool of dendritic resources. Hence, it is important to model AMPAR dynamics in a multi-spine setting.

In a recent study by Triesch and colleagues, they modeled a small stretch of dendrite with multiple spines on them to study the effect of resource sharing and local competition in plasticity-induced changes at stimulated spine and heterosynaptic changes in unstimulated spines [169]. However, their model also suffered several limitations. For example, their model again doesn't give information about long-range AMPAR distribution, as the size of the local pool can depend on the dendritic location.

None of the previous models have studied the effect of auxiliary subunit interaction with AMPAR. While the previously proposed models have been very useful in studying AMPAR changes during plasticity, they are incomplete in capturing certain aspects of AMAPR trafficking. Hence, a more comprehensive model is required that also includes interaction with auxiliary subunits to understand global and local trafficking of AMPAR under basal and plasticity conditions.

1.5. Research goal

Synaptic plasticity is crucial for higher brain functions such as learning and memory formation. Abnormal synaptic plasticity can lead to neurological disorders such as Parkinson's disease and Alzheimer's. Biologically, synaptic plasticity is realized through intricate dynamics of molecular processes that occur at various spatiotemporal scales. Experimental techniques to investigate these mechanisms allow us to glance at the remarkable complexity of molecular dynamics occurring inside the neuronal dendrites and axons. Nonetheless, we are still far from fully understanding the complete landscape of molecular processes and their specific responses to synaptic signals for two key reasons. First, techniques capable of analyzing thousands of molecules simultaneously, such as omics approaches, are inherently static and offer only a "snapshot" of the neuron's state at a specific moment. Alternatively, most available techniques addressing spatial and temporal dynamics of molecular motion are restricted to only a few molecules at once. In neuronal compartments, such as dendrites, the dynamics of many molecular species are interwoven and unfold across tens to hundreds of microns.

Another significant challenge in experimental neuroscience is untangling the contributions of various mechanisms influencing protein dynamics. While it is possible to study individual processes, such as local protein synthesis, in great detail, isolating and accounting for the effects of other mechanisms-like diffusion, degradation, active transport, and vesicular trafficking processes such as endo- and exocytosis, remains elusive. These overlapping and intertwined processes collectively modulate protein abundance and localization during synaptic plasticity, complicating efforts to assign changes to specific mechanisms.

This is where theoretical frameworks and computational models of mRNA and protein trafficking offer invaluable insights [58, 36, 17]. By leveraging mathematical and physical principles, these models can simulate the motion of individual particles or particle densities, for even thousands of molecular species simultaneously, with the help of experimental data to characterize the kinetics of each process. Simulation of such models enables researchers to predict molecular behavior under various and precise conditions, bridging the gap between large-scale but static datasets and dynamics but sparse experimental observations.

In this work, I aim to provide novel mechanistic insights into synaptic plasticity. For this, I introduce an integrative model of AMPAR and its auxiliary subunit CNIH-2. Using insights drawn from biological data, I describe the basal-level trafficking of two different subtypes of

AMPAR. I aim to predict the response of these two AMPAR subtypes to chemical plasticity induction in my model and validate my model predictions against experimental observations. Even though my findings in this work will be specific to AMPARs, my model can be generalized to study other synaptic proteins that use common trafficking pathways as well. Finally, I also aim to bridge the gap between experimental data and modern data analysis too by developing a novel data analysis pipeline for more comprehensive analysis of fluorescent imaging data.

2. SpyDen: Automating molecular and structural analysis across spines and dendrites

This chapter is adapted from the result section and the supporting information of the article:

Maximilian F. Eggl*, Surbhit Wagle*, Jean P. Filling*, Thomas E. Chater, Yukiko Goda and Tatjana Tchumatchenko. "SpyDen: Automating molecular and structural analysis across spines and dendrites". bioRxiv, (2024): 2024-06: doi: https://doi.org/10.1101/2024.06.07.597872. *: co-first authors

I describe a data analysis pipeline called "SpyDen" in this chapter. I have developed SpyDen in collaboration with fellow lab members Jean Filling and Maximilian Eggl to analyze and extract useful information from the raw data generated by modern fluorescent-based microscopy techniques.

2.1. Introduction

Recent innovations in imaging technology have made it possible to investigate the intricate interactions between synaptic plasticity and neural function, along with the molecular dynamics occurring over time across dendritic trees, axons, and synapses, at scales ranging from micrometers to nanometres [172, 41, 88, 112, 97, 116, 44, 140, 123]. These innovative microscopy techniques enable the quantification of mRNA localization and various protein species along dendritic and axonal trees, as well as within individual synapses, offering unprecedented insights into neuronal synaptic and dendritic dynamics [86, 133, 79].

Traditionally, microscopy images have been annotated manually or semi-manually. This annotation often requires using multiple software tools at different steps of the analysis pipeline to extract meaningful information, such as detecting discrete fluorescent puncta that label mRNAs or newly synthesized proteins and segment and quantify cellular compartments of interest.

Some of the frequently used tools are: java-based *ImageJ/Fiji* [141], python based *NAPARI* [3] or java-based *Neuronstudio* [134].

Meanwhile, modern Artificial Neural Network (ANN)-based automated tools offer significant advantages over traditional methods. For one, they reduce the possibility of annotator biases, and analysis is often reproducible. Another benefit is that large-scale datasets can be analyzed efficiently due to the fully automatic nature of such tools. Some of the frequently used tools include the DeepD3 Framework [57], *SpineS* [7], or the work of [175]. However, they have several limitations. For one, ANN-based techniques work best for images with the exact resolution as images they were trained on, rendering them suboptimal for other resolutions. Secondly, they are not fully open source and open access, which limits their adaptability and customization to diverse experimental needs. Additionally, both tools often address only specific segments of the data analysis pipeline. For a more comprehensive analysis of the structural and molecular composition, one must employ a combination of traditional and ANN-based tools. This mixed approach of switching between tools can become time-intensive and complex as one has to learn different tools.

In Appendix Table A.3, I provide a more exhaustive list of tools and the features they offer. The tools included offer at least some of the capabilities of SpyDen, such as analyzing dendrites, synapses, and mRNA and protein puncta. However, the tool I developed, "SpyDen," integrates these analyses into a single streamlined pipeline, for example, analyzing a dendritic stretch, its synaptic terminals, and the associated protein puncta in a single pipeline. This is a feature that many of the listed tools (in Table A.3) lack, hindering the functionality for comprehensive, all-in-one analysis.

Our pipeline is a structured approach to image analysis that is based upon three principles: *I)* easy to use for multiple types of analyses, *II)* open-source accessibility with data export to a standard and open-format, *III)* ability to customize the annotation generated by the software and generalization across spatial resolution. In addition, our tool is augmented with a Graphical User Interface (GUI) Fig. 2.1 and video tutorials to help new users.

Below, I describe the complete SpyDen pipeline. I also validated SpyDen using expert annotations across numerous use cases to evaluate its power as an integrated platform for molecular image analysis in an efficient and reproducible manner.

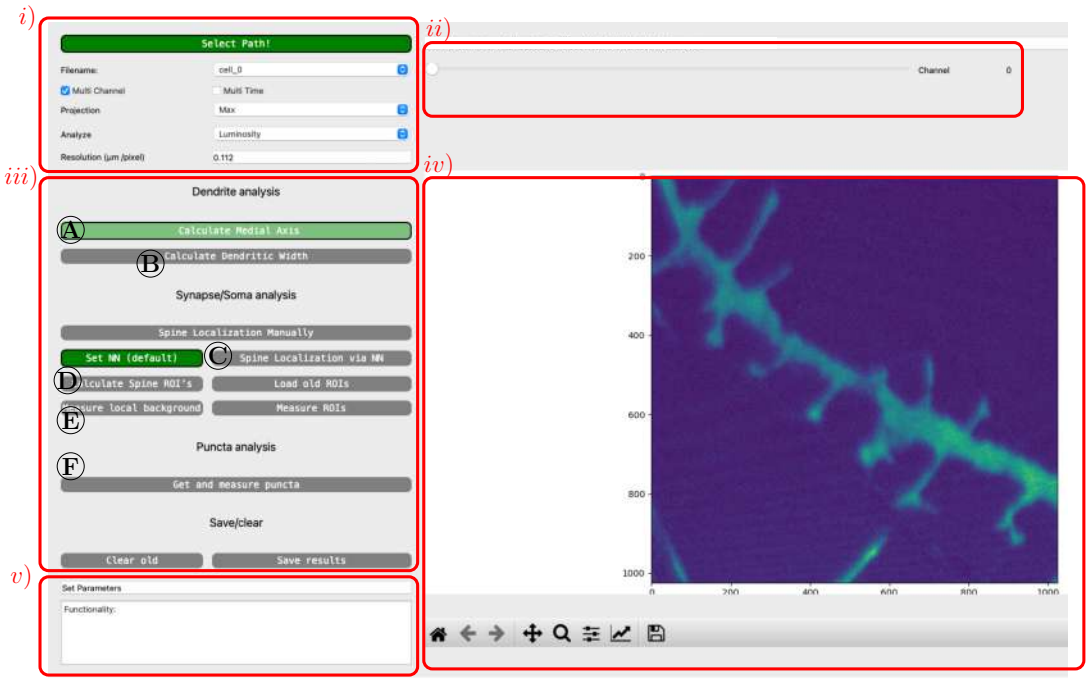

Figure 2.1.: **Graphical User Interface of SpyDen** SpyDen GUI comes with a main window, as shown in the figure. The main window is divided in 5 regions for: **i):** selecting file and metadata, **ii):** optimizing results by adjusting interactive sliders, the number of sliders changes based on the different steps of the analysis pipeline. **iii):** In the letters **A-F**, I highlight the buttons provided for different modes of analyses offered by SpyDen. **iv):** for displaying images and results of the analysis. Finally, **v):** where the user is provided feedback and instruction to use a particular feature. The buttons in red box **iii):** are as follows. **A):** calculate medial axis, **B):** calculate dendritic width, **C):** Spine localization via Neural Network, **D):** Calculating Spine RIOs, **E):** calculating local background intensity, **F):** get and measure puncta. The Figure is adapted from [52].

2.2. SpyDen pipeline

The SpyDen analysis pipeline is built of three primary analyses, namely the dendrite analysis, spine analysis, and puncta analysis Fig. 2.2. In this thesis, I mainly discuss the dendrite and puncta analysis. Please see the original article in [52] for details on Spine analyses.

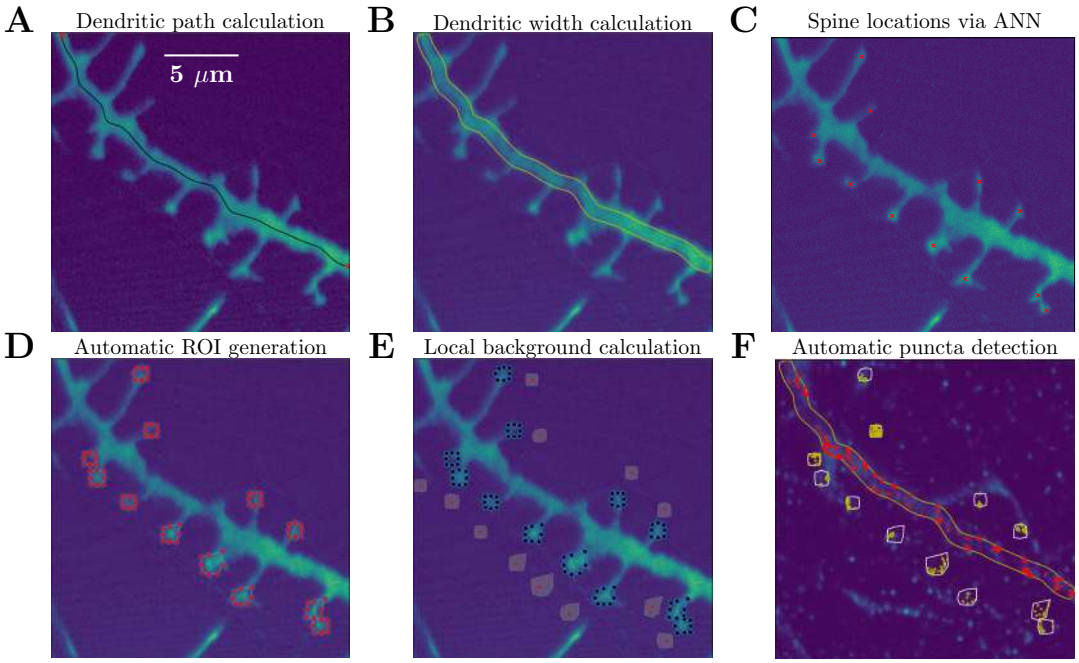

Figure 2.2.: **Analysis pipeline of SpyDen A)** An example image containing a dendritic stretch with spines, optimal medial axis path shown in black **B)** The segmented dendrite (outlined in yellow), after width calculation on the medial axis path **C)** Potential spine heads (red cross) generated using an ANN model. Spyden allows manual editing (adding or deleting) of potential spine heads. **D)** Spyden uses the spine heads as a starting point and calculates the full spine head ROIs. **E)** Spyden also automatically calculates local background intensity from an equal ROI area for each spine. The position of local background ROI can be edited manually. **F)** SpyDen calculates fluorescent puncta in both dendrite and spine ROIS. Image scale bar: 5 μm. Figure is adapted from [52].

Each analysis consists of several interactive objects and requires minimal user input via the GUI. SpyDen allows saving results at the end of each analysis pipeline. To adhere to a structure analysis pipeline, one must go through each analysis sequentially.

2.3. Dendritic analysis

As proteins and mRNAs are localized extensively in the dendrite, systematically segmenting the dendrite is essential to obtain statistics such as mRNA/protein intensity profile along the

dendrite. Spyden's dendritic pipeline inherently obtains this information. The dendritic analysis requires a start and an end node to work. This way, the dendritic distance is known for each point on the path connecting the start and end nodes. To segment the complete dendrite, SpyDen first calculates the optimal route on the medial axis of the dendrite. Then, SpyDen uses this medial axis path to iteratively calculate the dendritic width at each node. Next, I describe the medial path calculation.

► Medial Axis Path finding

For calculating the optimal path, the problem is reduced to the shortest pathfinding task in a maze. The algorithm traces the best route through the dendrite using the user-defined start and end points. This process begins by transforming the experimental image into a binary matrix, where pixels with luminosity above a defined threshold represent navigable paths. In contrast, all other pixels are treated as obstacles Fig. A.1.B. The shortest path through this binary matrix is computed using the Dijkstra algorithm from the NetworkX library [70]. I employed downsampling for larger images (bigger than 512x512 pixels) to speed up the computation.

However, this approach alone often places the calculated path along the dendrite's edges, especially for curved or bent dendrites. For this, the SpyDen algorithm augments the binary matrix with an additional factor representing the distance of each pixel from the nearest boundary (pixels below the luminosity threshold). This extra factor prioritizes pixels closer to the dendrites center by assigning higher weights to those further from the edges. The result is a medial axis path that accurately follows the dendrites central trajectory. To visualize this adjustment, see Fig. A.1.C, where peaks indicate pixels furthest from the dendritic boundary.

The resulting path consists of all pixels between the dendritic endpoints. The full pixel-resolution path then undergoes several reduction steps to get a compressed representation of key control points. These control points are easy to store, provide editability of the path, and improve computational efficiency. These control points are selected through curvature-based sampling and are the editable nodes shown in Fig. 2.3. Linear interpolation between the control points can regenerate the full path as needed. I have provided the complete algorithmic implementation of the reduction process in the Appendix as 1.

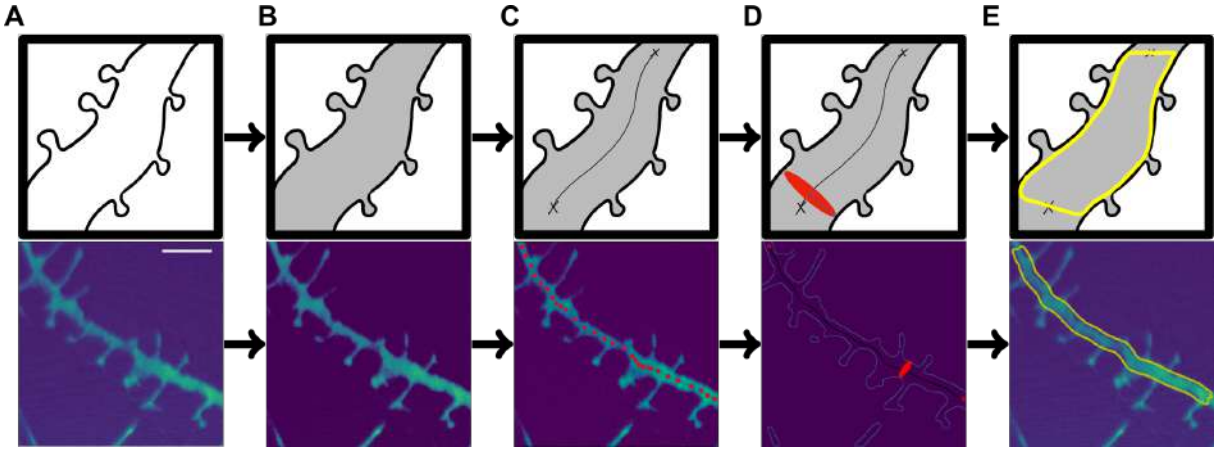

Figure 2.3.: **Various steps of dendritic segmentation. A)** An example image with a dendritic branch and spines, scale bar: 5μm. **B)** After applying a median filter to reduce the salt and pepper noise followed by a user-defined threshold (default is the mean) for a rudimentary segmentation of the fore- and background. This threshold defines the maze for the algorithm to calculate the medial axis path on **C)** A medial axis path is calculated as the weighted shortest path between user-defined endpoints. **D)** For each point on the medial axis path, an ellipse is fitted that covers the dendritic width. **E)** The width calculated at each point is further processed to avoid abrupt changes due to various factors, such as the presence of the spine and the gap in the edges. This processing results in a smooth dendritic segment. Figure is adapted from [52].

► Dendritic Width Calculation

After calculating the medial axis path, the entire selected dendritic stretch is segmented. This requires a precise calculation of width at each point. To achieve this, my algorithm defines an ellipse at each point along the medial axis. The semi-major axis is kept perpendicular to the medial axis and iteratively expanded until it intersects with the dendritic boundary detected. The dendritic boundaries are detected using the Canny edge detection algorithm [23]. Meanwhile, the semi-minor axis of the ellipse is set to a small fixed value and aligned with the direction of the medial axis. The Canny edge detection is applied to the median-filtered and thresholded image. I have illustrated this ellipse-based approach in the top panel of Fig. 2.3.D.

The ellipse-based method offers two advantages. It avoids ambiguities in edge detection by differentiating between synaptic and dendritic edges, often indistinguishable from direct Canny detection. Second, unlike ray-based approaches, the expanding ellipse method ensures that it eventually intersects an edge and mitigates gaps in the dendritic boundary caused by variations in luminosity, as a single ray might escape through gaps and fail to detect an edge. I showed an example of the ellipse-based for better visualization in Fig. 2.4.

The algorithm excludes non-dendritic structures such as spines and filopodia by applying

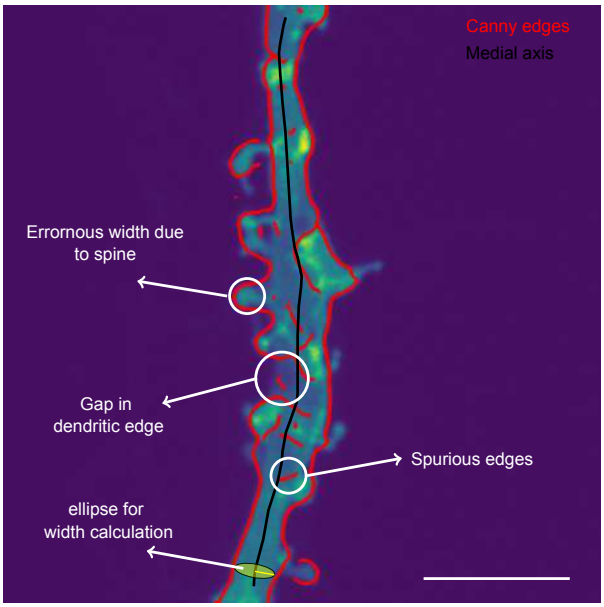

Figure 2.4.: **Example of dendritic width calculation** A canny-edge detection algorithm on an example image's filtered and thresholded version provides an acceptable set of edges. However, several problems preclude using the edges directly (as illustrated by the white circles). Instead, I decided to apply the ellipse-based approach seen in Fig. 2.3.A-E to encounter these problems and generate a smooth dendritic segmentation. Scale bar: 5μm. Figure is adapted from [52]

.

smoothing conditions to prevent abrupt width changes. SpyDen further incorporates user-interactive sliders to modify (i) the width-multiplication factor and (ii) the smoothing intensity, allowing users to refine segmentation results and optimize dendritic width calculation. The complete algorithm for dendritic width calculation, including smoothing and user-adjustable parameters, is detailed in Algorithm 2 in the Appendix. This robust method ensures precise segmentation and width determination, facilitating accurate dendritic analysis in diverse experimental conditions.

► Validation

I validated the dendritic segmentation across three distinct datasets to validate SpyDen's performance and demonstrate its robustness under varying experimental paradigms. These datasets Chater [26], Helm [79], and Cultured are publicly available and published, except for the Cultured dataset, which is newly introduced in this work. This Cultured dataset was acquired by my collaborators, Dr. Thomas Chater and Prof. Yukiko Goda. The Chater dataset comprises neurons from organotypic slice cultures Fig. 2.5.A while the Helm Fig. 2.5.B and Cultured datasets Fig. 2.5.C feature images of dissociated neuronal cultures. This combination offers a diverse

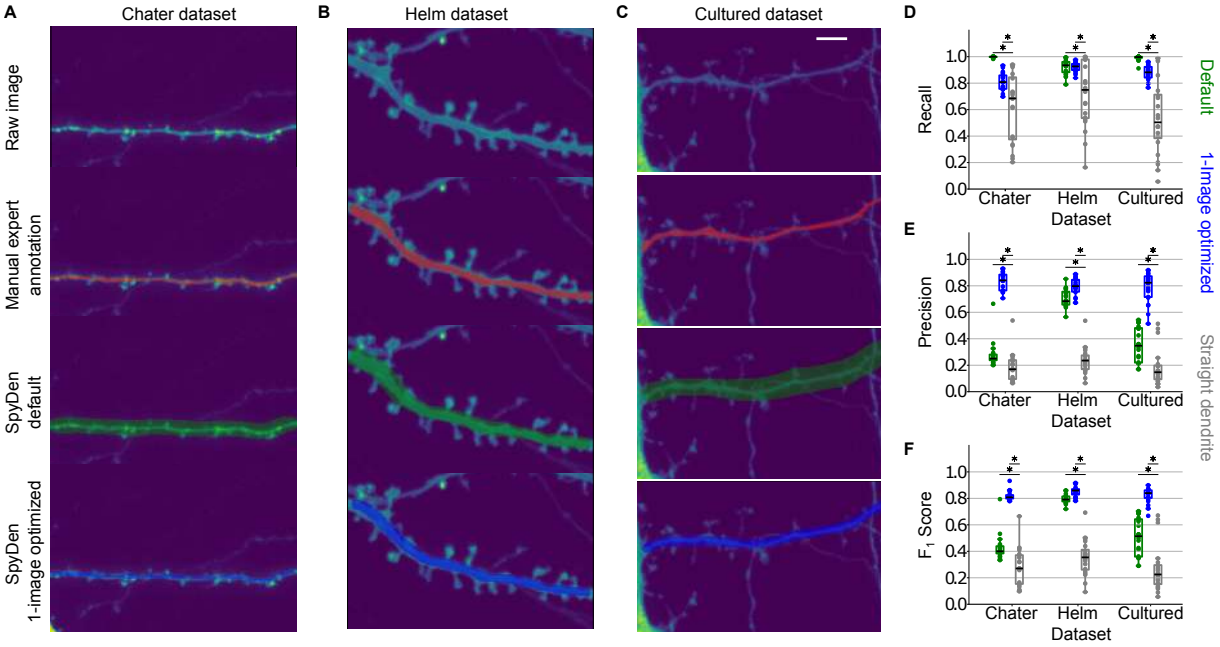

Figure 2.5.: **SpyDen dendritic segmentation performance is comparable to manual segmentation A-C)** Example dendrite from the Chater data (in A) [26]), Helm dataset (in B) [79], and unpublished Cultured data (in C);*Top row:*: Raw image; *second row:*: same image with manual annotations shown in red; *third row:* SpyDen segmentation with default parameter set; *last row:* SpyDen segmentation with augmented parameters optimized for one image in blue. **D) -F)** Recall (*D*), Precision (*E*) and F_1-score (*F*) as performance measure of dendritic segmentation. Performance of the SpyDen segmentation with default (in green) and 1-image optimized parameters (blue), respectively. Additionally, I calculated a baseline (called the *straight dendrite*), where a diagonal chord ($2\mu m$ width) is drawn between the dendritic start and endpoints and designated as the dendrite (in grey). For all images: scale bar: 5 μm and * refers to $p < 0.05$. Figure adapted from [52]

and compelling data set for evaluating SpyDen's capabilities.

A notable distinction among these datasets lies in their experimental resolutions, a factor critical for the performance of many neural network algorithms. Additionally, the datasets have varying signal-to-noise ratios in Fig. 2.5.A-C.

The evaluation begins with assessing the dendritic segmentation algorithm's performance compared to manual expert evaluations. Each dataset contains 20 dendrites. Typical usage of SpyDen involves applying the automatic algorithm's results as-is, adjusting the medial axis path of the dendrite, or fine-tuning algorithm parameters using slider adjustments. To replicate this usage, two segmentation scenarios were analyzed:

- **Default**: Results from the automatic algorithm with default SpyDen parameters.
- **1-Image Optimized**: Results after fine-tuning the algorithm parameters on a single image

from the dataset, then applying these settings across the remaining images.

In Fig. 2.5.A-C, I show an example dendrite from the three datasets along with the segmentations, with SpyDen-generated segmentations in green and blue. I utilized several metrics to quantify SpyDens performance compared to expert annotations (ground truth, in red). I treated the segmentation task as a classification problem, where each pixel is categorized as either in or out of the dendrite. This task is inherently imbalanced, with many more non-dendritic pixels than dendritic ones. To evaluate performance, I employed recall, precision, and the F_1 score, standard metrics for imbalanced datasets. Recall assesses the proportion of true positives correctly identified, precision evaluates the model's ability to minimize false positives, and the F_1 score combines both recall and precision for a balanced evaluation as:

$$\begin{aligned} \text{recall} &= \frac{t_p}{t_p + f_n} \\ \text{precision} &= \frac{t_p}{t_p + f_p} \\ F_1 &= \frac{2 \times \text{recall} \times \text{precision}}{\text{recall} + \text{precision}} \end{aligned}$$

Performance metrics for SpyDen across the Helm, Chater, and Cultured datasets are shown in Fig. 2.5.D&F. For the Helm dataset [79], I achieved a high recall ($\sim$ 0.9) and precision ($\sim$ 0.8) for both default and 1-image optimized segmentation, resulting in an average F1 score of 0.85. This consistency reflects SpyDen's design and optimization for Helm-like experimental conditions, where parameter adjustments provided minimal improvement.

To further explore SpyDens performance, a naive segmentation strategy ("straight dendrite") was tested. This naive segmentation achieved an F_1 score of $\sim$0.4 and $\sim$0.3 for the Helm [79] dataset and Chater [26] dataset, respectively. This naive strategy struggled with curved dendrites, resulting in low precision value and variable recall value. SpyDen with default parameters yielded lower precision and F_1 score on the Chater dataset [26]; however, the recall value was high. This was due to a lower contrast between the actual dendrite and background fluorescent, leading to over-segmentation and adjusting the Gaussian filter variance improved performance, achieving an F_1 score of $\sim$0.82. Similarly, the Cultured dataset displayed over-segmentation under default settings but achieved 0.85 F_1 scores with parameter optimization.

Significantly, in my analysis, I adjusted the parameters for a single image per dataset and

applied them to others, demonstrating SpyDens adaptability. Despite focusing on transferable parameters without editing dendritic paths, SpyDen consistently outmatched the baseline and delivered robust results across several datasets.

2.4. Puncta analysis

One of the most commonly investigated biological samples is the fluorescent labeling of mRNAs and newly synthesized proteins. Traditionally, the techniques used to label mRNA such as Fluorescence *in situ* hybridization (FISH) [171, 58] and Small Molecule Fluorescence *in situ* hybridization (smFISH) [30] and newly-synthesized protein such as FUNCAT-PLA[167], Puro-PLA[167] result in images with fluorescent bright puncta against a dark background (see Fig. 2.2.F). Hence, detecting and quantifying fluorescent bright puncta is critical in analyzing biological images. SpyDen provides a robust pipeline for identifying puncta for multi-channel or multi-time image datasets.

► **Fluorescence puncta detection**

SpyDen uses the **Laplacian of Gaussian (LoG)** technique, implemented via the python library *skimage*, to detect fluorescent spots in experimental images automatically. This method requires a threshold value to define the absolute lower bound for scale-space maxima. However, the optimal threshold varies depending on the type of biological structure being analyzed.

SpyDen accommodates puncta detection in multiple neuronal structures (e.g., spines, dendrites, somata) by providing two adjustable sliders:

- Threshold Dendrite
- Threshold Synapse/Soma

These sliders allow users to independently set threshold values for different types of ROIs. The puncta detection works as follows: for an image $I(t, c, x, y)$ and an ROI $R(t, c, x, y)$ within I, the threshold value $t_R(t, c)$ is calculated as:

$$t_R(t, c) = \max(R(t, c, j, k)) \times \frac{\gamma}{100}$$

Here: - $R(t, c, j, k)$ represents the array of fluorescence intensity values for all $j, k \in ROI$ in channel c at time t. and γ corresponds to the slider values.

SpyDen also allows users to detect puncta of varying sizes by adjusting the minimum and maximum standard deviations of the Gaussian kernel via the **Puncta Size** slider.

Additionally, SpyDen omits puncta detection in ROIs with intensities below the background noise level to enhance efficiency and reduce false-positive detections. This ensures reliable and accurate identification of fluorescent puncta in diverse experimental datasets.

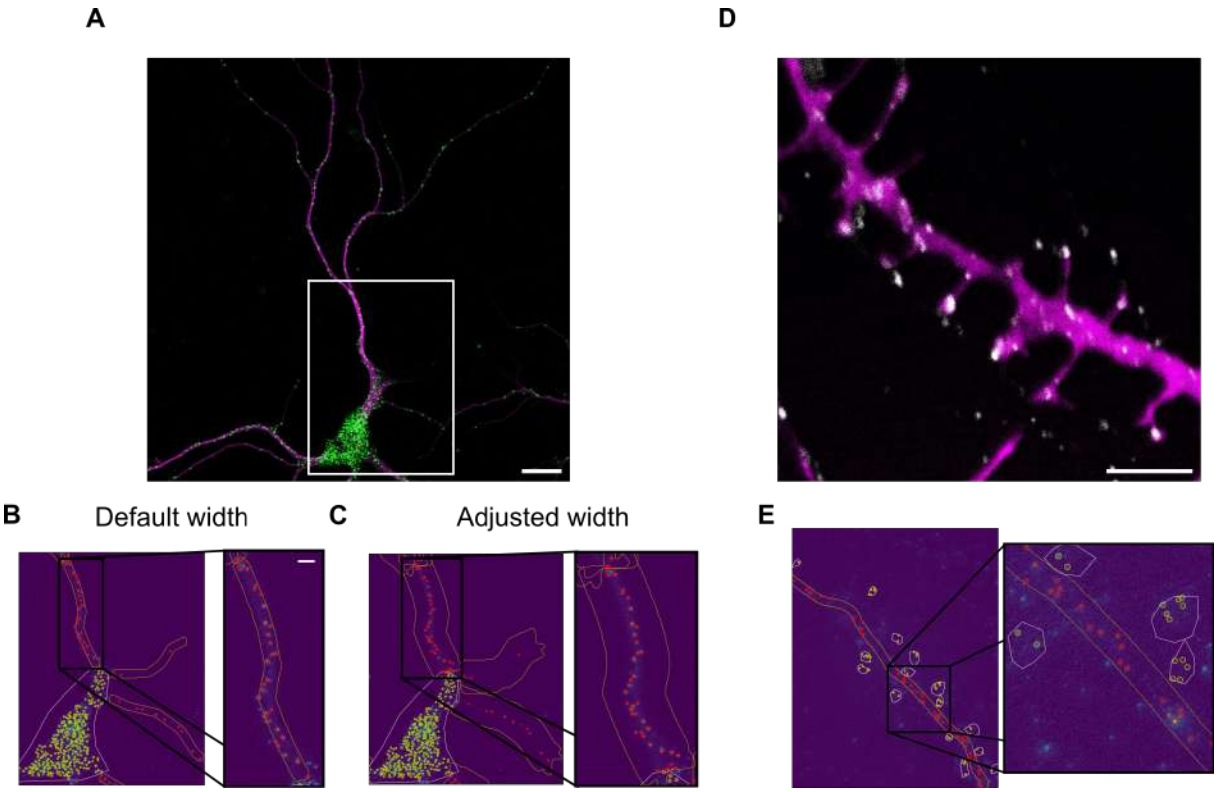

Figure 2.6.: **Puncta detection and analysis using SpyDen A)** An example image of cultured pyramidal neuron from with processed for FISH against *Camk2a* mRNA (in green) and fluorescently immunolabeled MAP2 (in magenta); scale bar: $20\mu m$. **B)** Puncta detected in the soma (shown in yellow) and in dendrite segmented with default parameters (shown in red); Scale bar $10\mu m$. **C)** Same as **B)** but for adjusted width calculation parameter. **D)** I show an example dendritic stretch from a cultured neuron processed for antibody labeling against Homer1; the dendritic boundary was visualized using Dio dye. **E)** Homer1 fluorescent puncta detected by SpyDen in dendritic stretch (in red) and in spine heads (in yellow). In **D, C, E**, I show the spine and soma segmented using SpyDen (outlined in white) and the dendrite, also segmented by SpyDen (outlined in yellow). The figure is modified from [52].

As an example, I show the puncta detected in different datasets that involved imaging mRNA and protein localization in In Fig. 2.6,

First, *CamK2a* mRNA, encoding for the CaMK2α protein, is known to be localized in the cell

somata and neurites (as can be seen in In Fig. 2.6.A). SpyDen efficiently detected the somatic and dendritic mRNA puncta as shown in Fig. 2.6.B&.C.

Second, Homer1 is a crucial synaptic protein that mainly localizes in the spine head [79] and, hence, is often used as a marker for spines (shown in Fig. 2.6.D). SpyDen detected homer1 puncta mainly in the spine head and fewer puncta in dendrite that could belong to the stubby spines (see Fig. 2.6.E).

▶ Validation

Next, I assessed the accuracy of SpyDen's puncta analysis. I analyzed the dataset from two recently published datasets [58, 11] and compared the results against the computational tool used in respective studies.

- **Dataset 1:** Confocal microscopy images of mouse primary cortical neurons with two Cdc42 isoforms labeled using single-molecule mRNA FISH Fig. 2.7.A&B.

- **Dataset 2:** Confocal microscopy images of rat dissociated hippocampal cultured neurons, where mRNA FISH was performed for *Camk2a* (Fig. 2.7.C, left).

In the original studies, **StarSearch (RajLab)** was used to quantify smFISH puncta for the Cdc42 isoforms (E6 and E7) in Dataset 1 [11]. SpyDens analysis produced comparable results, accurately reflecting the percentage localization of the two isoforms between soma and neurites (Fig. 2.7.D&E).

For Dataset 2 [58], **Neurobits** [171] was used to analyze *Camk2a* mRNA. Similarly, SpyDens results closely matched Neurobits' findings in terms of quantifying *Camk2a* mRNA in somatic and dendritic compartments (Fig. 2.7.F). SpyDen also produced comparable puncta counts for soma and neurites across both datasets (Fig. 2.7.G-I), making it a robust puncta detection tool for several types of ROIs. SpyDen can also be used to detect fluorescent puncta in smaller ROIs such as spines; for a full description, please refer to [52].

SpyDen, along with matching the performance of established tools like StarSearch and Neurobits, also provides additional flexibility, efficiency, and user-friendly features, making it a powerful tool for puncta analysis in diverse experimental contexts.

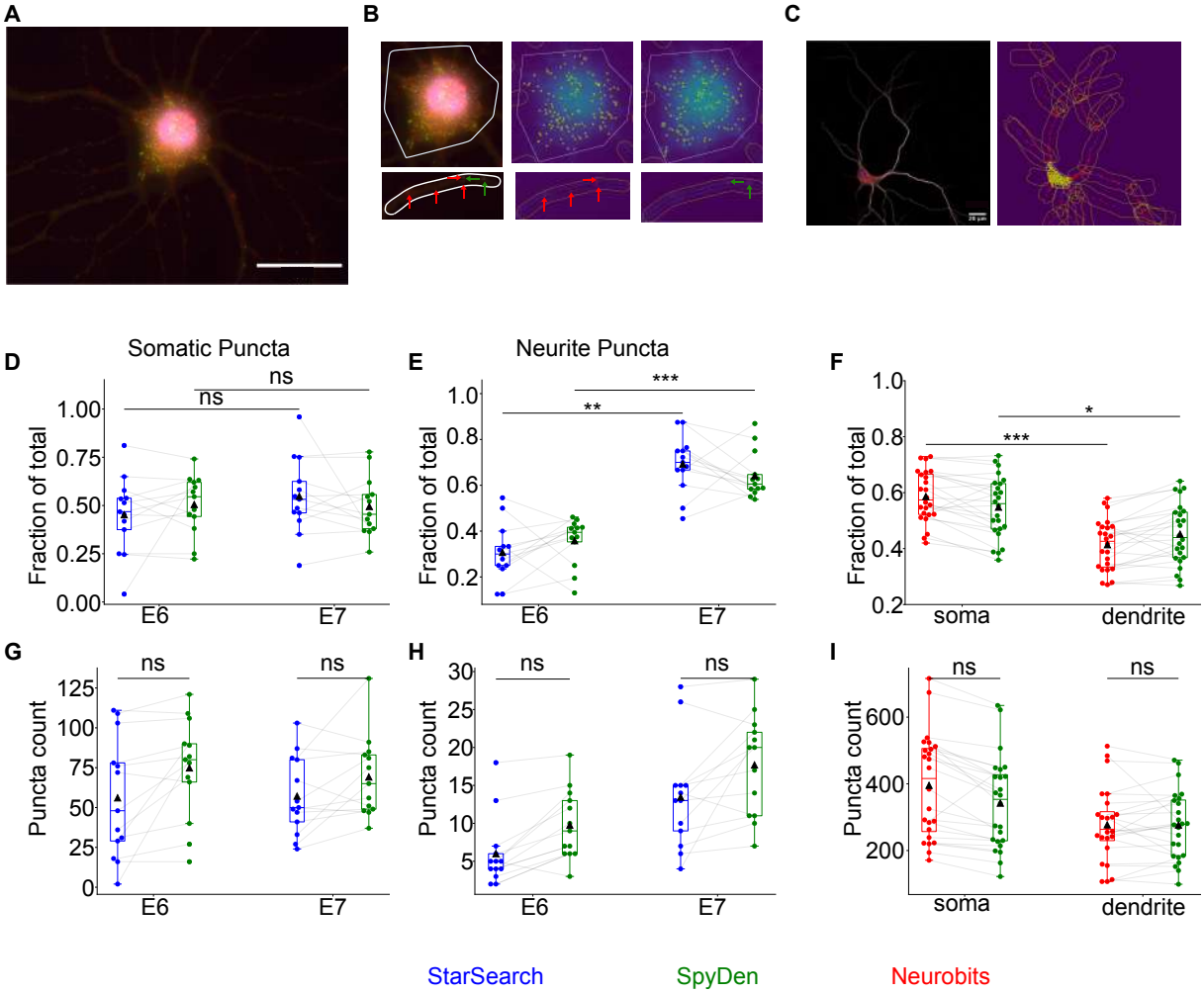

Figure 2.7.: **SpyDen's puncta detection was validated against published datasets. A)** An example neuron processed for smFISH against Cddc42 isoforms E6 (green channel) and E7 isoforms (red channel), the cell body is labeled with DAPI (blue channel); Scale bar: 5 μm. **B)** Zoomed-in image of the segmented soma and an example dendrite. *top row:* smFISH image of soma and puncta detected by SpyDen for E6 and E7. *bottom row:* smFISH in the image and the same puncta detected by SpyDen (red: E7 and green: E6). **C)** *Left image:* An example neuron processed for FISH against *Camk2a* mRNA (in red) with fluorescent immunolabeling of MAP2 for neurites (gray), scale bar: 20 μm. *Right* SpyDen outputted somatic mRNA puncta and dendritic mRNA puncta. **D)** Somatic puncta detection from SpyDen and StarSearch obtained comparable fractions. **E)** Same as D for neurites. Isoform E7 is preferentially localized in the neurites as opposed to isoform E6 [11]. SpyDen analysis generated same results (*: p-value < 0.05,**: p-value < 0.01, ***: p-value < 0.001). **F)** Soma vs neurites fraction of total *Camk2a* mRNA with higher localization in soma. SpyDen analysis can replicate the results obtained using Neurobits. **G-I)** No significant difference in the number of puncta detected by StarSearch vs. SpyDen in the soma (*G*), in neurites (*H*), and FISH puncta count by Neurobits vs. SpyDen (*I*). The figure is adapted from [52].

► **Key Advantages of SpyDen's Puncta Detection**

- ROI-specific detection: Established tools such as Neurobits process the entire image and assign each identified puncta to an ROI. However, this approach is inefficient as the complete image is processed. SpyDen, on the other hand, focuses on puncta detection within predefined ROIs. SpyDen's targeted approach significantly reduces analysis time per image.
- Parameter adjustment: SpyDen allows users to inspect and optimize algorithm parameters, such as puncta size and intensity threshold, providing flexibility to fine-tune results.
- Automatic Statistics Output: SpyDen generates detailed statistics for each detected punctum, including location, radius, intensity range (minimum and maximum), etc. These outputs are readily accessible and reduce post-analysis processing. I have listed the output statistics generated by SpyDen in Table A.2.
- Easy to Use with video tutorials: SpyDen comes with extensive video tutorials, simplifying the learning process compared to tools like StarSearch and Neurobits, which provide text-based documentation.

2.5. Brief Summary

This chapter describes a Python-based tool I developed to perform several fluorescent-based neuronal imaging data analyses. The tool offers several analyses, including 1. Dendritic segmentation and analysis, 2. Spine segmentation and analysis, and 3. Puncta detection and analysis. Existing tools provide one or more of these features, but not all. Hence, I developed SpyDen. The first step in the analysis is to segment the dendrite for which I calculate the medial axis path and then calculate the width at each point on this path using an ellipse-based approach. Next, I used the segmented dendrites to identify fluorescent puncta and calculate their statistic. Next, I introduce how the biological information extracted from such microscopy data set helped me develop mathematical models of AMPAR trafficking under basal conditions. I also used my model to study AMPAR copy-number change upon LTP induction.

3. Model of AMPA Receptor Trafficking Under Baseline Condition

This chapter is adapted from the results section and the supporting information of the article:
Surbhit Wagle, Maximilian K. Kracht, Anne Bührke, Amparo Acker-Plamer, Nataliya Kraynyukova, Anne-Sophie Hafner, Erin M. Schuman and Tatjana Tchumatchenko. "An integrative model of AMPA receptor trafficking reveals the central contribution of local translation in subtype-specific kinetics". bioRxiv, (2025): doi: https://doi.org/10.1101/2025.02.08.637220.

In this chapter, I discuss the different trafficking mechanisms that are known to orchestrate the movement of AMPAR and their distribution along the dendritic tree. I also present the simulations of the trafficking mechanism under baseline conditions using a computational model.

3.1. Modes of AMPA receptor trafficking

AMPARs are crucial to excitatory synaptic communication in the brain, mediating the fast depolarizing synaptic current. They play an integral role in the mechanisms underlying synaptic plasticity, particularly in the expression of long-term potentiation (LTP), a process essential for learning and memory. The strength of excitatory synaptic transmission is largely determined by the number and composition of synaptic AMPARs within the PSD. Therefore, regulating AMPAR availability and functionality at synapses is a key mechanism for controlling synaptic efficacy and neuronal communication [42, 29].

Neurons, such as the pyramidal neurons in the hippocampus and cortex, have long dendritic arbors that can extend several hundreds of micrometers. This vast network of dendritic processes enables them to integrate inputs from thousands of other neurons. These dendrites are densely populated with dendritic spines, small protrusions that serve as the primary sites for excitatory synaptic input. Typically, dendritic spines are distributed at a density of approximately 12 spines per micrometer along the dendrite [119].

For effective detection of excitatory inputs (i.e. detecting the release of glutamate from the axons of presynaptic neurons), postsynaptic neurons must make sure that their dendritic spines are appropriately populated with sufficient AMPARs. The presence of AMPARs at these spines is critical for translating synaptic signals into postsynaptic responses, thereby enabling the functional connectivity necessary for neural circuit activity and plasticity. There are several mechanisms that neurons employ to overcome the challenges of their structural complexity and ensure the distribution of AMPARs. These trafficking mechanisms can be divided into roughly two modes based on their spatial extent. First is the global trafficking mode, which can again be divided into two subsets *i)* passive, Brownian motion-like diffusion, and *ii)* active, motor protein-based transport Fig. 3.1.B. These two mechanisms can shape the dendrite-wide landscape of AMPAR distributions. The second mode is the local trafficking mode. As AMPAR is a trans-membrane protein, it has a population that is bound to the plasma membrane and another population that is intracellular. The exchange between these two populations occurs mostly through local trafficking mechanisms, namely, *i)* endocytosis that causes internalization of the surface receptors and *ii)* exocytosis that causes surface insertion of cytoplasmic receptors Fig. 3.1.C.

Here, I describe the molecular processes that are known to traffic the AMPARs along the dendrite of neuron, thus shaping their spatial distribution in the neuron.

3.1.1. Surface movements

The plasma membrane of cells is a dynamic and compartmentalized medium, characterized by its viscous nature. Within this structure, neurotransmitter receptors including AMPARs can undergo Brownian diffusion when not stabilized by interactions with cytoskeletal or scaffold proteins which are relatively fixed on in the plasma membrane. Several studies tracking the movements of individual endogenous AMPARs on neuronal surfaces have confirmed these predicted behaviors [14, 9, 78], while also revealing some unexpected features. This is especially evident in the extrasynaptic compartment. Receptors in the extrasynaptic neuronal membrane can typically diffuse freely at rates of up to 1 $\mu m^2/s$ [9, 121, 90]. Similarly, high mobility is observed in intracellular membranes, such as the endoplasmic reticulum (ER).

Brownian diffusion is an energetically neutral process for the cell, entirely driven by thermal agitation and molecular collision. The mean squared displacement, MSD, achieved through

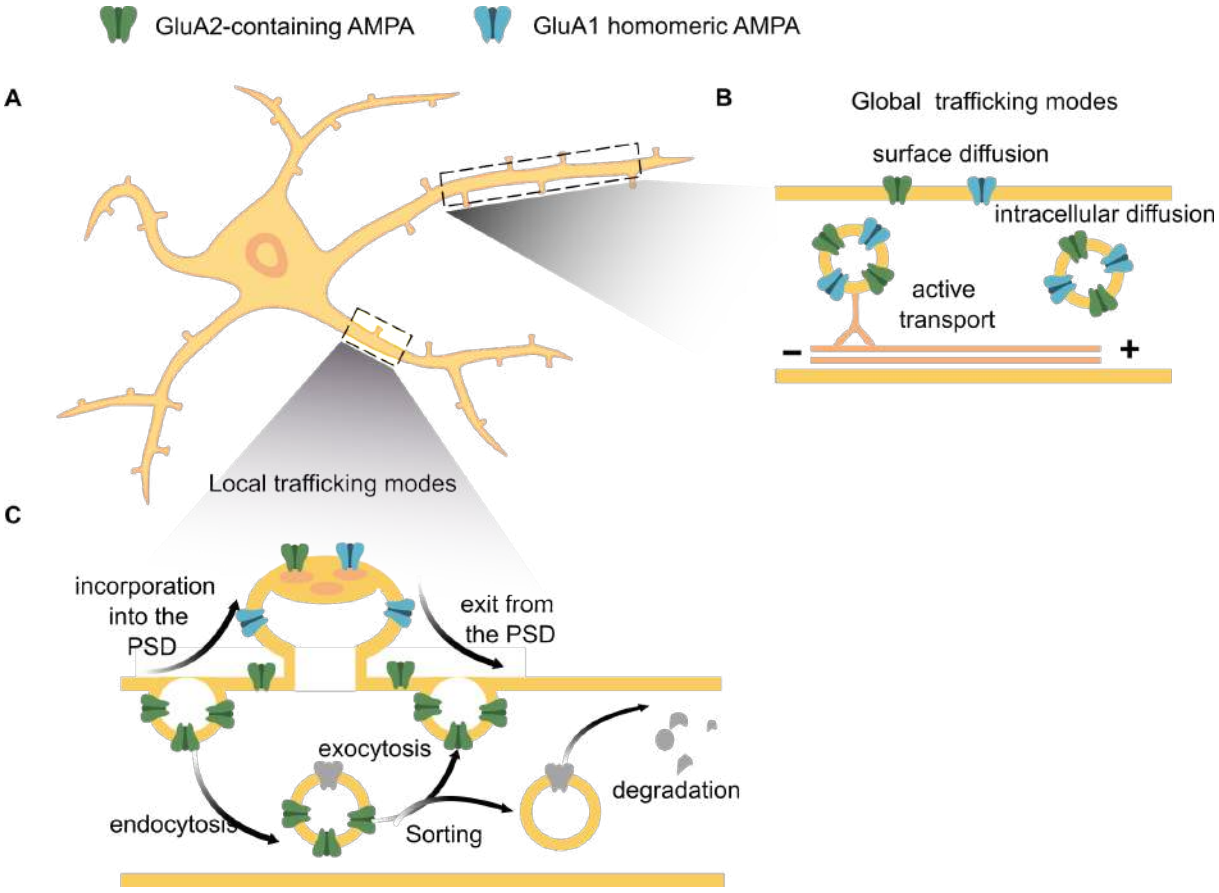

Figure 3.1.: **Various trafficking processes of AMPARs. A)** Synapses distributed along the dendritic arbors require GluA1- and GluA2-containing AMPARs for LTP. Various processes impact AMPAR availability, and their time scales range from seconds to hours. **B)** The global landscape of AMPARs in a neuron is shaped by fast bidirectional active transport and slow passive diffusion on the cell surface or inside the cytoplasm. **C)** The local trafficking modes, including slow endocytosis and exocytosis of AMPARs, help to maintain a sufficient pool of extrasynaptic receptors. Upon endocytosis, AMPARs are sorted into recycling and early endosomes that are reinserted. AMPARs in the late endosome are degraded. Following surface insertion, AMPARs reach PSD by their diffusion towards the synapse and binding to PDZ domain scaffold proteins at the PSD. See text for full description. The figure is adapted from [178].

diffusion is proportional to the time:

$$MSD(t) \propto t^{\alpha} \tag{3.1}$$

t represents the time since the start of the observation, and $\alpha = 1$ for diffusive movement, $\alpha < 1$ for subdiffusive movement, and $\alpha > 1$ for superdiffusive movement. As the displacement depends on the square root of time for a diffusive movement, purely diffusive movement is efficient on short time scales but not on long time scales. For instance, a receptor diffusing at an average rate of 1 $\mu m^2/s$ can move roughly a micrometer in 1 second but travel only about 15 micrometers in 100 seconds. In contrast, intracellular motor-driven transport, which relies on ATP for energy, enables receptors to traverse approximately 200 micrometers in the same amount of time, making it far more effective for longer distances.

Interestingly, while directed receptor movement on intracellular tracks is well-documented, reports of directed movement on the neuronal surface are rare, with only a few exceptions noted in the literature (see [166]). These findings highlight the reliance on diffusion for localized receptor dynamics and the necessity of motor-driven mechanisms for more extensive intracellular transport.

Measuring receptor movement is best in live cells for obvious reasons. In live neurons, one of the most common and oldest methods is FRAP. In this method, fluorescently tagged receptors are photobleached in a small ROI using a focused laser beam, and the subsequent recovery of fluorescence in this ROI is recorded to access the rate of receptor mobility in the surrounding membrane environment Fig. 3.2.A. However, it has several shortcomings, such as a lack of spatial resolution due to diffraction limit, and cannot be used for subsynaptic information on receptor movement. Also, it is not suited for studying endogenous receptor movement as it often requires overexpression that strongly biases receptor composition. Additionally, it also biases measurements of mobility as overexpression can saturate the limited number of trapping sites.

Another commonly used technique is single-particle or single-molecule tracking Fig. 3.2.B. This method has advanced from earlier techniques that used receptor-bound nanogold or latex particle tracking to a highly refined approach capable of tracking single fluorophores attached to receptors with remarkable speed (up to kilohertz) and resolution (in the 10-nm range) [106, 32]. Thanks to their inherent single-molecule sensitivity, these techniques are particularly well-

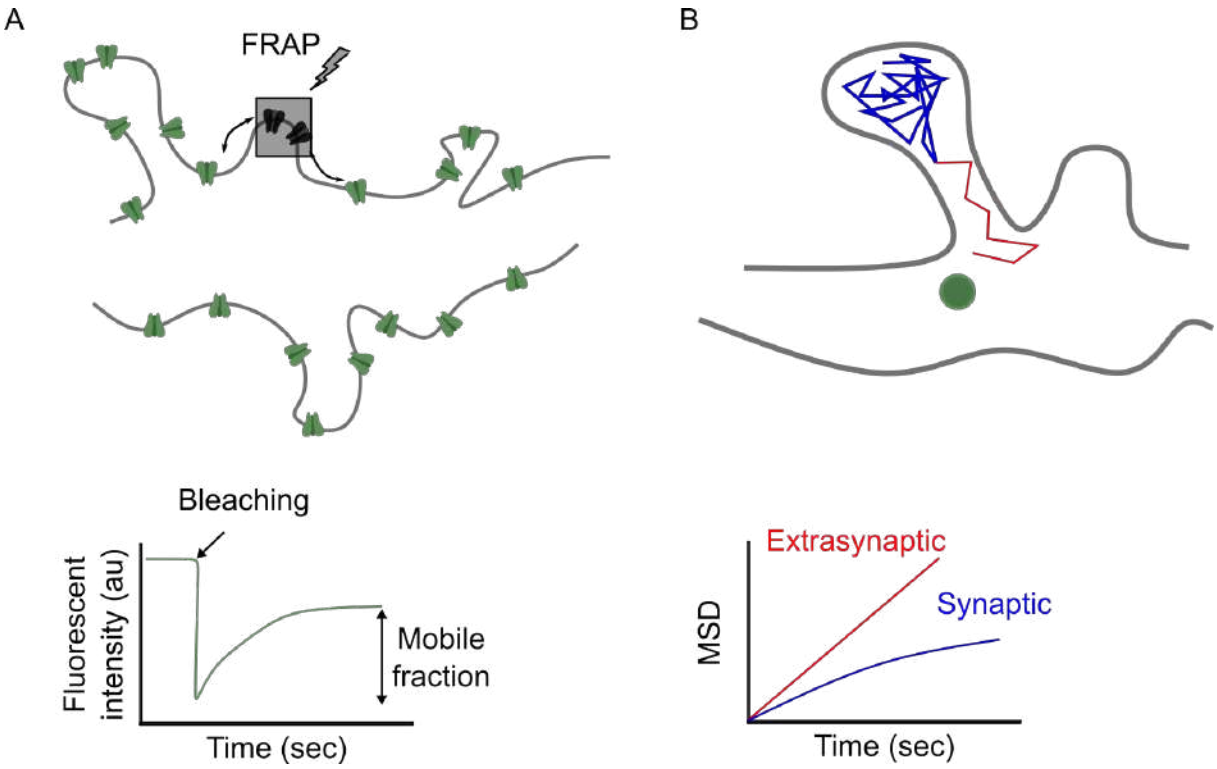

Figure 3.2.: **Methods to study receptor motion. A)** Fluorescence recovery after photobleaching (FRAP) involves locally photobleaching fluorescently labeled receptors and monitoring the recovery of fluorescence in the bleached area to determine both the rate of receptor movement and the proportion of immobile receptors [9]. **B)** Time-lapse imaging of single molecules in live cells enables the tracking of individual receptors. By analyzing the surface explored by these receptors over time, researchers can measure their movement patterns and diffusion rates. Extrasynaptic receptors generally exhibit free Brownian motion, characterized by a linear MSD curve, while synaptic receptors display confined movements [164]. The figure is adapted from [65].

suited for tracking endogenous receptors, which are often expressed in low copy numbers.

3.1.2. Active transport

The viscous nature of the intracellular environment makes it unsuitable for long-distance trafficking via purely diffusive processes. Owing to the lack of direct measurement of diffusion rates of receptor-containing vesicles, the estimated diffusion rates are in the order of $0.01 \mu m^2/s$, with significant confinement [91]. Intracellularly, a more efficient way of transporting cargo is through molecular motors, such as kinesin and Dynien, which consume energy in the form of Adenosine Triphosphate (ATP). For short distances, myosin motors can move cargo along the actin cytoskeleton with high specificity [54]; however, myosin-based transport is not suited for long-range transport. Microtubule-based systems are preferred for long-distance intracellular

transport, such as transport between various cell organelles (like Endoplasmic Reticulum (ER), and Golgi) as they allow directional movements at speeds of up to 5 $\mu m/s$. Few studies have examined glutamate receptor transport due to imaging challenges with fluorescently tagged receptors. The first detailed report of intracellular transport of AMPAR was studied in nematode, Caenorhabditis elegans[85].

In a recent study, Hangen and colleagues have highlighted the microtubule-based rapid transport of AMPAR [72]. Intriguingly, they observed a bidirectional movement of vesicles containing AMPARs. This bidirectional transport enables efficient distribution of receptors and ensures their availability across the dendrite for rapid, on-demand delivery during activity-dependent plasticity. They further highlighted that synaptic activity-driven calcium influx can arrest vesicles transporting AMPAR, which they hypothesized could be for the surface insertion of AMPAR to meet synaptic demands. They also showed that during prolonged periods of elevated synaptic activity, intracellular AMPAR transport increases significantly, likely to replenish the dendritic receptor pool [72]. These findings, collectively, indicate that neurons have evolved a robust activity-dependent regulation of glutamate receptor intracellular transport [72, 151] hinting towards a pivotal role in controlling receptor availability during synaptic plasticity and warranting further examination.

3.1.3. Exocytosis, endocytosis, and degradation

Efficient vesicular trafficking in the cytoplasm is achieved through interactions with actin, requiring energy expenses. These interactions generate the essential push for vesicle biogenesis, propulsion over short-distance through the cytoplasm to their target destinations [95, 73], and is crucial for recycling of receptors via endocytosis and exocytosis.

The actin motor protein myosin VI is specifically required for activity-induced, clathrin-mediated endocytosis of AMPARs during synaptic LTD in hippocampal neurons [122] and at parallel fiber-Purkinje cell synapses [179]. Since dendritic spines are densely packed with actin filaments and largely lack microtubules, myosin-driven movements are likely predominant in these compartments. During long-term potentiation (LTP) induction, myosin Vb or Va interacts with GluA1-containing recycling endosomes in the dendritic shaft, facilitating their transport into spines. Within the spines, these recycling endosomes fuse with the plasma membrane, enabling surface insertion of GluA1 AMPARs and contributing to the spine surface growth

associated with LTP [181]. It remains unclear whether actin-based transport is also involved in longer-range movements within dendrites.

AMPARs, like many other surface proteins, are internalized and stored in intracellular compartments such as an early endosome. They can also be stored in late endosomes following endocytosis, where they are degraded through lysosomal pathways [113]. Finally, they can be recycled back to the surface via recycling endosomes [74, 113]. Their reinsertion or degradation seems to be dependent on the activation of NMDAR and phosphorylation activity of PKA as activating AMPAR without NMDAR activation targets AMPAR to late endosome and lysosomal degradation [53].

3.1.4. Local translation

Another major pathway for a neuron to supply proteins to distal dendrites is to synthesize proteins locally in the dendrites. This can be achieved by transporting mRNAs and protein synthesis machinery to the dendrites. The first evidence that mRNA present in dendrites is translated into proteins essential for synaptic plasticity was reported in [93]. Since then, research has progressively highlighted the significance of locally synthesized proteins and their critical role in long-term plasticity [51, 163, 16]. As demonstrated by these studies, the continuous presence of mRNA within the dendritic arbor enables the consistent production of newly synthesized proteins. The steady synthesis in dendrites ensures a uniform distribution of proteins across the dendritic arbor while minimizing the overall protein demand in the dendrite [58].

The reduction of protein needs comes with the additional cost of transporting mRNAs into the dendritic branches. Again, this can happen with the methods of intracellular motion described above, mainly with passive diffusion and active transport. In addition to transporting the mRNA the protein synthesis machinery also needs to be localized in the dendrites. The number of ribosomes present in the synapses of a hippocampal neuron ranges from zero to eight per synapse [155], enabling individual synapses to respond and adapt to stimuli in various ways.

For AMPARs, whether local translation plays a critical role in shaping their distribution remains unclear. Recent evidence suggest local translation under plasticity condition [66, 92]. However, experimental work also argues that mRNA encoding for the pore-forming subunits of AMPAR are largely somata-enriched [63] under basal conditions. One way to reconcile these differences would be to consider enhanced mRNA translocation to the dendrites under plasticity

demands for mRNAs that are somatically enriched such as AMPAR. For this reason, we studied mRNA localization for two major pore-forming subunits of AMPAR, namely the GluA1 and GluA2 subunits.

3.2. mRNA density of AMPA receptor subunits

As discussed above, diffusion and active transport are well-established mechanisms that regulate AMPAR distribution along neuronal dendrites Fig. 3.1.A-B. However, the role of local transport in the trafficking of AMPAR subunits remains poorly understood. To explore the contribution of local protein synthesis to AMPAR availability in dendrites, we began by examining the distribution of mRNAs encoding AMPAR subunits.

For this, my collaborators, Dr. Anne-Sophie Hafner, performed fluorescent in-situ hybridization (FISH) against the *Gria1* and *Gria2* mRNA-coding for the GluA1 and GluA2 subunits of AMPAR. I have provided the details on the FISH experiments in Appendix section A.14. Next, I analyzed this FISH dataset and quantified endogenous levels of *Gria1* and *Gria2* mRNA molecules in hippocampal cultured neurons Fig. 3.3.A using the SpyDen tool's puncta analysis pipeline described in section 2.4.

First, I quantified the fraction of mRNA of *Gria2* in the neuronal somata and dendrite and compared it against *Camk2a* mRNA, an mRNA species well known to be localized in dendrites [22, 171, 58], detected in the same neuron. I found that while a majority of *Camk2a* mRNA (more than 70%) was localized in the dendrites, only a small, 18% of the *Gria2* mRNA was localized in the dendrite while the remaining 82 % was localized in the somata. Fonkeu and colleagues have shown that even though *Camk2a* mRNA distribution declines as one moves away from the somata, it is still sufficient to satisfy protein needs [58]. So, I asked if the small fraction of *Gria2* mRNA shows similar characteristics. To answer this, I binned the dendritic fraction of *Gria2* mRNAs based on their distance from the soma or origin of the dendrite. Then, I fitted this distribution with the exponential function to compare the relative amount of mRNA at 100 μm distance Fig. 3.3.C. This analysis showed a fast decline and relatively low abundance of *Gria2* mRNA. Specifically, I observed that the *Gria1* mRNA levels dropped by a large, 98% while the *Camk2a* mRNA only showed a moderate 42% decrease Fig. 3.3.C.

Then, I performed the same set of analysis for the *Gria1* mRNA. In this case, also, a small $\approx$ 25 % of the *Gria1* mRNA was localized into the dendrite compared to the *Camk2a* mRNA that

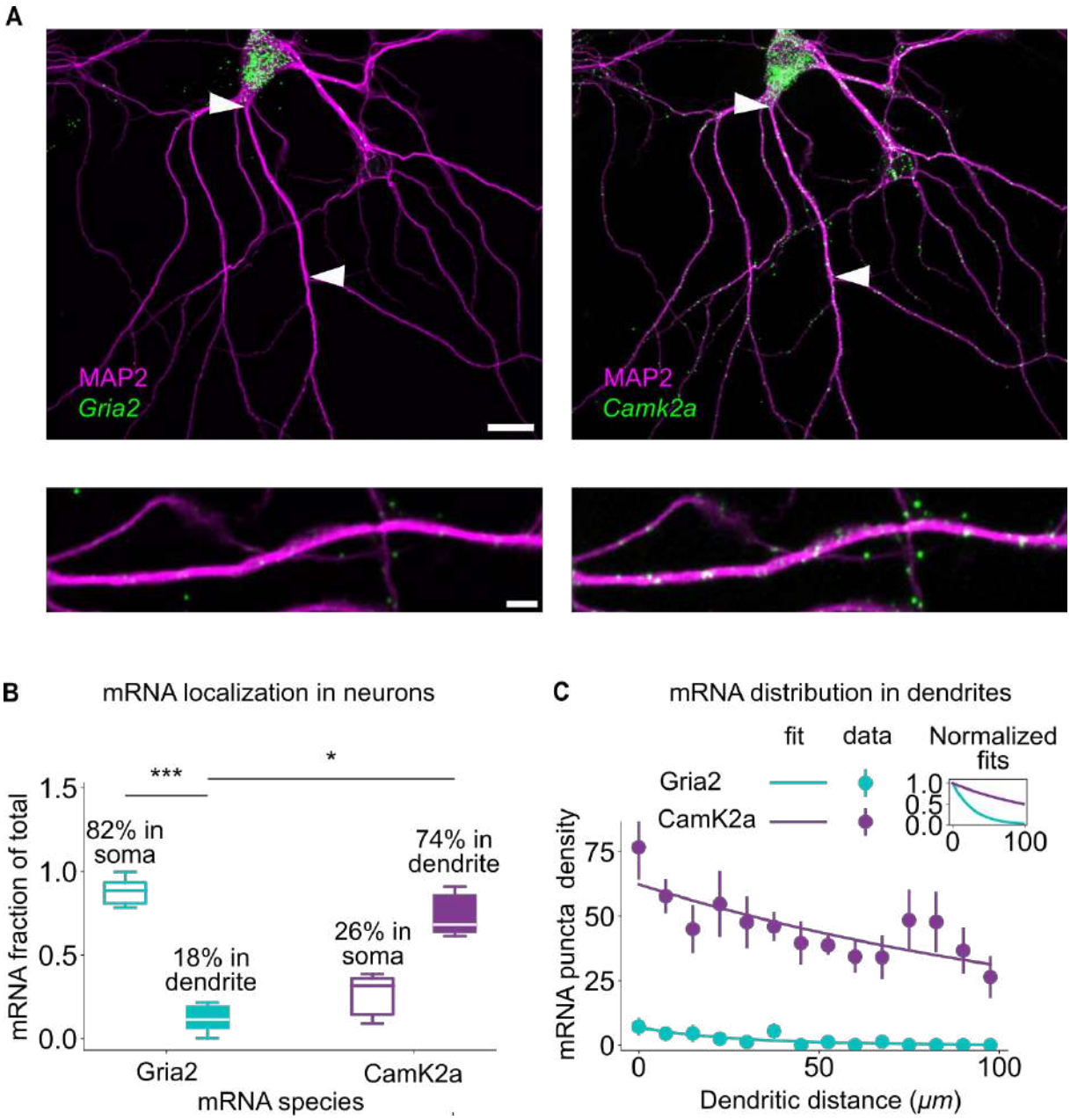

Figure 3.3.: ***Gria2* mRNA is predominantly enriched in soma.** **A)** *Top*: Rat cultured hippocampal neurons at 18-21 DIV labeled using fluorescence *in situ* hybridization to detect *Gria2* (left, green) and *Camk2a* mRNAs (right, green) and immunostained for MAP2 (magenta). Scale bar = 20 μm. *Bottom*: The zoomed image of the representative dendritic segment shows a considerably small number of *Gria2* mRNA (left) compared to abundant *Camk2a* mRNA (right). Scale bar = 5 μm. **B)** Box plot of the somatic (hollow) and dendritic (filled) fraction of total mRNA for *Gria2* computed as a fraction in a compartment with respect to the total mRNA count in a neuron (18 cells, p-value: 6.9×10^{-5}) and *Camk2a* (23 cells, p-value: 0.23), *Gria2*-dendrite vs *Camk2a*-dendrite (p-value:0.02). **C)** Fitting an exponential function to mRNA puncta density distribution for *Gria2* ($n = 12$ dendrites, exponent *Gria2* = -0.04 $\pm$ 0.009) compared to the *Camk2a* distribution ($n = 33$ dendrites, exponent *Camk2a* = -0.006 $\pm$ 0.001), revealed rapid drop in *Gria2* mRNA. *Inset*: I show normalized fit of *Gria2* mRNA distribution compared to *Camk2a*. The figure is adapted from [178].

had ≈ 50% of its in the dendrite Fig. 3.4.A-B. Also, the dendritic distribution of *Gria1* mRNA showed a similar trend as the *Gria2* mRNA where at a distance of $100\mu m$, the concentration of *Gria1* mRNA dropped by 96% Fig. 3.4.C.

Overall, relatively low abundance of *Gria1* and *Gria2* mRNA, coupled with their rapid decline with the dendritic distribution challenges the possibility of local translation as a mechanism for maintaining AMPAR protein levels at distal dendritic sites. Previous studies have reported local synthesis of the AMPAR subunit GluA1 in proximal dendrites, within a few tens of microns from the soma, in response to BDNF stimulation [92] and secreted amyloid precursor protein-alpha-mediated LTP [107]. These findings align with my results regarding the presence of *Gria1* and *Gria2* mRNAs in the proximal dendrites near the soma and do not contradict the absence of local GluA1 and GluA2 synthesis in more distal dendritic regions observed in my analyses. Notably, my results are in line with the recent work of Glock and colleagues, who examined the neuronal translatome by comparing the somatic layer and neuropil (primarily comprising dendrites, axons, and glia) in the CA1 region of the hippocampus. Their data on RNA footprinting showed minimal coverage for *Gria1* and *Gria2* in the neuropil but substantial coverage in the somatic layer [63]. Next, I studied how the GluA2 protein is distributed along the dendrite.

3.3. Protein density of AMPA receptor subunits

Experimental studies have revealed that the abundance of AMPAR along the dendrites often increases towards the distal ends [5, 150], which is shown to depend on GluA2 subunit of AMPAR [150]. This phenomenon is also known as distance-dependent scaling of AMPARs and has been observed for other ion channels as well, such as HCN channels [109] and voltage-gated potassium channels Kv4.2 [11]. However, the studies on AMPAR used AMPAR-mediated current amplitude as a proxy for AMPAR copy-number, which is considered an indirect measure of AMPAR abundance. Hence I decided to test this using protein-antibody labeling of GluA2.

For this, I analyzed the density of GluA2 AMPAR protein to see if my findings align with previous studies. To test this, my collaborator, Dr. Anne-Sophie Hafner, performed protein antibody labeling of total GluA2-containing AMPARs after fixation and permeabilization and acquired images using confocal microscopy. In Fig. 3.5.A, I show an example image from this dataset. I measured the fluorescent intensity of endogenous GluA2-containing AMPARs within

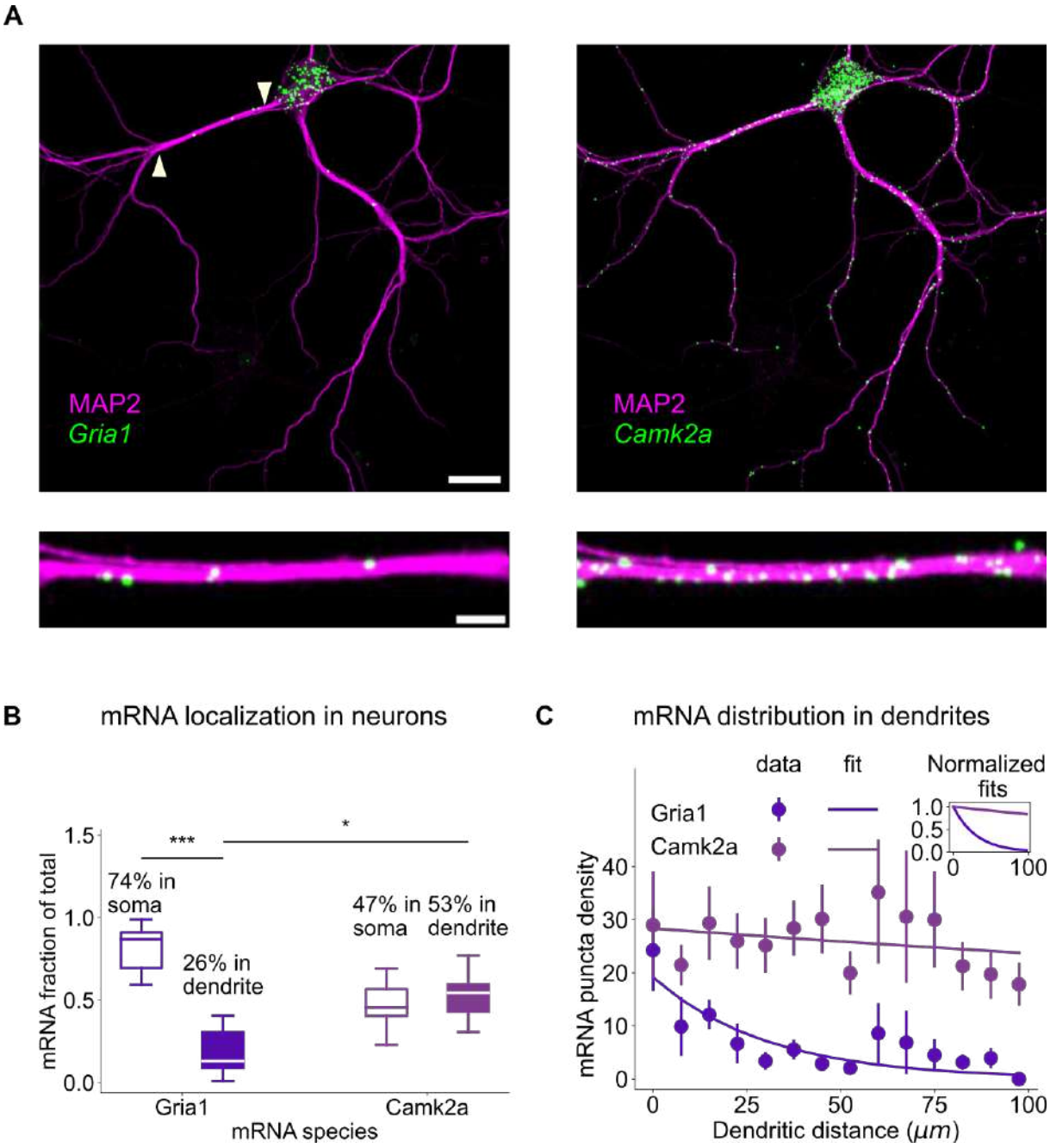

Figure 3.4.: ***Gria1* mRNA is predominantly localised in soma.** **A)** *Top*: 18-21 DIV cultured rat hippocampal neurons at processed for FISH against *Gria1* (left, green) and *CamK2a* mRNA (right, green) and fluorescently immunostained (FI) MAP2 (magenta). Scale bar = 20 μm. *Bottom*: Zooming into a representative dendrite shows a smaller number of *Gria1* mRNA (left) in comparison to *CamK2a* mRNA (right). Scale bar = 5 μm. **B)** Somatic (hollow) and dendritic (filled) fraction of total mRNA for *Gria1* (19 cells, p-value: 1e-06) and *CamK2a* (19 cells, p-value: 1), *Gria1*-dendrite vs *CamK2a*-dendrite (p-value:0.019). **C)** Exponential fit of mRNA puncta density distribution for *Gria1* ($n = 12$ dendrites, exponent *Gria1* = -0.03 $\pm$ 0.007) compared to the *CamK2a* distribution ($n = 33$ dendrites, exponent *CamK2a* = -0.001 $\pm$ 0.001), see Methods for mRNA exponential fit. *Inset*: Normalized fitted *Gria1* mRNA distribution compared to *CamK2a*. The figure is adapted from [178].

the first 100 μm of the dendrites to analyze their dendritic distribution. My analysis revealed no significant trend in receptor density along the first 100 μm of dendritic length Fig. 3.5.B.

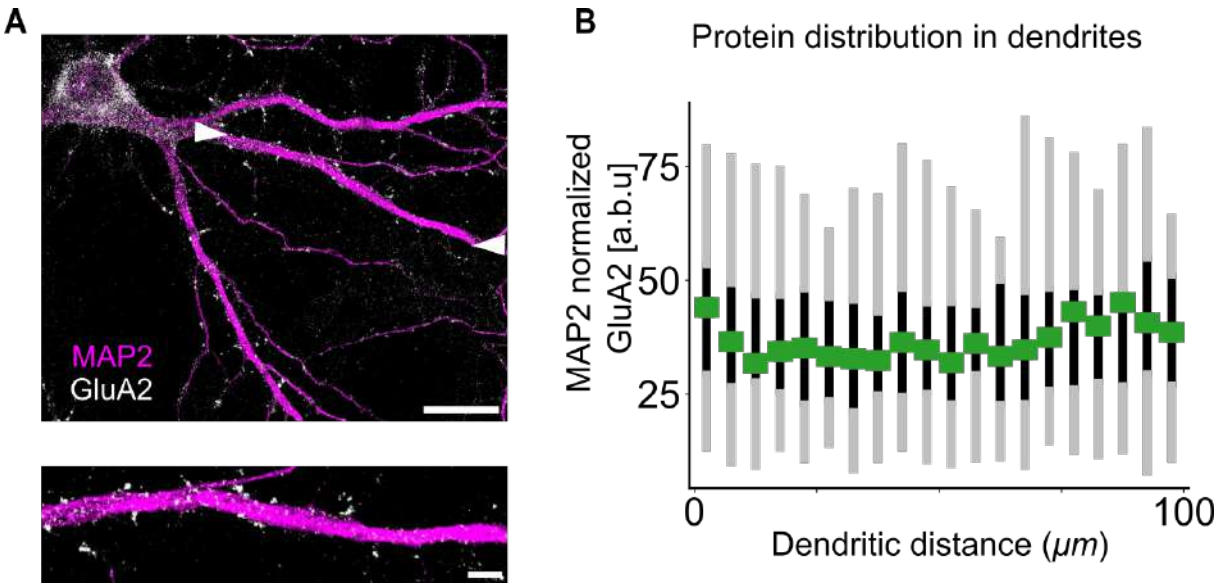

Figure 3.5.: **GluA2 protein showed uniform density in dendrites up to 100 μm. A)** *Top*: DIV 18-21 cultured rat hippocampal neurons performed with antibody labeling of FI MAP2 (magenta) and GluA2 (white). *Bottom*: Zoomed in representative dendritic stretch showed a homogeneous GluA2 protein distribution along the first 100 μm. Scale bar = 20 μm. **B)** GluA2 intensity normalized by the MAP2 intensity (5 μm bins, median: green squares with IQR). A sum of exponential fit revealed a minimal 5% drop in GluA2 density. The figure is adapted from [178].

3.4. Model of total GluA2-containing AMPAR

Recent modeling work can not recapitulate the findings that AMPARs exhibit a uniform concentration in the first 100 μm and an increasing concentration towards the distal tip. These modeling studies suggested an exponentially decaying profile of protein over long-range [50, 58], especially for proteins that lack local synthesis. However, in these models, protein diffusion was used as the mode of protein trafficking, and one of the key mechanisms, active transport, was not considered.

► Diffusion, active transport and degradation

Hence, I next developed a computational model that consisted of the known mechanisms of AMPAR trafficking, mainly passive diffusion, active transport, and degradation, to study their distribution along a model dendrite. I considered a finite dendrite of length L. Next, I described

the protein density $\rho(x,t)$ in this model dendrite to evolve using the Partial differential equation (PDE)s:

$$\frac{\partial \rho(x,t)}{\partial t} = D\frac{\partial^2 \rho(x,t)}{\partial x^2} - V\frac{\partial \rho(x,t)}{\partial x} - \lambda\rho(x,t). \tag{3.2}$$

In this equation, the first term on the right-hand side (RHS) describes the passive diffusion of AMPARs with a constant rate of diffusion (D). The second term on RHS describes the active transport, and the last term on RHS describes a constant rate of degradation throughout the model dendrite. I would like to note that in this model, the rate of diffusion, active transport velocity, and degradation rate are considered to be constant along the dendrite. Next, I analyzed the distribution of proteins at equilibrium - meaning the distribution observed after a time significantly longer than all relevant timescales of the system. What that means for the model in Eq. 3.2, is that the system doesn't change with time and Eq. 3.2 converts into an Ordinary differential equation (ODE), described as:

$$0 = D\frac{d^2 \rho(x)}{dx^2} - V\frac{d\rho(x)}{dx} - \lambda\rho(x). \tag{3.3}$$

The resulting ODE is of 2nd order and, with two boundary conditions, can be fully solved. Next, I described the two boundary conditions and the biological intuition behind them.

▶ Boundary conditions

Here I focused on the boundary conditions that can be imposed on the diffusion-advection-degradation equation at equilibrium (in Eq. 3.3). Assuming a finite dendrite of length L, $x \in (0, L)$, the boundary conditions are $\Phi(0) = J_{influx}$ assuming a constant influx of new receptors from the soma at the left boundary of the model dendrite. The second boundary condition I imposed is $\Phi(L) = 0$, which represents no flux at the tip of the dendrite assuming the dendrite is closed at the distal tip and no receptor can escape from it. With these boundary conditions, the problem can be described using the following ordinary differential equations

$$
\begin{aligned}
D\frac{\partial^2\rho(x)}{\partial x^2} - V\frac{\partial\rho(x)}{\partial x} - \lambda\rho(x) &= 0 \\
\Phi(0) &= J_{influx} \\
\Phi(L) &= 0.
\end{aligned}
\tag{3.4}
$$

The system of equations in Eq. 3.4 can be analytically solved, see Appendix section A.5.

$$
\rho(x) = \frac{J_{influx}}{e^{-K_1 L} - e^{-K_2 L}} \left(\frac{e^{-K_2 x - K_1 L}}{V + DK_2} - \frac{e^{-K_1 x - K_2 L}}{V + DK_1} \right). \tag{3.5}
$$

In the appendix section A.5, I show how to obtain the solution of equation Eq. 3.3 at equilibrium.

► Global trafficking parameters

Next, I fitted the model described in Eq. 3.4 to understand which trafficking parameters could explain the uniform distribution and reconcile with the earlier reports on AMPAR distribution with an increase toward the distal end [150, 5]. I describe the details of the fitting procedure in the Appendix section A.12. Upon fitting the model, I measured a marginal 7% decrease in GluA2-containing AMPAR at 100 μm distance from the soma.

Previous modeling studies have demonstrated that active transport velocity can significantly influence the distribution of molecules along dendrites [58, 19]. AMPARs, as transmembrane proteins, are transported within vesicles in the cytoplasm through microtubule-mediated transport. These vesicles move bidirectionally, with speeds averaging 1.46 $\mu m/s$ in both anterograde and retrograde directions [72]. However, experimental works have not established a net anterograde active transport velocity for unmodified receptors.

To address this, I initially treated the active transport velocity as an unknown parameter in my mathematical model (see Supplemental Information). Subsequently, I assumed that the net active transport velocity was zero (i.e. $V = 0$ in equation Eq. 3.3), meaning anterograde and retrograde transport fully compensate for each other. I then analyzed whether modulation in diffusion parameters and protein half-life could account for the experimentally observed distribution of GluA2 receptors in our dataset Fig. 3.5B, characterized by an almost constant

concentration near the soma and an increase toward the dendritic ends.

I first investigated how changing the diffusion rate changed the distribution of GluA2-containing AMPARs in model dendrite. For this, I set the active transport velocity, V, to 0 and protein half-life to 3.12 days [46] and changed the diffusion rate, D.

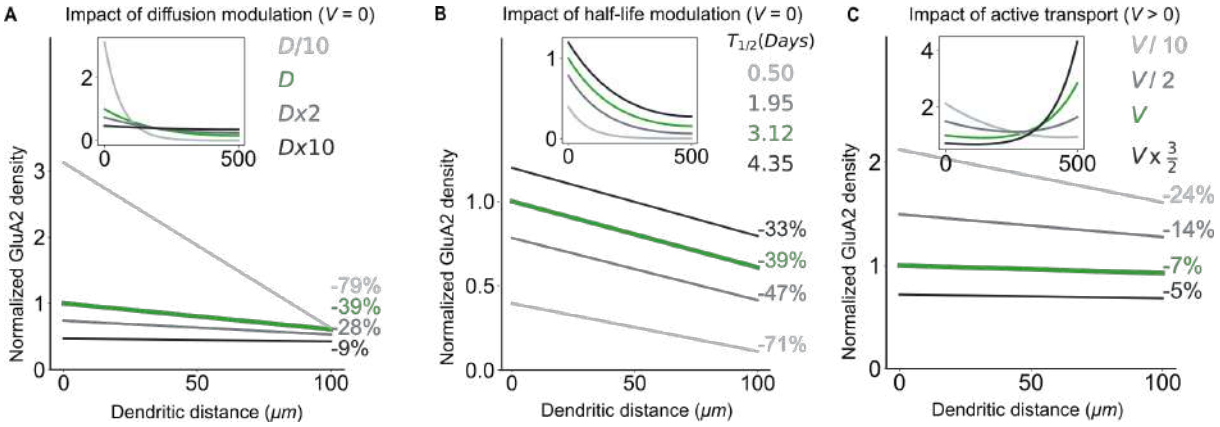

Figure 3.6.: **AMPAR GluA2 subunits require biased active transport to compensate for the lack of their local synthesis. A)-C)** Steady state distributions of GluA2 from the protein trafficking dynamics model proposed in section 3.4. Elevating the reported diffusion constant (D) of GluA2 10 times than the reported value leads to a 9% GluA2 decrease at 100 μm but does not distance-dependent scaling at 500 μm (inset). **B)** and **C)** Active transport $V = 0$. **B)** The half-life ($T_{1/2}$) of GluA2 protein increased over the reported maximum of 4.35 days cannot provide constant GluA2 distribution observed in the data (shown in Fig. 3.5. **C)** Biased active transport of $V = 1.4 * 10^{-3}$ μm/s leads to an observed 7% decrease in GluA2 protein concentration and distance-dependent scaling at 500 μm (inset). The figure is adapted from [178].

I used diffusion constants ranging from to $10^{-2}\mu m^2/s$ to $1\mu m^2/s$, starting with the experimentally reported value of [14]. At this value, the model showed a 39% decrease in GluA2 concentration at a distance of $100\mu m$ from the soma (Fig. 3.6.A). When I reduced the diffusion constant by a factor of 10, still keeping it in the experimentally reported range [185], this led to a 79% decrease in GluA2 concentration at the same distance (Fig. 3.6.A). Conversely, increasing the diffusion constant by a factor of 10 an order of magnitude higher than what is typically measured at the cell surface resulted in only a 9% decrease at $100\mu m$, closely matching the experimentally observed reduction in GluA2 concentration (Fig. 3.6.A).

Further increasing the diffusion constant by two orders of magnitude led to a minimal reduction of ≈30% in GluA2 concentration, with the distribution remaining only slightly flatter than that observed with a single order of magnitude increase. Despite trying diffusion coefficients spanning several orders of magnitude, none of the tested values for GluA2 diffusion were able to replicate the experimentally reported increase in AMPAR concentration observed in distal

dendritic regions (Fig. 3.6.A, inset) [150, 157].

Next, I asked if protein half-life can explain the observed experimental distribution of GluA2. For this, I again set the active transport velocity, V, to zero and used an intermediate value of diffusion coefficient, D, equal to $0.1\mu m^2/2$ reported in [14]. Then, I set the half-life of GluA2 protein in my model to values between 1.95 to 4.35 days as reported in experimental studies [47, 33]. When I set the half-life to 1.95 days, the GluA2 concentration decreased by 47% at a dendritic distance of $100\mu m$. This reduction was slightly mitigated to ≈40% when the half-life was increased to the maximum reported value of 3.12 days. Longer half-life values result in an extended lifetime for the molecules, allowing more of them to reach distal dendritic locations through diffusion.

However, even with a 39% decrease in GluA2 concentration at 100 μm, the reduction remained substantially higher than obtained in our experiments, which was a 7% decrease. Further increasing the GluA2 half-life to 4.35 days (see Table A.5) reduced the drop to 33% at 100 μm (Fig. 3.6.B). While extending the GluA2 half-life increased its dendritic concentration, only non-physiological values were able to replicate the experimentally measured GluA2 distribution.

Additionally, when analyzing GluA2 distribution curves beyond 100 μm, we did not observe the expected increase toward the distal dendritic ends (Fig. 3.6.B, inset). These findings indicate that modifying the half-life parameter alone, in the absence of active transport, is insufficient to explain the experimentally observed distribution pattern of GluA2.

Since neither increasing the GluA2 diffusion rate nor half-life alone was sufficient to replicate the reported distribution of AMPARs, I next studied the potential role of biased active transport velocity along microtubules. Initially, I assumed an active transport velocity of zero, reflecting the non-biased bidirectional nature of microtubule-based transport in dendrites [165]. However, in the next step, I introduced a positive active transport velocity, V, creating a bias for the anterograde movement of intracellular vesicles toward the distal tips of dendrites.

To test this hypothesis, I set the receptor half-life to 3.12 days and adjusted both the active transport velocity constant, V, and the diffusion constant, D, to fit the experimentally measured GluA2 fluorescence distribution.

I decided to fit the two constants, V and D, to get an initial value of this parameter as there is a lack of evidence of a net anterograde active transport for AMPAR. I have provided the details of the parameter fitting in Appendix section A.12.

The best fitted values for active transport parameter, V, came out to be $1.4 * 10^{-3} \mu m/s$ and the diffusion rate, D, was equal to $0.22 \mu m/s$ Fig. A.2. Using these physiologically plausible parameter values, the model produced a GluA2 receptor distribution with a 7% decrease at $100 \mu m$ from the soma (Fig. 3.6.C), followed by a steady increase in receptor concentration that reached 180% at 500 μm (Fig. 3.6.C, inset). Interestingly, fitting the active transport to just the first $100 \mu m$ in my model automatically predicted an increase in GluA2 concentration towards the distal tip. To investigate the impact of globally reducing the active transport velocity on the GluA2 distribution, I decreased its value by factors of 2 and 10.

As the active transport velocity decreased, I observed an accumulation of receptors in the proximal dendritic regions near the soma (Fig. 3.6.C). When the active transport velocity was reduced by a factor of 10, the gradual increase in GluA2 concentration in distal dendrites disappeared completely (Fig. 3.6.C, inset). Conversely, increasing the fitted active transport velocity by a modest factor of 3/2 resulted in a dramatic 500% rise in GluA2 concentration at the dendritic tip, demonstrating that even small increases in active transport velocity can cause a significant accumulation of GluA2 at distal dendritic sites (Fig. 3.6.C, inset).

Overall, my computational model and experimental data analysis emphasize that active transport could explain the experimentally observed GluA2 protein distribution. Next, I moved on to characterizing the local modes of trafficking Fig. 3.1C, namely the endo-and exocytosis of receptors and their incorporation into synapses.

► Endocytosis and exocytosis of AMPAR

Given that the number of AMPARs in the PSD directly correlates with synaptic strength, I next investigated the mechanisms underlying AMPAR insertion into the PSD under both basal conditions.

To achieve this, I focused on small dendritic compartments, including dendritic spines, and examined AMPAR trafficking between the cytoplasm (intracellular compartment), the plasma membrane (surface), and PSD. AMPAR exocytosis occurs near synaptic sites, such as the spine head or adjacent dendritic shaft, allowing AMPARs to enter the PSD via lateral diffusion in the plasma membrane [121]. By modeling the rates and locations of endocytosis, exocytosis, and synaptic trapping, I wanted to better understand how these processes influence synaptic plasticity.

Importantly, the trafficking speed and residence time (lifetime within a compartment) of transmembrane proteins differ between the plasma membrane and the cytoplasm [65]. Therefore, it is essential to model intracellular and surface proteins separately to accurately estimate their redistribution.

3.5. Three population model of AMPAR trafficking

In thi section, I describe the extended, three-population model that I developed to study AMPAR trafficking in detail. The three compartments that I modeled are: the cytoplasm, the plasma membrane, and the PSD. The protein density in each of these three compartment are henceforth termed as ρ_c, ρ_s and ρ_{psd} respectively (see Fig. 3.7.B). Using this extended model, I analyzed how endocytosis, exocytosis, and diffusional trapping at the PSD shape AMPAR distribution across these compartments.

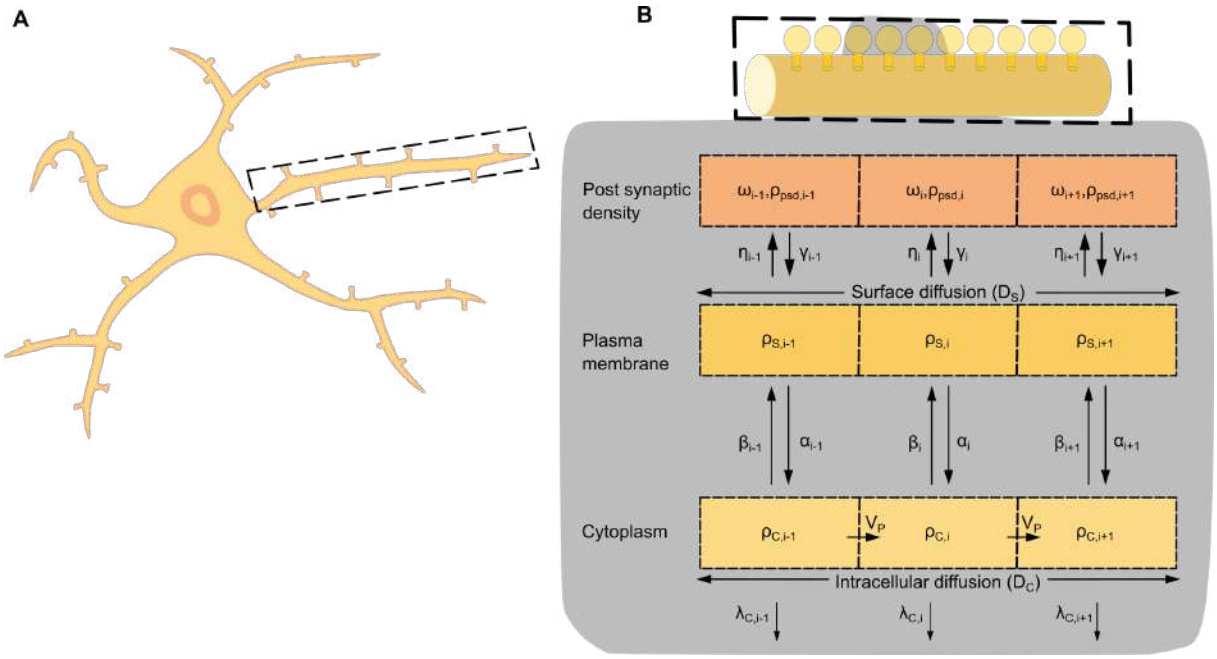

Figure 3.7.: **Schematic diagram of the three population model and rates of exchange between them A)** Schematic diagram of a neuron . **B)** Schematics of the three compartmental mathematical models with the rates of exchange between them.

I describe the three population models using the system of coupled partial differential equations:

$$\frac{\partial \rho_c(x,t)}{\partial t} = D_c \frac{\partial^2 \rho_c(x,t)}{\partial x^2} - V_p \frac{\partial \rho_c(x,t)}{\partial x} - \lambda_c \rho_c(x,t) - \beta \rho_c(x,t) + \alpha \rho_s(x,t) \tag{3.6}$$

$$\frac{\partial \rho_s(x,t)}{\partial t} = D_s \frac{\partial^2 \rho_s(x,t)}{\partial x^2} - \lambda_s \rho_s(x,t) + \beta \rho_c(x,t) - \alpha \rho_s(x,t) \tag{3.7}$$

$$- \eta \rho_s(x,t)(\omega - \rho_{psd}(x,t)) + \gamma \rho_{psd}(x,t)$$

$$\frac{\partial \rho_{psd}(x,t)}{\partial t} = \eta \rho_s(x,t)(\omega - \rho_{psd}(x,t)) - \gamma \rho_{psd}(x,t) \tag{3.8}$$

In this three-population extended model, I can describe the distribution of AMPAR in the cytoplasm, plasma membrane, and PSD. For the cytoplasmic compartment, the density of receptors is shaped by the diffusion constant (D_c), intracellular transport (V_p), and the degradation rate of the receptors (λ_c). The dynamics of the receptors in the plasma membrane is shaped entirely by lateral diffusion (D_s) through Brownian motion. The local trafficking between the plasma membrane and intracellular receptors is modeled using the coupling terms representing exocytosis (β) and endocytosis (α).

Synaptic uptake plays a critical role in determining AMPAR availability at different dendritic locations. Surface receptors can become trapped in the PSD by binding to anchoring proteins, such as PSD-95, with an incorporation rate (η). These trapped receptors can eventually unbind from anchoring proteins and exit the PSD at a rate (γ). Finally, I assumed that each synapse has a maximum capacity, defined by ω, for accommodating AMPARs. This maximum capacity is dictated by the number of slots within the PSD. These slots are structural components composed of proteins like PSD-95, which anchor AMPARs in the PSD and limit their mobility [147, 69].

In this three-population model, I have made the following assumptions:

- All the trafficking parameters in the model are assumed to be constant and do not depend on the location in the dendrite. For example, the degradation rate λ_c has the same value at each location in the dendrite.

- The exchange between the extra-synaptic and synaptic receptor occurs because of lateral diffusion and binding and unbinding of receptors to the PSD structure proteins such as PSD-95 [65]. Here, I have modeled that collective motion as a hopping-like motion such that receptors can hop into the PSD, leading to their incorporation into the synapse, and eventually receptors can hop out of the PSD and hence return to the extrasynaptic pool of

receptors.

- The nanoscale organization of the PSD was not considered for simplicity reasons, which can influence the diffusional trapping of AMPARs inside the PSD (see [96, 65]).

Next, I began characterizing the values of the parameters for the three population models. For this, first, I solved the system of PDEs described in Eq. 3.6 - Eq. 3.8 at equilibrium, meaning that the concentrations did not change with time. In the Appendix section A.6, I have described the mathematical details on deriving the distribution of the three populations.

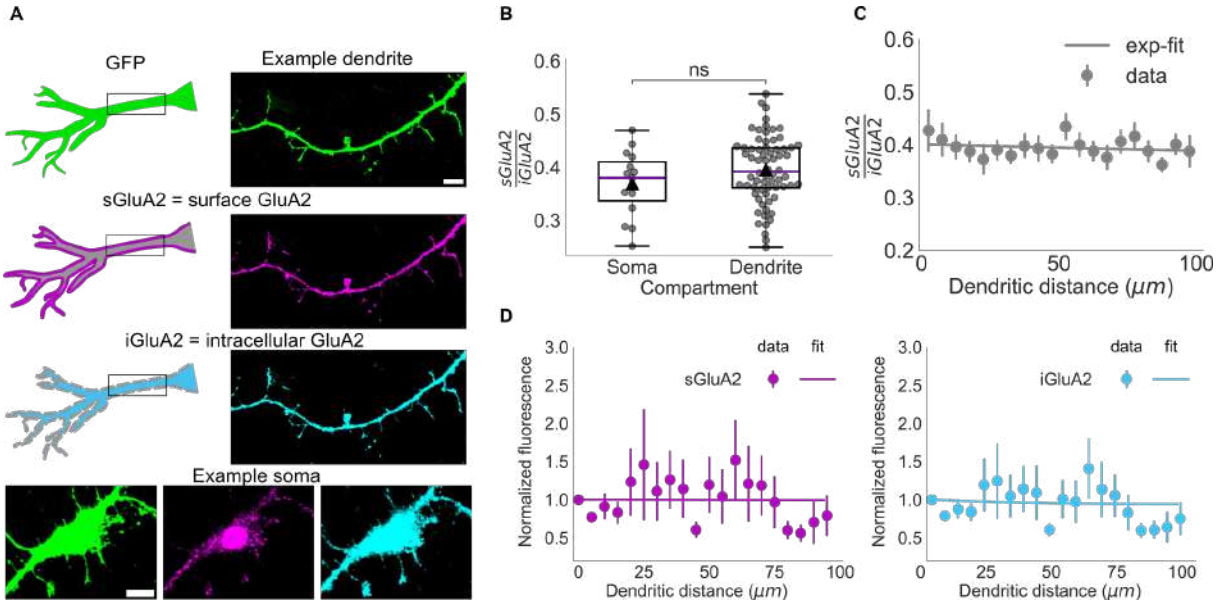

Figure 3.8.: **The endogenous distribution of GluA2-containing AMPARs. A)** Schematic representation of antibody labeling (top left) alongside example images used to quantify intracellular and surface protein concentrations in dendrites (top right) and somata (bottom). The GFP signal (green) highlights the intracellular region. The iGluA2 signal (cyan) represents GluA2 subunits within the cytoplasm, while the sGluA2 signal (magenta) corresponds to GluA2 subunits localized to the cell surface (scale bars 10μm). **B)** Fitting of the global transport parameters (D_c, D_s, V_p) to the surface and intracellular GluA2 fluorescent intensity. *left:* Dendritic distribution of soma-normalized GluA2 confined to the surface (sGluA2 data and model fit,) and *right:* intracellular GluA2 (iGluA2 data and model fit, cyan, right). $N_{Dendrites} = 11$. **C)** Ratio of fluorescent intensity between surface and intracellular GluA2 was 0.37 $\pm$ 0.062 in somata (mean $\pm$ std, N = 15) and 0.40 $\pm$ 0.063 in dendrites (mean $\pm$ std, N = 69, p = 0.35, z-stat=0.86). **D)** Distribution of the ratio of surface to intracellular GluA2 fluorescent intensity ratio fitted with an exponential function shows an insignificant decrease of 3% at 100 μm (exponent = 2.9×10^{-4}). Figure is adapted from [178].

Then, I analyzed the experimental data on fluorescent labeling of GluA2-containing AMPARs in the cell cytoplasm, on the neuronal surface, and in the spines. The experimental data was

acquired by my collaborators, Maximilian Kracht and Prof. Amparo Acker-Plamer. They performed immunolabeling of endogenous surface and intracellular GluA2 Fig. 3.8. Their labeling protocol utilized secondary antibodies with different fluorophores applied before and permeabilization in fixed cultured hippocampal neurons. To visualize the cell structure, they expressed a green fluorescent protein (GFP) cell transfection technique. I have provided the complete experimental protocol in Appendix section A.14.

First, I characterized the ratio of exocytosis to endocytosis rates in my three populations model that drives continuous recycling of GluA2-containing AMPARs between the plasma membrane and the cytoplasm. In my three population model (described in Eq. 3.6 - Eq. 3.8) under equilibrium condition, the ratio of exocytosis to endocytosis rates (β/α) corresponds to the ratio of total protein in the plasma-membrane to cytoplasm, i.e.

$$\frac{\beta}{\alpha} = \frac{\int_0^L \rho_s(x)dx}{\int_0^L \rho_c(x)dx} \tag{3.9}$$

I have described the step to obtain this ratio in Eq. A.31 in the Appendix section A.12.

My data analysis showed that; under basal conditions, cytoplasmic GluA2 levels were higher than surface GluA2 in both somata and dendrites Fig. 3.8.B, consistent with previous findings [12, 128]. Interestingly, the data analysis also showed that this ratio remained constant along the dendrite up to 100 μm (Fig. 3.8.C).

Based on the relation in Eq. 3.9, I obtained the value of the exocytosis rate. For this, I used the ratio of fluorescence intensity cytoplasm to the neuronal surface and multiplied it with the endocytosis rate reported in published literature by Rosendale et al., 2018 [135]. Finally, I arrived at the exocytosis rate as $\beta = 2.4 \times 10^{-4} s^{-1}$ for the endocytosis rate, $\alpha = 6 \times 10^{-4} s^{-1}$.

Next, I obtained the global trafficking parameters for the model, namely D_s, D_c, V_p. For this, I fitted the steady-state concentration of GluA2-containing AMPAR in the three population model to estimate global transport parameters to the normalized GluA2 fluorescence intensity Fig. 3.8.D. The best-fit values were $D_s = 0.7\,\mu\text{m}^2/\text{s}$, $D_c = 0.7\,\mu\text{m}^2/\text{s}$, and $V_p = 10^{-4}\,\mu\text{m/s}$.

Here, I obtained different values for the global trafficking parameters than in the previous section. However, it is important to note that these values were derived from a separate dataset of mouse hippocampal neurons, which may account for their variation from the experimental results shown in Fig. 3.5.B. Overall, by integrating experimentally measured AMPAR distribution data with an extended molecular dynamics model, I successfully characterized both local

and global trafficking parameters of endogenous AMPARs.

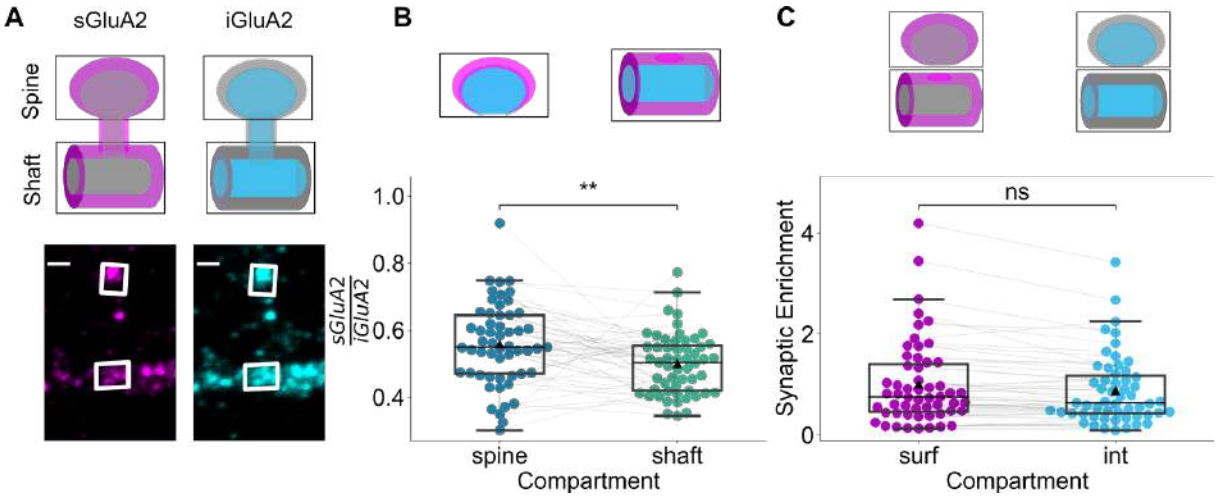

Figure 3.9.: **Synaptic enrichment of endogenous distribution of GluA2-containing AMPARs.** **A)** The schematic of the surface (top, left, magenta) and intracellular areas (top, right, cyan) of a synapse. Example images (bottom) show dendritic segments with spine and corresponding shaft ROIs (scale bar: 1 μm). **B)** The balance between the exocytosis and endocytosis rates in the spine (0.56 ± 0.12) and dendritic shaft (0.5 ± 0.09) ($N = 55$, $p = 0.0034$, z-stat=0.83). **C)** The surface (top, left) and intracellular (top, right) synaptic enrichment were computed as the corresponding spine area divided by the shaft area (magenta for the surface and cyan for the cytoplasm area, respectively $SE_{surf} = 1.01 \pm 0.84$, $SE_{int} = 0.88 \pm 0.68$) ($N = 55$, $p = 0.45$, z-stat = 0.55). Figure is adapted from [178].

Next, I wanted to understand if the ratio of exocytosis to endocytosis rate differed near the spines as compared to the dendritic shafts. For this, I performed a detailed analysis of the experimental data where I defined two regions of interest (ROIs): one encompassing the spine head region and the other corresponding to the adjacent dendritic shaft Fig. 3.9.A. I also utilized these ROIs to fit the rates of incorporation (η) into and exit (γ) from the PSD. Using these rectangular ROIS, I investigated whether the surface-to-intracellular (β/α) ratio of GluA2-containing AMPARs in spine heads and neighboring dendritic shafts differed from the average ratio along the dendrite (shown in Fig. 3.8.B). This analysis revealed a slightly but significantly higher β/α ratio in the spine head compared to the nearby dendritic shaft. Specifically, the mean exocytosis-to-endocytosis ratio was 0.5 in dendritic shafts adjacent to spine heads and 0.55 in the spine heads themselves (Fig. 3.9.B), exceeding the dendritic average of 0.4 (Fig. 3.8.B). AMPARs are exocytosed first and then get incorporated into the PSD via lateral diffusion. After reaching the PSD, AMPARs can interact with scaffolding proteins via intracellular signaling pathways, such as phosphorylation. These interactions stabilize them at the PSD by reducing their diffusion rate to a very low value (in the order of $10^{-3} - 10^{-2} \mu m^2/s$). To leave the PSD,

AMPARs must unbind from these scaffolding slots and diffuse away. This slightly higher ratio near spines compared to the rest of the dendrite can be due to the accumulation of surface near the spine neck, as the spine neck is shown to serve as a bottleneck for entry of surface receptors into the spines due to their thin morphology and presence of cytoarchitectural proteins such as septin7 barriers in the spine neck reduces the receptor diffusion across the neck ([56]). In the end, I used the value of 0.4 to obtain the exocytosis rate, as it was obtained over the entire dendrite and, hence, is a better representative value for the complete neuron.

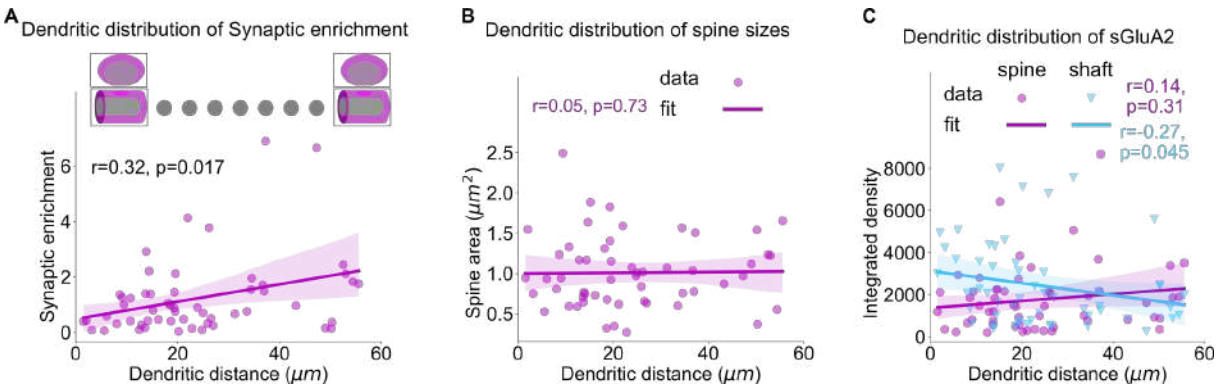

Figure 3.10.: **Synaptic enrichment increases with distance (A)** Scatter plot of Synaptic enrichment plotted against distance from the soma and regression line (magenta) and 95% Confidence interval (CI) shown as shaded region, spearman correlation coefficient = 0.32,p-value=0.017. **(B)** Scatter plot of spine areas plotted as a function of distance from the soma in $60\mu m$ distance. Regression line (magenta) and 95% CI shown as shaded region, spearman correlation coefficient= 0.05,p-value=0.73. Indicating no correlation between spine size and distance from soma. **(C)** Scatter plot of integrated fluorescence intensity (FI) from the spine (in magenta) and shaft (in cyan) plotted as a function of distance from the soma. Regression lines for the spine in magenta and 95% CI shown as a shaded region and shaft in cyan with 95 % CI shown as a shaded region, spearman correlation coefficients = 0.14,p-value=0.31 (for spines) and Spearman correlation coefficients = -0.27,p-value=0.045 (for shaft). FI in Shaft shows a decrease with distance from soma where as FI in spines remain constant. The figure is adapted from [178]

To determine the balance between the net synaptic incorporation (η) and exit (γ) rates of GluA2-containing AMPARs, I further analyzed the experimental data. I calculated a metric termed "synaptic enrichment, (SE)" defined as the ratio of integrated fluorescence density between spine heads and extrasynaptic ROIs for both surface and cytoplasmic receptors (see Fig. 3.9.C). On average, this ratio was approximately 1, and the fraction of extrasynaptic and synaptic surface receptors was close to 50% each. Using this information, I fitted the incorporation and exit parameters which came out to be $\eta = 7 \times 10^{-4} s^{-1}$ and $\gamma = 2.3 \times 10^{-2} s^{-1}$.

Interestingly, the synaptic enrichment also showed a positive correlation with dendritic distance. SE increased from proximal to distal dendrites, driven by a decrease in shaft fluorescence while synaptic fluorescence remained constant (Fig. 3.10.A-C).

To validate our 2D ROI-based approach, we cross-verified synaptic enrichment using a 1D method [61], which evaluates fluorescence intensity along a straight line ROI passing through the spine head (likely the PSD region) and adjacent dendritic shaft. The results were consistent, confirming the robustness of my results. I have described the comparison of the two methods in Fig. 3.11.

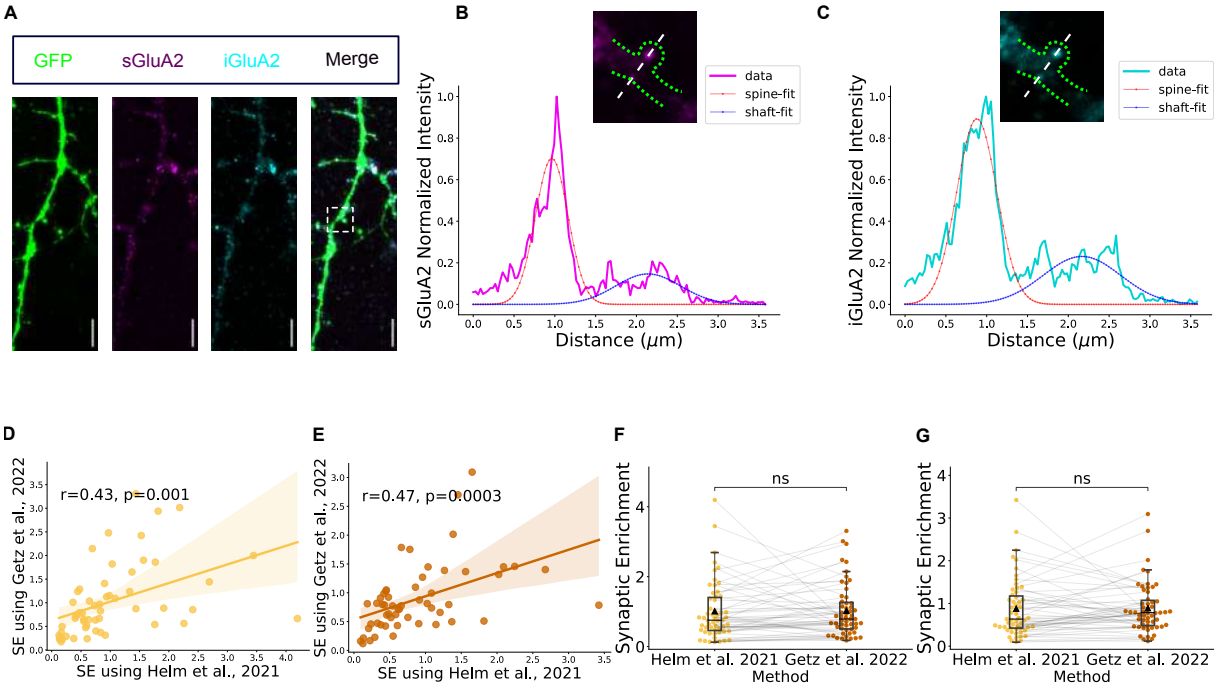

Figure 3.11.: **Calculation of Synaptic enrichment with two different methods yield comparable values** **(A)** A representative confocal image of hippocampal neuron cultures from mice transfected with GFP, anti-GluA2 labeled before and after permeabilization (sGluA2 and iGluA2 respectively obtained by my collaborators. Scale bar: $5\mu m$ **(B-C)** A representative line scan of sGluA2 across synaptic and dendritic ROIs (inset) used to calculate synaptic enrichment factor as described in [61]. The line starts from the spine head and is drawn along the neck and across the shaft. **(C)** Same as **B** but for iGluA2. I fitted two Gaussian kernels to the normalized intensity profile for calculating the synaptic enrichment factors. **(D-E)** A correlation plot of synaptic enrichment value calculated using the two methods described in [79] and [61], $n^{spines} = 55$ (from 8 neurons) for sGluA2 **(D)** and iGluA2 **(E)** (sGluA2: r= 0.43, p = 0.001, iGluA2: = 0.47, p = 3E-4). **(F-G)** Box plot with median and interquartile interval synaptic enrichment values gives comparable results using the two methods for both sGluA2 **(F)** and iGluA2 in **(G)**. mean is shown as black triangles. The figure is adapted from [178]

3.6. Brief summary

In this chapter, I describe the development of the baseline model of endogenous AMPAR trafficking. Obtaining equilibrium concentrations from the steady state is important to study the impact of plasticity induction. Using experimentally measured AMPAR distribution in biological neurons and an extended, three-population model, I successfully characterized the local and global trafficking parameters of endogenous AMPARs under basal conditions. Notably, I discovered that the endocytosis rate of AMPARs surpasses their exocytosis rate, with the exocytosis-to-endocytosis ratio remaining consistent along the dendrite. This dual regime"live longer, travel slower" in the plasma membrane near synapses and "live shorter, travel faster" in the cytoplasmappears to maintain a critical balance. This balance ensures the availability of GluA2-containing AMPARs at distal dendritic sites while supporting their stability near synapses. Subsequently, I applied the three-population model to explore how AMPAR copy numbers change during the regulation of local trafficking following plasticity induction.

4. AMPAR dynamics upon chemical LTP induction

This chapter is an adaptation of the results section and the supporting information of the article:
Surbhit Wagle, Maximilian K. Kracht, Anne Bührke, Amparo Acker-Plamer, Nataliya Kraynyukova, Anne-Sophie Hafner, Erin M. Schuman and Tatjana Tchumatchenko. "An integrative model of AMPA receptor trafficking reveals the central contribution of local translation in subtype-specific kinetics". bioRxiv, (2025). doi: https://doi.org/10.1101/2025.02.08.637220.

In this chapter, I discuss the time-dependent simulations of the three-population models described in Chapter 3. I performed these simulations to explain the plasticity-induced changes in synaptic AMPAR copy numbers for two subtypes of AMPARs, namely the GluA1-homomeric AMPARs and GluA2-containing AMPARs.

4.1. Differential kinetics of AMPAR subtypes to LTP induction

AMPAR underlies synaptic efficiency and plasticity. Hence, understanding their temporal dynamics is essential to unravel the time scales and mechanisms that lead to synaptic plasticity. One of the significant challenges in this domain is the complex interplay between the onset and duration of LTP-related processes and the specific subunit composition of the AMPARs involved. While much of the early research focused predominantly on GluA2-containing AMPARs, as they are the most abundant AMPAR subtype [182], recent studies have shed light on the pivotal role played by GluA2-lacking AMPARs in the induction and expression of LTP. The GluA2 subunit impacts the functional property of AMPARs with a significant divergence in AMPAR's permeability to Calcium ions (Ca^{2+}). AMPARs that lack a GluA2 subunit are permeable to Ca^{2+} while having a GluA2 subunit makes them impermeable to Ca^{2+}. Another functional consequence is that having GluA2 leads to a linear current-voltage (I-V) relationship. On the

other hand, GluA2-lacking AMPARs exhibit inward rectification as intracellular polyamines block them in a voltage-dependent manner. They also show high conductance and fast decay kinetics.

Generally, GluA2-lacking AMPARs are also called Calcium permeable- (CP) AMPARs [21]. While growing evidence has established that CP-AMPARs do not participate in synaptic transmission under basal conditions, their role in LTP is unclear due to conflicting findings. It is particularly noteworthy that the GluA1 homotetramer is the most abundant pore-forming complex among CP-AMPARs [42]. Several studies have shown that GluA1 homomers can be inserted at the synapse in a small time window (up to 30 minutes after LTP induction). Their insertion and the resulting Ca^{2+} was necessary for the full expression of LTP [126, 131] as applying inhibitors to block these CP-AMPARs within 30 minutes led to LTP reversal [126, 125, 131]. Previous studies have also reported a significant pool of CP-AMPARs present at the perisynaptic sites that can be rapidly and transiently incorporated into synapses undergoing LTP [131, 67, 76, 184, 126, 127]. The synaptic incorporation of GluA1 in basal condition and during LTP is shown to depend on the interaction of long-tailed C-terminal domain with the PSD proteins. This interaction is necessary and sufficient for hippocampal LTP [187].

These CP-AMPARs accumulate in the plasma membrane more quickly than their GluA2-containing counterparts [162]. However, immediately after the cessation of stimulation, the concentration of CP-AMPARs begins to decrease [162]. Recent research emphasizes that the synaptic incorporation of these receptors is essential for fully expressing LTP. In contrast, during chemically induced LTP (cLTP), GluA2 recruitment seems to be constitutive [148]. In recent work, Clavet-Fournier and colleagues performed protein antibody labeling of endogenous GluA2-containing AMPARs at different time points following chemical LTP induction. They observed that the synaptic fraction increased up to 2 hrs. These results show that chemical LTP induction leads to persistent, long-lasting changes in synaptic GluA2 content [31]. Given the preciseness and direct measure of synaptic AMPARs in these two studies, I decided to compare my model prediction to their results.

To better understand and compare the temporal responses of GluA2-containing AMPARs and GluA1 homomers, I decided to employ the three-population model described earlier (in section 3.5) to predict AMPAR concentrations in surface and synapse and compare its with experimental studies. To isolate these receptor types' distinct behaviors and quantitative measures, I utilized the data from Tanaka and Hiranos experiments [162]. In their study, they utilized

GluA1-SEP overexpression to visualize surface GluA1. Overexpression of specific AMPAR subunits significantly alters the receptor stoichiometry within transfected neurons, promoting homomeric AMPAR formation [42]. They induced LTP in cultured hippocampal neurons using a 10-minute bath application of Glycine, which is known to induce N-methyl-D-aspartate receptor (NMDAR) - dependent LTP. After LTP, the authors measured the change in synaptic GluA1 fluorescent intensity at 10, 20, and 30 minutes. The exocytosis rate was also measured once per minute during the entire 30 minutes.

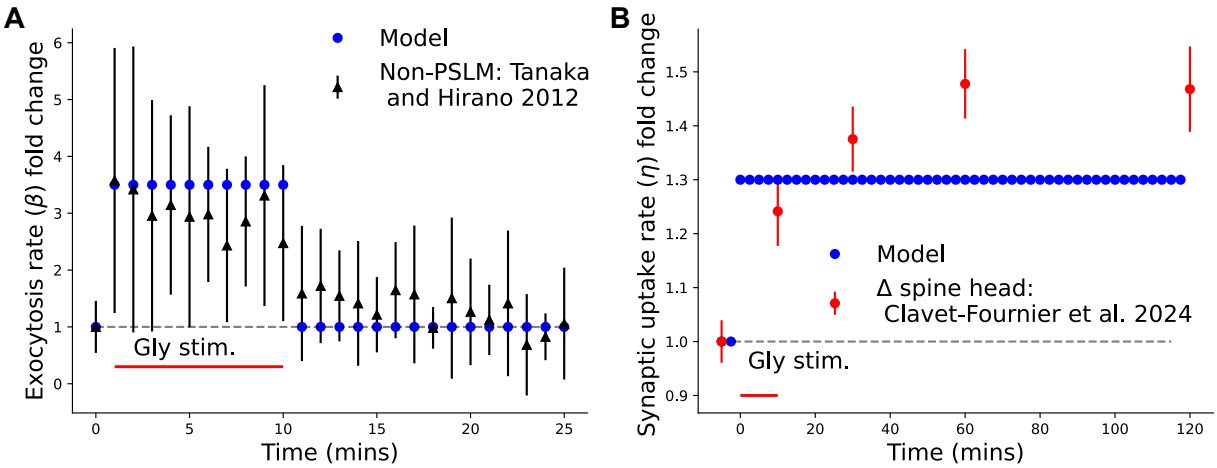

Figure 4.1.: **Changes for GluA1-homomeric AMPAR cLTP A)** I used a step function where the exocytosis rate (β) was increased 3.5 fold to the basal rate. The changes made in the model matched well with the change in exocytosis frequency reported in ([162] FigS3C). **B)** An additional change in the synaptic incorporation rate (η) was necessary, which reflects the average change in spine head size measured in ([31] Fig2F). The figure is adapted from [178].

In my simulations, I set out to replicate the changes in synaptic GluA1 content using the GluA1 version of three-population models that incorporated a matching Chemical long-term potentiation (cLTP) protocol (see section A.12 for details on GluA1-homomeric AMPAR model). For this, I assumed my model would be at equilibrium at the start of the simulation. Next, I simulated a 3.5-fold transient increase in the GluA1 exocytosis rate (β) during the 10-minute induction period that matched the experimental observation in [162] (see also Fig. 4.1.A). While this approach resulted in elevated GluA1 concentrations in the plasma membrane (ρ_s) and PSDs (ρ_{psd}), the model predicted a transiently higher concentration in dendritic regions compared to PSDs, which contradicted experimental findings Fig. 4.2.C.

To address this discrepancy, I refined the model by increasing both the exocytosis rate (β) and the incorporation rate (η) of GluA1 receptors upon cLTP induction. The increased incorporation rate reflects the enhanced trapping to AMPAR under plasticity condition due to the phoshory-

lation of GluA1 subunit and change in spine head area [68, 80, 40], which enhances synaptic incorporation rates (η). Specifically, I implemented a 1.3-fold increase in the incorporation rate alongside the 3.5-fold transient exocytosis rate enhancement. This increase in incorporation rate lasted for the entire duration of simulation time. These adjustments enabled the model to replicate the experimentally observed magnitude and temporal profile of GluA1 homomer dynamics well Fig. 4.2.C. Interestingly, changing the synaptic incorporation alone was insufficient to match experimental observations Fig. 4.2.B.

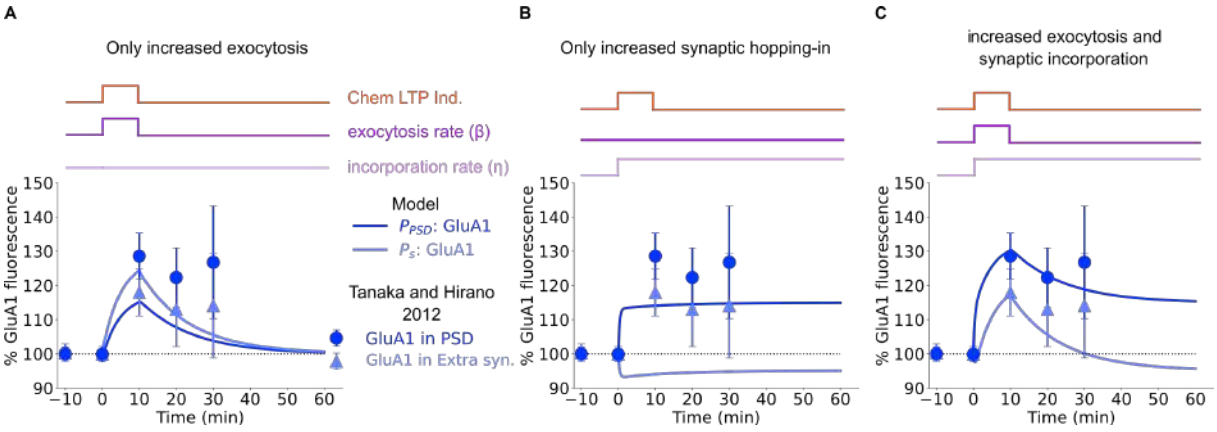

Figure 4.2.: **The three-population model can replicate the fast and transient synaptic GluA1 AMPAR dynamics A)** Change in GluA1 fluorescent intensity (as % of baseline intensity) upon increase in exocytosis rate. A fast increase in exocytosis rate (β) alone can not match the experimental data **B)** Same as **A** but for persistent increase in synaptic incorporation rate (η). This persistant increase also could not the experimental data. **C)** Same as **A** for a combination of exocytosis and synaptic incorporation. Both of these changes are necessary to match experimental data. The experimental data is reported in [162]. The figure is adapted from [178].

An exciting prediction emerged from the refined model: approximately 30 minutes after cLTP induction, the extrasynaptic concentration of GluA1 in the plasma membrane returned to baseline and subsequently fell below baseline levels after $\sim$ 1 hour Fig. 4.2.C. Meanwhile, synaptic GluA1 levels stabilized at an equilibrium concentration approximately 15% above baseline. This behavior highlights the intricate regulation of AMPAR dynamics during synaptic plasticity and underscores the critical interplay between receptor exocytosis and synaptic incorporation rates in shaping the temporal behavior of AMPARs.

These findings are interesting as they highlight the quick response of GluA1-AMPAR to plasticity induction. However, the decay in synaptic and extrasynaptic concentrations of these AMPAR subtypes after the end stimulation doesn't match with the observations of LTP induction, leading to long-lasting changes in synaptic efficacy and AMPAR content. To reconcile

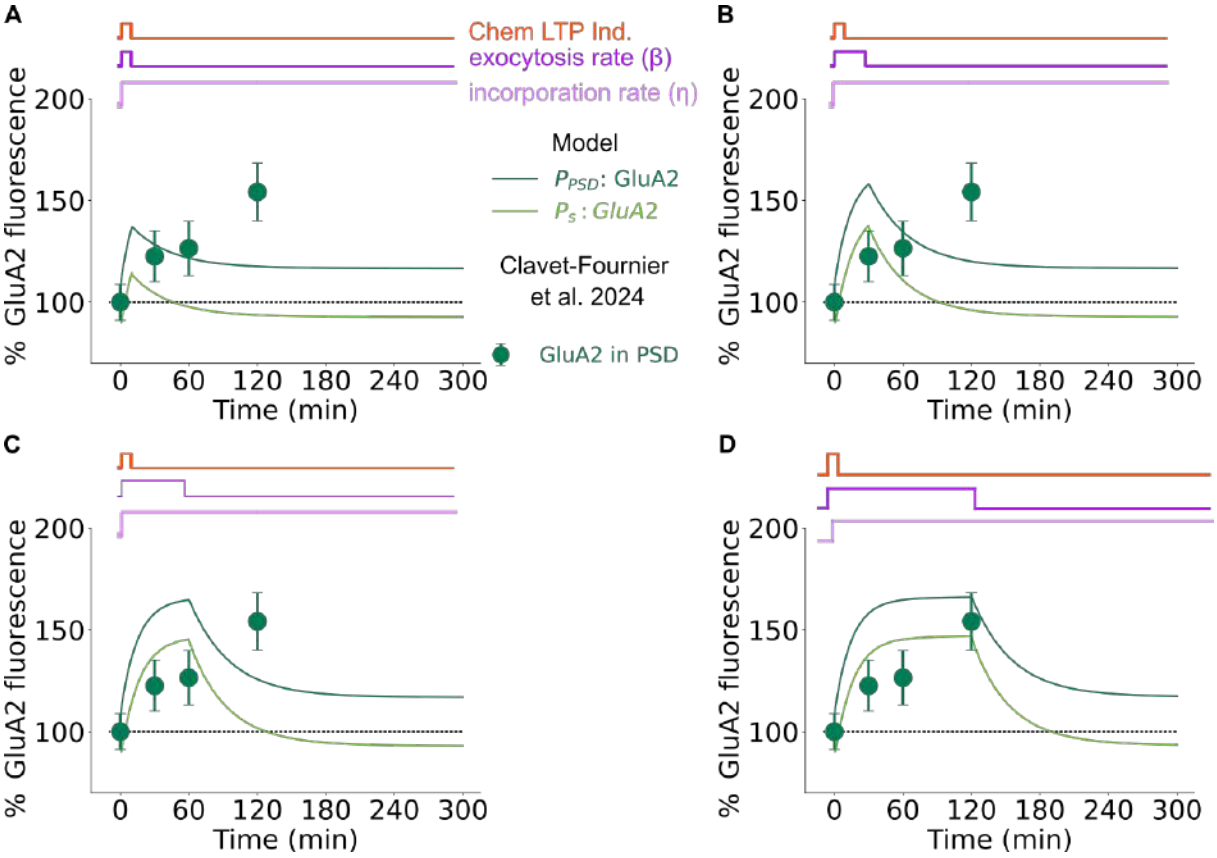

Figure 4.3.: **Constant exocytosis increase doesn't explain the response of GluA2-containing AMPARs A-D)** Temporal changes in GluA2 fluorescent intensity (% of baseline value) for fast increase in exocytosis rate (β) and a persistant change in synaptic incorporation rate (η). The exocytosis was increased for 10 minutes (in **A**), 30 minutes (in **B**), 60 minutes (in **C**), and 120 minutes (in **D**). The figure is adapted from [178].

these findings, I focused on GluA2-AMPAR content in synapses and their temporal evolution reported in experimental findings. To this end, I re-analyzed the data from a recently published study where Clavet-Fournier and colleagues utilized antibodies targeting endogenous GluA2 and super-resolution microscopy to track GluA2 concentration in postsynaptic densities (PSDs) following cLTP induction [31]. My analysis revealed a sustained increase in synaptic GluA2-containing receptors, persisting beyond the stimulation period and reaching approximately a 150% increase two hours after cLTP induction.

To replicate these findings, I integrated the experimental data for GluA2-containing receptors into my model [31] Fig. 4.3. Similar to the observations with GluA1, increasing the exocytosis and PSD incorporation rates elevated receptor concentrations in PSDs during stimulation but failed to sustain these elevated levels beyond the stimulation period. Moreover, the model could not reproduce either the kinetics or the amplitude of concentration increase of GluA2-containing

receptors Fig. 4.3. When I increased exocytosis rates for 10 minutes Fig. 4.3.A, 30 minutes Fig. 4.3.B, 1 hour Fig. 4.3.C and 2 hours Fig. 4.3.D, the model still could not reproduce the experimental observation in [31]. I have summarized the parameter changes and whether they matched experimental data on AMPAR changes following chemical LTP induction in Fig. 4.4. These results indicate that additional mechanisms, beyond direct changes in exocytosis and PSD incorporation, are likely involved in mediating synaptic trafficking of GluA2-AMPARs. In addition, they also highlight that the increase in exocytosis rate is both limited or slow and persists for several hours even after the stimulation ceases. Interestingly, such delayed and prolonged responses are often associated with the recruitment of local protein synthesis following stimulation. However, I have already shown that GluA2 mRNA is not abundantly present in dendrites (see Fig. 3.3]). Hence, I decided to shift my focus toward other key components of the AMPAR macromolecular complexes, particularly auxiliary subunits, as they are known to alter functional and trafficking characteristics of AMPARs [12, 168, 143].

	GluA1-homomeric AMPAR			GluA2-containing AMPAR		
Parameter change / Response	exocytosis rate (β) only	incorporation rate (η) only	both β and η	exocytosis rate (β) only	incorporation rate (η) only	both β and η
Kinetics	✓	✗	✓	✗	✗	✗
Amplitude	✗	✗	✓	✗	✗	✗

Figure 4.4.: **Summary of chemical LTP simulations for GluA1-homomeric and GluA2-containing AMPARs**. The figure is adapted from [178].

4.2. Auxiliary subunit CNIH-2 is locally translated

To gain insights, I leveraged a large translatome dataset published by Glock and colleagues [63]. The authors used ribosomal profiling to dissect local transcriptomes in neurons, estimating the translation rates of neuronal transcripts in the cell body, dendrites, and axons. Their data also confirmed the somata-enriched localization of AMPAR pore-forming subunit GluA1-2 mRNAs.

CNIH-2, encoded by the gene *Cnih2*, stood out due to its unique transcript distribution among all the AMPAR's auxiliary subunits previously identified. The ribosome profiling data showed comparable read levels for *Cnih2* mRNA in dendrites and somatic regions, a distribution profile remarkably similar to that of *CamK2a* mRNA. Experimental studies show that CNIH-2 signifi-

cantly slows down receptor deactivationby as much as five-fold thereby extending the duration of excitatory postsynaptic currents, irrespective of the GluA subunit composition [34, 149, 143]. This modulation enhances the net depolarizing ion influx into the postsynaptic neuron, increasing synaptic efficacy.

Despite these findings, the precise role of CNIH-2 remains debated. Initially, it was thought to facilitate AMPAR transport between the endoplasmic reticulum (ER) and the Golgi apparatus (GA) in hippocampal CA1 neurons [75, 20]. However, subsequent studies suggest that CNIH-2 can bypass this early anterograde pathway and directly deliver AMPARs to the plasma membrane [74]. Moreover, there are conflicting results on the association of CNIH-2 with AMPARs subtypes, with evidence for a higher preference for GluA1/2 heteromers over GluA2/3 receptors and GluA2-lacking or GluA2-containing AMPARs [34, 15, 12]. To address these uncertainties and understand the role of CNIH-2 in AMPAR trafficking, I decided to study its mRNA and protein localization and function in more detail.

► Cnih2 mRNA density

I began by investigating the localization of *Cnih2* mRNAs in the rat hippocmapal neuronal cultures. My Collaborator, Dr. Anne-Sophie Hafner, performed FISH against *Cnih2* mRNA and compared it with *CamK2a* mRNA and acquired neuronal images using confocal microscopy. In Fig. 4.5.A, I show an example FISH image. Next, I analysed this data to understand *Cnih2* mRNA localization. Strikingly, the distribution of *Cnih2* mRNA closely mirrored that of *CamK2a*. Excitingly, my analysis revealed that $\sim 50\%$ of *Cnih2* mRNA was localized within dendrites, a level comparable to the 60% observed for *CamK2a* Fig. 4.5.B. This fraction was approximately three folds higher than *Gria2* mRNA (18%) and two folds higher than the *Gria1* mRNA (26%).

To get a more precise idea about the distribution of dendritic mRNA, I fitted the spatial profiles of both *Cnih2* and *CamK2a* mRNAs with decaying exponential functions (see Appendix section A.12 for details on the fitting procedure). At a dendritic distance of 100 μm, the distributions of *Cnih2* and *CamK2a* mRNAs showed similar profiles. The mRNA density reduced by 59% and 52% for, *Cnih2* and *CamK2a* mRNAs respectively Fig. 4.5.C. Next, I studied how *Cnih2* mRNA dictates the protein density and local synthesis of de novo CNIH-2 protein in dendrites.

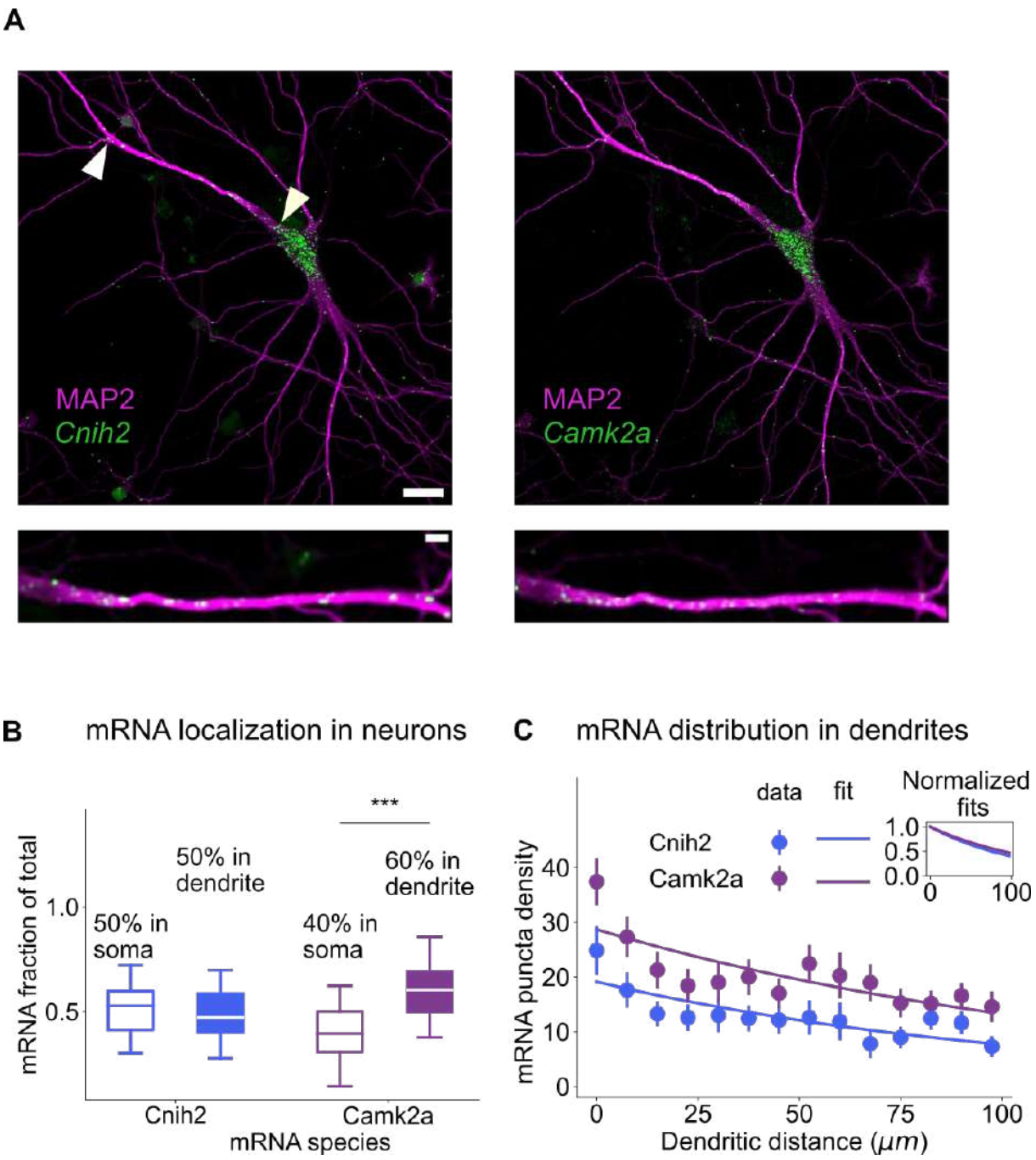

Figure 4.5.: ***Cnih2* mRNA is abundant in dendrites A)** *Top:* Cultured rat hippocampal neurons (1821 DIV) labeled with FISH for *Cnih2* (left, green) and *CamK2a* mRNA (right, green) alongside fluorescent MAP2 immunostaining (magenta). Scale bar = 20 μm. *Bottom:* A magnified dendrite shows fewer *Cnih2* mRNA signals (left) compared to *CamK2a* mRNA (right). Scale bar = 5 μm. **B)** Somatic (hollow) and dendritic (filled) fractions of total mRNA for *Cnih2* (27 cells, p = 1.0) and *CamK2a* (19 cells, p = 6e-4). Comparison between *Cnih2* and *CamK2a* in dendrites: p = 0.08. **C)** Fitting an exponential function to mRNA puncta density distribution yields an exponent of -0.009 ± 0.002 for *Cnih2* (n = 36 dendrites) compared to-0.007 ± 0.002 for *CamK2a* (n = 38 dendrites). *Inset:* Normalized fits shown for *Cnih2* and *CamK2a* mRNA distribution. The figure is adapted from [178].

► CNIH-2 protein density

Next, I studied the localization of CNIH-2 receptors along the dendrites. For this, my collaborator, Dr. Anne-Sophie Hafner performed immunolabeling of CNIH-2 using protein antibody in rat hippocampal cultural neurons at DIV 18-21 Fig. 4.6.A. I have provided the details of this experiment in Appendix section A.14. Dr. Hafner acquired images of the processed neuron using confocal microscope and I analyzed the dataset. My analysis revealed a homogeneous distribution of receptors along the dendrites Fig. 4.6.B.

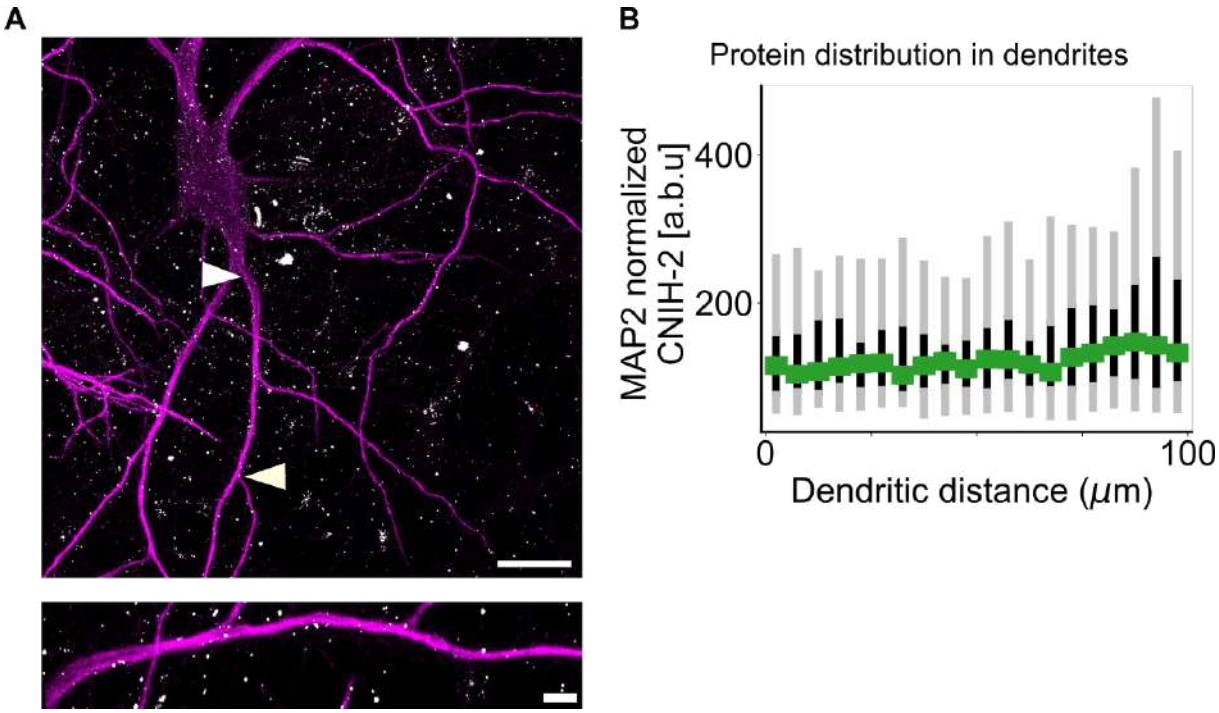

Figure 4.6.: **CNIH-2 protein exhibit a constant density in the dendrites**. **A)** *Top:* Cultured rat hippocampal neurons at DIV 1821 were processed for antibody labeling of CNIH-2 protein (gray) and FI MAP2 (magenta). *Bottom:* A magnified view of a representative dendrite reveals a uniform GluA2 distribution along the first 100 μm. Scale bar = 20 μm. **B)** MAP2-normalized CNIH-2 intensity (5 μm bins; median shown as green squares with interquartile range [IQR]). The figure is adapted from [178].

► CNIH-2 local synthesis

Given this significant dendritic localization of *Cnih2* mRNA and protein, I examined whether CNIH-2 protein is synthesized locally within dendrites. For this, my collaborators Dr. Anne-Sophie Hafner and Prof. Erin Schuman performed FUNCAT combined with PLA. Briefly, this technique involves the incorporation of a non-canonical amino acidAHA, a methionine derivativeduring protein synthesis, followed by antibody-based detection of a specific protein

of interest, with coincidence signals detected via PLA. Neurons were incubated with AHA or methionine (as a control) for one hour, fixed, and analyzed. I have provided the details of this experiment in Appendix section A.14.

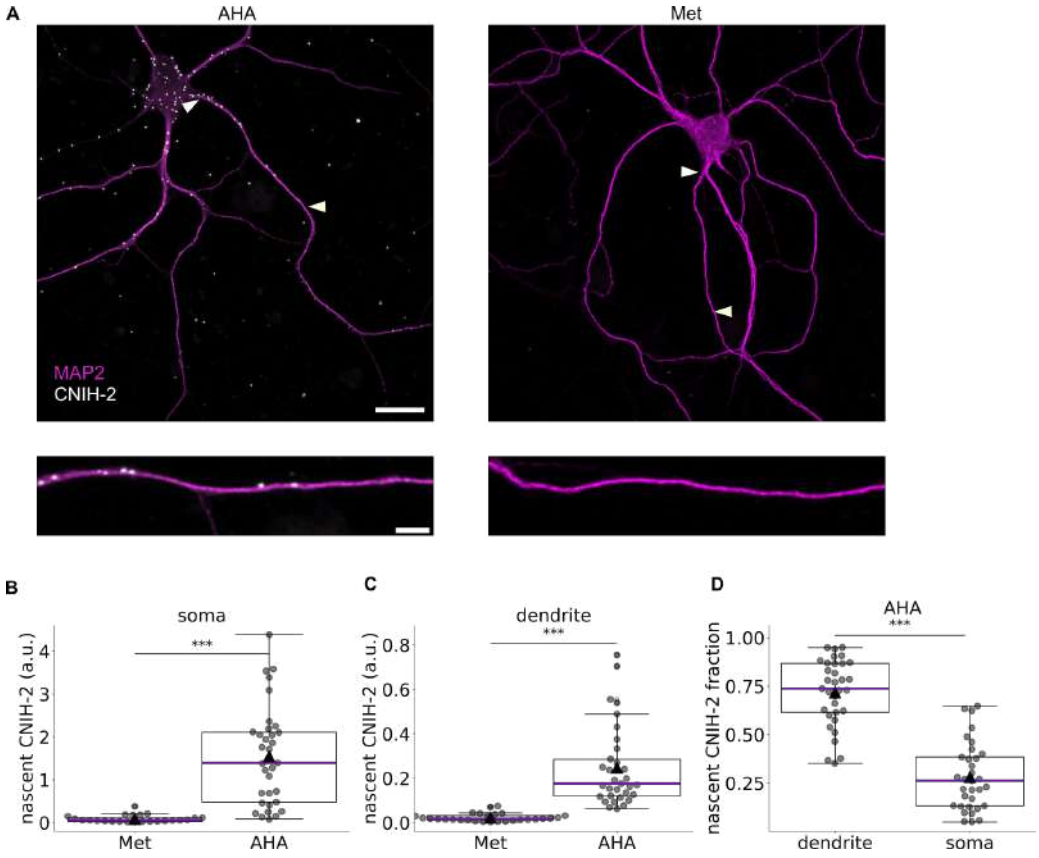

Figure 4.7.: **CNIH-2 protein is locally translated**. **A)** *Top:* Example images of cultured hippocampal neurons processed using FUNCAT-PLA showing the distribution of newly synthesized AMPAR auxiliary subunit CNIH-2 after 1 hour of metabolic labeling with AHA or, in control conditions, with methionine (Met). Scale bar $= 20\mu m$. *Bottom:* Representative dendrite illustrates abundant CNIH-2 nascent protein after 1 hour of metabolic labeling with AHA. cale bar $= 10\mu m$. **B)** Boxplot showing CNIH-2 nascent protein density in the soma ($n_{met} = 33$, $n_{AHA} = 29$ neurons per condition). **C)** same as B) but for dendrites. **D)** Boxplot showing fraction of protein in dendrites and the somatic compartment for neurons treated with AHA. $***, p \leq 0.001$. Circles represent individual neuron values, box lines indicate the median, and black triangles represent the mean. The figure is adapted from [178].

Next, I analyzed the CNIH-2 FUNCAT-PLA dataset and quantified local synthesis puncta using the SpyDen tool. Quantification of nascent CNIH-2 proteins (in AHA condition) during this period revealed prevalent synthesis in somata and across the dendritic arbor Fig. 4.7.A. Notably, approximately 75% of the newly synthesized CNIH-2 protein localized to dendrites Fig. 4.7.D. Under the control conditions (methionine), FUNCAT-PLA signals were virtually absent in both somata and dendrites, confirming the specificity of the synthesis signal Fig. 4.7.B-

C.

The findings from FUNCAT-PLA data, combined with the high abundance of *Cnih2* mRNA in dendrites, strongly suggest that CNIH-2 is locally synthesized throughout the dendritic arbor. This raises an important question: what could be the functional implications of CNIH-2 synthesis at such distal sites?

4.3. CNIH-2 dynamics upon cLTP induction

Given its role in slowing down AMPAR deactivation and prolonging excitatory postsynaptic currents, local synthesis of CNIH-2 could serve as a mechanism to enhance synaptic strength selectively and dynamically at specific dendritic sites. This spatially targeted modulation could be particularly critical for synaptic plasticity, where the precise timing and location of receptor regulation play a pivotal role in shaping neural circuits and information processing.

To further unravel the intricate molecular machinery underpinning learning, memory, and neuronal adaptation, I continued investigating the interplay between AMPAR auxiliary subunits and synaptic function. Harmel and colleagues previously reported that CNIH-2 preferentially associates with AMPARs possessing unprocessed glycans [75]. At the time, these findings were interpreted to suggest that CNIH-2 primarily interacts with receptors within the endoplasmic reticulum (ER). However, more recent studies challenge this interpretation. First, evidence has shown that CNIH-2 is present at the PSD, where it significantly impacts synaptic currents [15]. Second, unprocessed glycan-bearing AMPARs have been shown to traffic to the plasma membrane in neurons [74].

Based on these findings, I hypothesized that CNIH-2 might play a pivotal role in the activity-dependent trafficking of AMPARs to the neuronal plasma membrane. To test this hypothesis, my collaborators, Dr. Anne-Sophie Hafner and Prof. Erin Schuman, designed plasticity experiments where they applied a chemically induced cLTP protocol to cultured hippocampal neurons from rats and tracked changes in newly synthesized CNIH-2 protein concentrations using FUNCAT-PLA. In Fig. 4.8.A, I show an example image from this dataset under basal and chemical LTP condition. I have provided the details of this experiment in Appendix section A.14. Interestingly, I observed no significant change in CNIH-2 synthesis in somata Fig. 4.8.B. On the contrary, cLTP induction remarkably resulted in a significant twofold increase in the concentration of dendritic CNIH-2 protein within an hour of stimulation Fig. 4.8.C. This experiment

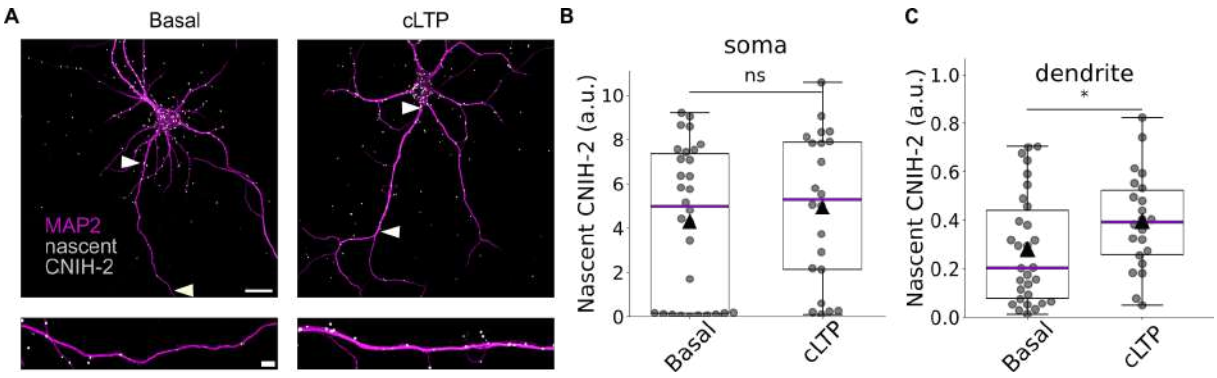

Figure 4.8.: **De novo CNIH-2 synthesis in dendrites increases upon chemical LTP induction**. **A)** *Top row:* Representative images of rat cultured hippocampal neurons displaying the distribution of newly synthesized CNIH-2 after 1 hour of metabolic labeling with AHA (*left*) and increased levels of de novo CNIH-2 proteins in dendrites following cLTP induction (*right*). Scale bar: $20\mu m$. *Bottom row:* Zoomed in images of dendrites from the representative images, scale bar: $5\mu m$. **B)** Box plots displaying the density of newly synthesized CNIH-2 in the soma. **C)** Same as **B** but in dendrites (n = 30 for basal, n = 22 for cLTP neurons analyzed). A significant increase was seen in dendrites but not in the soma * $p \leq 0.05$. Circles represent individual neuron values, and box lines for the median and IQR. The mean is shown as black triangles. The figure is adapted from [178].

provides direct evidence of activity-dependent regulation of an AMPAR auxiliary subunit for the first time, demonstrating a robust, localized increase in CNIH-2 synthesis in dendrites following LTP. What could be the function of CNIH-2 local synthesis and its regulation upon chemical LTP induction? To answer this, my collaborators further recorded the data where CNIH-2 was removed from the neurons, and surface GluA subunits were immunolabelled and imaged.

4.4. CNIH-2 drives forward trafficking of AMPARs to neuronal surface

To further explore how CNIH-2 synthesis in dendrites regulates AMPAR trafficking to the neuronal surface, my collaborators Dr. Anne-Sophie Hafner, Dr. Anne Bührke and Prof. Erin Schuman developed a platform to label nascent GluA1- and GluA2-containing receptors localized on the plasma membrane. First, they treated cultured hippocampal neurons with AHA (4 mM, 1 hour) and during the final 715 minutes, they incubated neurons with antibodies targeting the extracellular N-terminal domains of GluA1 or GluA2 subunits for surface labeling.

To investigate the functional role of CNIH-2 in promoting AMPAR surface expression, they employed a shRNA strategy to reduce *Cnih2* transcript levels. Hippocampal cultured neurons

from rats were transfected with CNIH-2 shRNA or control shRNA at 8 days in vitro (DIV). After 11 days of shRNA expression, they treated the neurons with AHA or methionine (as a control) and subsequently surface-labeled GluA1 or GluA2 using antibodies prior to fixation Fig. 4.10.A.

They also valludated the efficieny of CNIH-2 knockdown after 11 days. For this they performed FISH against *Cnih2* mRNA and FUNCAT-PLA detection of nascent CNIH-2 protein, the efficiency of was validated. My analysis of their FISH dataset showed that *Cnih2* mRNA transcript levels were reduced to 0 in the shRNA against *Cnih2* conditions as compared to shRNA control Fig. 4.9.A. Next, I analyzed the FUNCAT-PLA dataset of nascent CNIH-2 protein and observed significantly smaller protein levels in the shRNA-*Cnih2* condition compared to the control shRNA condition Fig. 4.9.B. This analysis validated the knockdown of CNIH-2 protein from the system.

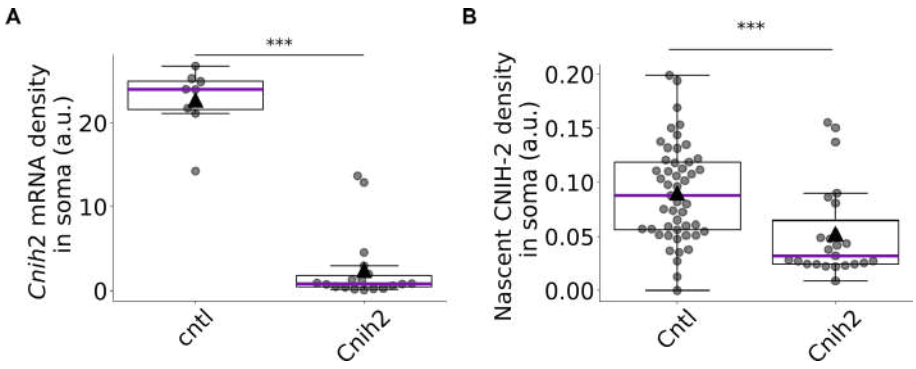

Figure 4.9.: **Validation of CNIH-2 knockdown using an shRNA strategy**. **A)** Bar graphs and strip plots illustrate the density of Cnih2 mRNA in the soma of neurons expressing either a control shRNA or an shRNA targeting Cnih2 ($n_{Control} = 8, n_{CNIH2} = 18$ neurons per condition). *** $p \leq 0.001$. **B)** Bar graphs and strip plots depict the density of nascent CNIH-2 proteins in the soma of neurons expressing either a control shRNA or an shRNA targeting Cnih2 ($n_{Cntl} = 49, n_{CNIH2} = 23$ neurons analyzed per condition). ***$p \leq 0.001$. Circles represent individual neuron values, and box lines for the median and IQR. The mean is shown as black triangles. The figure is adapted from [178].

Next, I analyzed the levels of GluA subunits at the neuronal surface in the two conditions. Reduced CNIH-2 expression had no measurable effect on the surface expression of GluA1 subunits Fig. 4.10.B&C. However, it dramatically reduced the surface expression of GluA2 subunits, both in the soma and dendritic arbor Fig. 4.10.B&D.

These findings highlights the critical role of CNIH-2 in driving the surface expression of GluA2-containing AMPARs. The data also reveal a specific requirement for CNIH-2 in facilitating the trafficking of GluA2 subunits to the plasma membrane, emphasizing its essential role

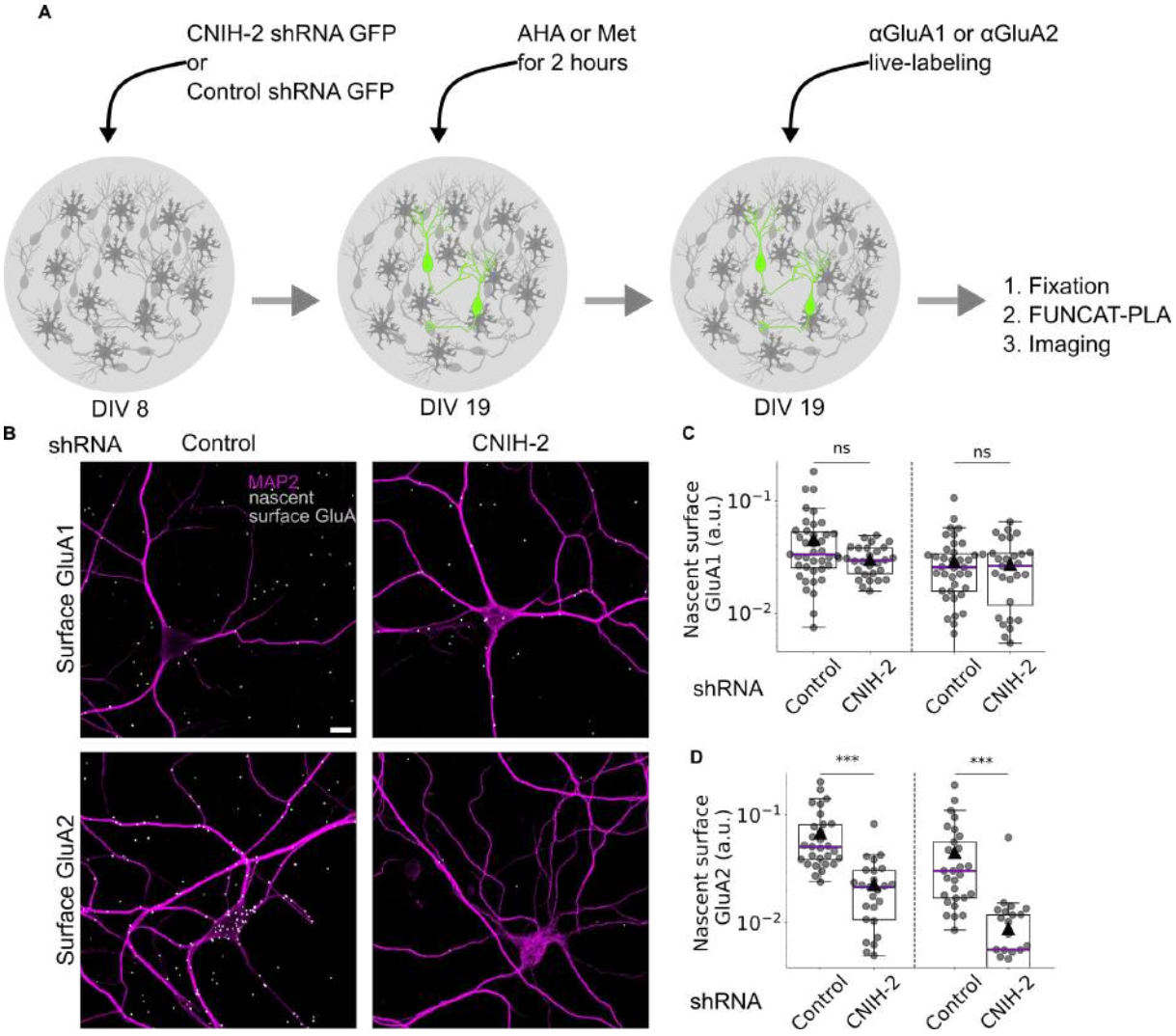

Figure 4.10.: **CNIH-2 drives surface insertion of GluA2-containing AMPARS**. **A)** Scheme showing experimental flow for the analysis of GluA1 and GluA2 trafficking to the surface in presence (Control-shRNA-GFP) or absence (CNIH-2-shRNA-GFP) of CNIH-2. **B)** Cultured hippocampal neurons displaying newly synthesized surface GluA1 and GluA2 subunits in neurons expressing either a shRNA targeting CNIH-2 or a control shRNA with no rat genome ta gets. In the absence of CNIH-2 proteins, newly synthesized GluA2-containing AMPARs are absent from both the somatic and dendritic surfaces. Scale bar$= 20\mu m$. **C)** Box plots display no significant change in the abundance of newly synthesized GluA1 receptors at the cell surface in the soma and dendrite (Control $n = 39$, without CNIH-2 $n = 28$ neurons per condition). **D)** Box plots display a significant reduction in the abundance of newly synthesized GluA2 receptors at the cell surface in the soma and dendrite(Control $n = 29$, without CNIH-2 $n = 25$ neurons per condition). (* $p \leq 0.05$, *** $p \leq 0.001$) . Circles represent individual neuron values, and box lines for the median and IQR. The mean is shown as black triangles. The figure is adapted from [178].

in regulating AMPAR composition and synaptic plasticity.

Next, I build a trafficking model of CNIH-2 by expanding a previously developed model by Fonkeu and colleagues [58] to model CNIH-2 concentration along my model dendrite at

equilibrium and changes in its concentration upon plasticity induction.

4.5. Model of CNIH-2 mRNA and protein density

My findings so far warranted detailed modeling of CNIH-2 mRNA and protein as it drives the insertion of GluA2-containing AMPARs to the neuronal membrane.

► mRNA density

To model CNIH-2 mRNA density, I utilized the model published in [58]. The mRNA dynamics is governed by the PDE:

$$\frac{\partial R_{CNIH-2}(x,t)}{\partial t} = D_R \frac{\partial^2 R_{CNIH-2}(x,t)}{\partial x^2} - v_R \frac{\partial R_{CNIH-2}(x,t)}{\partial x} - k_R R_{CNIH-2}(x,t). \quad (4.1)$$

I am interested in getting the equilibrium concentration of *Cnih2* mRNA (i.e. assuming that the mRNA concentration doesn't change with time, $\frac{\partial R_{CNIH-2}(x,t)}{\partial t} = 0$). At equilibrium, this PDE is reduced to an ODE:

$$0 = D_R \frac{d^2 R_{CNIH-2}(x)}{dx^2} - v_R \frac{dR_{CNIH-2}(x)}{dx} - k_R R_{CNIH-2}(x). \quad (4.2)$$

This ODE can be fully solved with the help of two boundary conditions. Hence, I subject the ODE Eq. 4.2, first to a boundary condition assuming there is a constant influx ($\Phi(0)$) of new mRNAs from the soma (J_{Rin}). Second, I assume a no-flux boundary at the distal end of the dendrite ($\Phi(L)$), as no mRNA can escape out of the dendrite. These two boundary conditions are mathematically described as:

$$\begin{aligned} \Phi(0) &= -J_{Rin} \\ \Phi(L) &= 0. \end{aligned} \quad (4.3)$$

The steady state concentration of *Cnih2* mRNA (denoted by $R^{SS}_{Cnih2}(x)$) is then given by the solution of Eq. 4.2, as:

$$R^{SS}_{Cnih2}(x) = \frac{J_{Rin}}{e^{-\lambda_{R1}L} - e^{-\lambda_{R2}L}} \left(\frac{e^{-\lambda_{R2}L-\lambda_{R1}x}}{v_R + D_R\lambda_{R1}} - \frac{e^{-\lambda_{R1}L-\lambda_{R2}x}}{v_R + D_R\lambda_{R2}} \right). \tag{4.4}$$

Here $\lambda_{R1,2} = (-v_R \pm \sqrt{v_R^2 + 4D_R k_R})/(2D_R)$. I have described the steps to derive the solution written in Eq. 4.4 in Appendix section A.8. Additionally, the baseline parameters used for mRNA density distribution are provided in Table A.7.

▶ Protein density

Next, I describe the protein density of CNIH-2 in my model dendrite. The protein density distribution is governed by the diffusion, degradation, and local synthesis of CNIH-2 in the dendrites. These mechanisms are captured using the PDE:

$$\begin{aligned} \frac{\partial \rho_{CNIH-2}(x,t)}{\partial t} = D_P \frac{\partial^2 \rho_{CNIH-2}(x,t)}{\partial x^2} - v_P \frac{\partial \rho_{CNIH-2}(x,t)}{\partial x} - k_P \rho_{CNIH-2}(x,t) \\ + \beta_P R^{SS}_{Cnih2}(x). \end{aligned} \tag{4.5}$$

$\rho_{CNIH-2}(x,t)$, describes the dynamics of CNIH-2 protein along the dendrite in this equation. The first term on the right-hand side (RHS) describes the diffusion (with the rate D_P), the second term represents active transport (with the rate v_p), the third term represents the degradation of CNIH-2 protein (with the rate k_p), and the final term represents the local translation of *Cnih2* mRNA w th a rate of translation β_P. To get the CNIH-2 protein density at equilibrium (i.e. the density doesn't change with time), we can assume $\frac{\partial \rho_{CNIH-2}(x,t)}{\partial t} = 0$, and convert the PDE in Eq. 4.5, to an ODE:

$$0 = D_P \frac{d^2 \rho_{CNIH-2}(x)}{dx^2} - v_P \frac{d\rho_{CNIH-2}(x)}{dx} - k_P \rho_{CNIH-2}(x) + \beta_P R^{SS}_{Cnih2}(x). \tag{4.6}$$

Similar to the ODE describing mRNA density, the ODE for protein density can also be solved using two boundary conditions. Again, first, I assume a constant influx, $\Phi(0)$, of new proteins from the soma into my model dendrite. Second, I assume a no-flux boundary at the distal end of the dendrite, $\Phi(L)$, as no protein can escape out of the dendrite. These two boundary conditions are mathematically described as:

$$\begin{aligned}\Phi(0) &= -J_{Pin} \\ \Phi(L) &= 0.\end{aligned} \tag{4.7}$$

With these boundary condition, The full solution of the ODE in Eq. 4.6, describing CNIH-2 protein density distribution, is given as:

$$\begin{aligned}\rho^{SS}_{Cnih2}(x) = \\ &- \left(\frac{\frac{(v_P+D_P\lambda_{R1})\beta_P}{D_P\lambda^2_{R1}+v_P\lambda_{R1}-k_P}\left(e^{-\lambda_{P2}}L - e^{-\lambda_{R1}}L\right) + J_{Pin}e^{-\lambda_{P2}}L}{(v_P+D_P\lambda_{P1})(e^{-\lambda_{P1}}-e^{-\lambda_{P2}}L)} \right. \\ &\left. + \frac{\frac{(v_P+D_P\lambda_{R2})\beta_P}{D_P\lambda^2_{R2}+v_P\lambda_{R2}-k_P}\left(e^{-\lambda_{P2}}L - e^{-\lambda_{R2}}L\right)}{(v_P+D_P\lambda_{P1})(e^{-\lambda_{P1}}-e^{-\lambda_{P2}}L)} \right) e^{-\lambda_{P1}x} \\ &+ \left(\frac{\frac{(v_P+D_P\lambda_{R1})\beta_P}{D_P\lambda^2_{R1}+v_P\lambda_{R1}-k_P}\left(e^{-\lambda_{P1}}L - e^{-\lambda_{R1}}L\right) + J_{Pin}e^{-\lambda_{P1}}L}{(v_P+D_P\lambda_{P2})(e^{-\lambda_{P1}}-e^{-\lambda_{P2}}L)} \right. \\ &\left. + \frac{\frac{(v_P+D_P\lambda_{R2})\beta_P}{D_P\lambda^2_{R2}+v_P\lambda_{R2}-k_P}\left(e^{-\lambda_{P1}}L - e^{-\lambda_{R2}}L\right)}{(v_P+D_P\lambda_{P2})(e^{-\lambda_{P1}}-e^{-\lambda_{P2}}L)} \right) e^{-\lambda_{P2}x} \\ &- \frac{-\beta_P J_{Rin}e^{-\lambda_{R2}L}}{(D_P\lambda^2_{R1}+v_P\lambda_{R1}-k_P)(v_R+D_R\lambda_{R1})(e^{-\lambda_{R1}L}-e^{-\lambda_{R2}L})}e^{-\lambda_{R1}x} \\ &- \frac{-\beta_P J_{Rin}e^{-\lambda_{R1}L}}{(D_P\lambda^2_{R2}+v_P\lambda_{R2}-k_P)(v_R+D_R\lambda_{R2})(e^{-\lambda_{R2}L}-e^{-\lambda_{R1}L})}e^{-\lambda_{R2}x}\end{aligned} \tag{4.8}$$

whereby $\lambda_{P1/2} = (-v_P \pm \sqrt{v_P^2 + 4D_P k_P})/(2D_p)$. I have described the steps to arrive at the solution to the ODE defined in Eq. 4.6 in Appendix section A.9. Additionally, I have provided the the parameters I used to obtain a uniform CNIH-2 protein distributions are provided in Appendix Table A.7. Next, I used my model of CNIH-2 protein density to understand how it impacted GluA2-containing AMPAR dynamics upon plasticity induction.

4.6. CNIH-2 driven GluA2-AMPAR exocytosis

As I have previously shown, CNIH-2 is locally synthesized in the dendrite, and the rate of its de novo synthesis increases upon plasticity induction (see Fig. 4.8); I decided to use the model

of CNIH-2 for explaining AMPAR changes upon plasticity induction, specifically for GluA2-containing AMPARs as it selectively traffics them to the neuronal membrane Fig. 4.10.

For this, I solved the time-dependent PDE in Eq. 4.5 using numerical integration methods. I have described the step for the numerical integration in Appendix section A.10.

First, I simulated a brief increase in CNIH-2 local translation rate (by 500 folds) that lasted for 10 minutes to match the time used for chemical LTP induction. This brief translation upregulation lasting just 10 minutes resulted in a moderate two-fold increase in CNIH-2 concentration within the proximal dendritic region after two hours, which further declined to a 1.5-fold increase after five hours Fig. 4.11.A. Next, I incorporated the time-dependent changes in CNIH-2 density into my three-population model of AMPAR trafficking. I simulated an increase in the exocytosis rate of GluA2-containing AMPARs dependent on CNIH-2 density and a 1.3-fold increase in their synaptic incorporation rate into PSDs after cLTP induction. My model assumed that the exocytosis rate varied spatially and temporally in proportion to the modeled changes in CNIH-2 distribution. With these changes, my model could not fully capture the dynamics of GluA2-containing AMPARs reported by Clavet-Fournier and colleagues [31]. My model predicted a slow increase in GluA2 synaptic concentration that matched the early time point data (at 30 and 60 minutes). However, the peak amplitude predicted by my model saturated at $\approx 125\%$ of baseline Gl A2 synaptic concentration Fig. 4.11.B. This was less than the data that showed an $\approx 150\%$ increase at 120 minutes after chemical LTP induction.

These results indicated that local synthesis of CNIH-2 does provide the timescales required to match synaptic GluA2 changes. However, a local synthesis lasting only for the duration of LTP stimulation is not sufficient to explain the significant increase in synaptic GluA2 content.

To fix this, I next simulated a prolonged up-regulation of CNIH-2 local synthesis (again by 500 folds) that lasted for hours. The intuition behind this prolonged up-regulation is based on experimental studies that have reported heightened local synthesis following synaptic plasticity [28, 130]. My model of CNIH-2 protein density resulted in an $\approx$ twelve-fold increase in CNIH-2 density at the end of 2 hours (up-regulation duration). Additionally, the CNIH-2 protein remained well above five folds after 5 hours of simulation time Fig. 4.12.A. Next, again I used CNIH-2 density as a driver of exocytosis rate in my three-population model of GluA2-containing AMPARs. When combined with the small 1.3-fold increase in synaptic incorporation rate, my model could match both the kinetics as well as the peak amplitude of synaptic GluA2 reported experimentally in [31] Fig. 4.12.B.

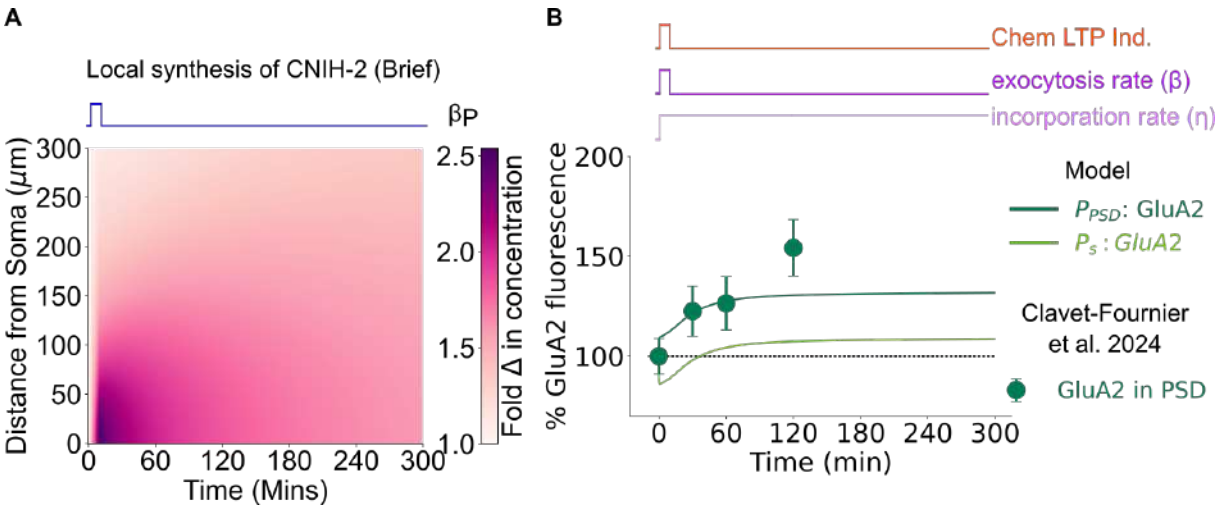

Figure 4.11.: **Brief, 10 minutes CNIH-2 local synthesis can not explain GluA2 dynamics upon chemical LTP induction**. **A)** Spatio temporal distribution CNIH-2 concentration upon increased local translation lasting for brief, 10 minutes follwoing LTP induction. **B)** Changes in synaptic and surface GluA2 when changes in CNIH-2 was used as an increase in exocytosis rate. In addition a 1.3 fold changes in synaptic incorporation rate was implemented. The brief local syntheis upregulation can match the kinetics of GluA2 change but not the amplitude at 2 hours. The figure is adapted from [178].

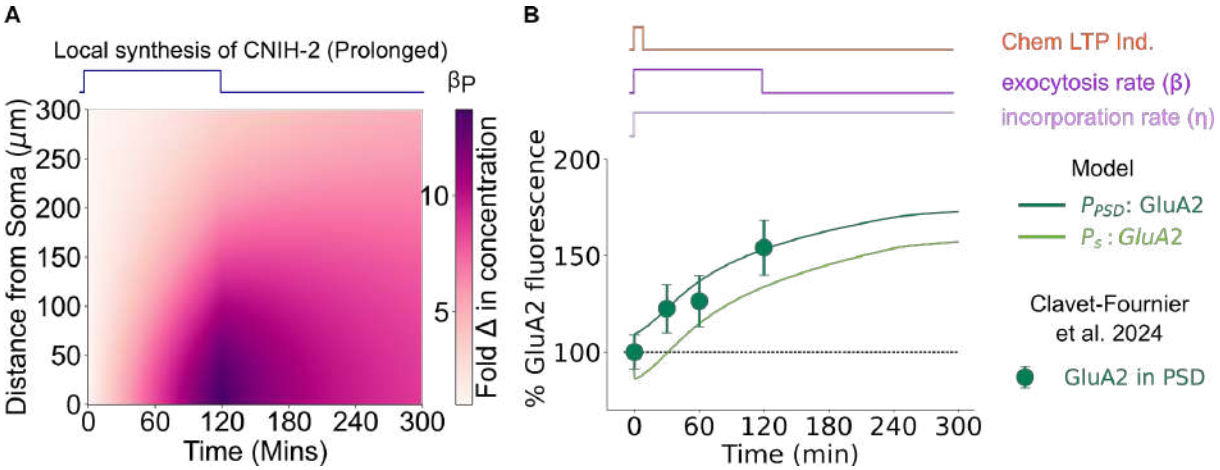

Figure 4.12.: **Prolonged CNIH-2 local synthesis can explain GluA2 dynamics upon chemical LTP induction**. **A)** Spatio temporal distribution CNIH-2 concentration upon increased local translation that persisted for 2 hours follwoing LTP induction. **B)** Changes in synaptic and surface GluA2 when changes in CNIH-2 was used as an increase in exocytosis rate, in addition a 1.3 fold changes in synaptic incorporation rate can match the kinetics and amplitude of GluA2 changes at 2 hours. The figure is adapted from [178].

Finally, I wanted to understand if the increased de novo protein synthesis has to occur in the dendrites in order to explain GluA2 dynamics. For this, I simulated a prolonged increase (by 500 folds) in somatic synthesis rate (J_{Pin} in Eq. 4.7) that lasted for 2 hours. This increase in somatic CNIH-2 synthesis led to only a marginal increase in dendritic CNIH-2 concentration,

as per my model prediction. Specifically, there was an initial 1.15-fold increase in the proximal dendrite after two hours of somatic upregulation, which diminished to a 1.05-fold increase after five hours Fig. 4.13.A.

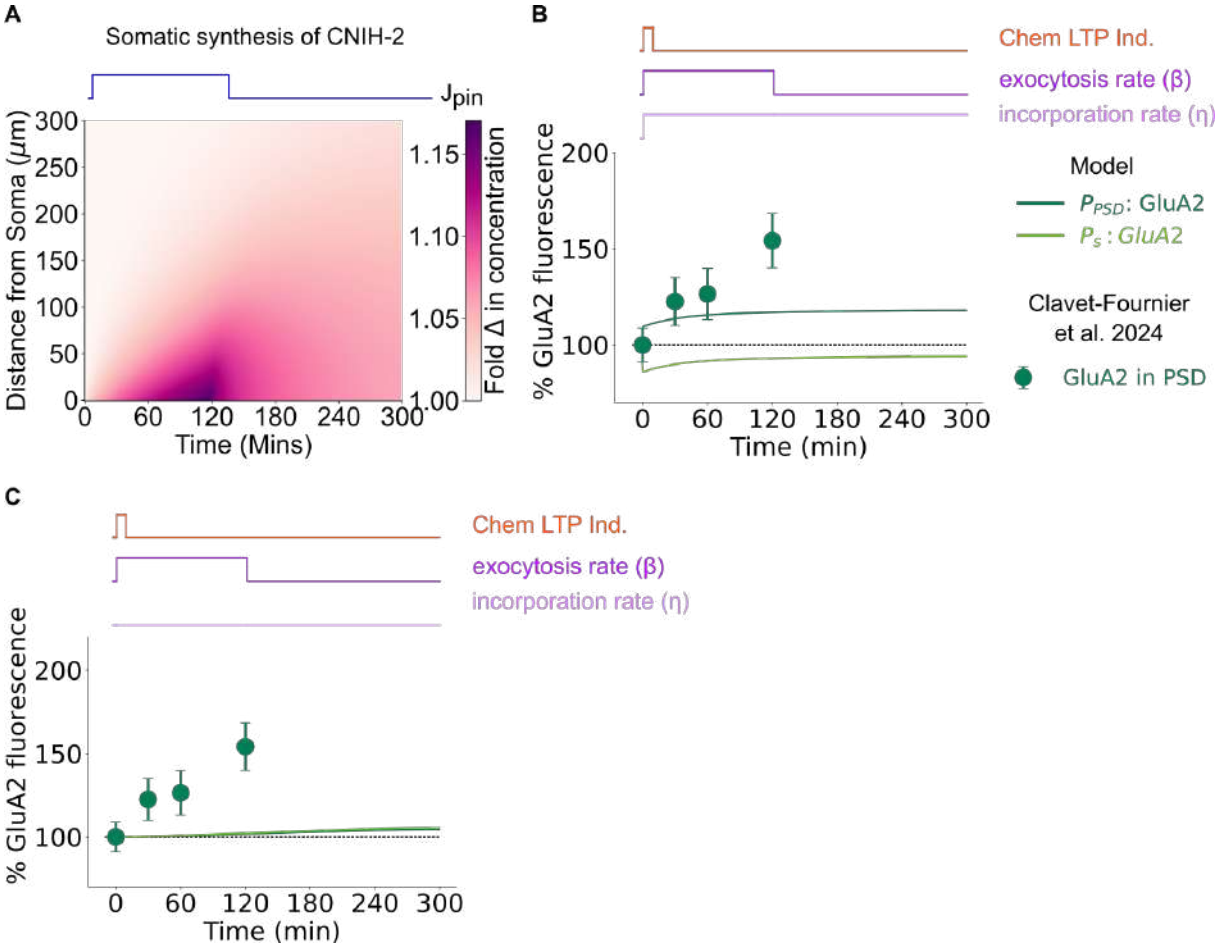

Figure 4.13.: **Prolonged somatic CNIH-2 synthesis has minuscule impact on GluA2 concentration upon chemical LTP induction**. **A)** Spatio temporal distribution CNIH-2 concentration upon increased somatic translation lasting for 2 hours. **B)** Changes in synaptic and surface GluA2 when changes in CNIH-2 was used as an increase in exocytosis rate. In addition a 1.3 fold changes in synaptic incorporation rate was implemented. **C)** same as **B** but without the change in synaptic incorporation rate. Change in exocytosis rate only hardly impacts the GluA2 concentration. The figure is adapted from [178].

Next, when I incorporated the time-dependent changes in CNIH-2 distribution into my mathematical model of AMPAR trafficking, I observed a marginal change of $\approx 15\%$ in the synaptic GluA2, significantly below the experimentally observed changes Fig. 4.13.B. This change was mostly due to the persistent changes in synaptic incorporation rate as without this enhanced synaptic trapping, the synaptic AMAPRs showed almost no change Fig. 4.13.C. I summarise the trafficking changes that I tried and whether they could explain GluA2-containing AMPAR

dynamics in Fig. 4.14.

CNIH-2 parameter change / Response	GluA2-containing AMPAR		
	Somatic Synthesis J_{pin}	Local synthesis (Brief) β_P	Local synthesis (Prolonged) β_P
Kinetics	✗	✗	✓
Amplitude	✗	✓	✓

Figure 4.14.: **Summary of parameter changes that can explain GluA2-conatining AMPAR changes upon chemical LTP induction**. The figure is adapted from [178].

4.7. Brief Summary

In this chapter, I described that AMPARs can display distinct responses to LTP induction by chemical application of glycine. Next, I showed that the GluA1-homomeric AMPARs show a fast insertion in the cell plasma membrane and accumulation at the synapse. However, the accumulation at the synapse is transient. On the other hand, GluA2-containing AMPAR shows a slower insertion into the neuronal surface, but it lasts for hours. The key mechanisms that result in this temporal difference can be the local synthesis of AMPAR auxiliary protein CNIH-2. I showed that *Cnih2* mRNA is dendrite-enriched and has its mRNA distributed across the entire neuronal tree. Then, using the FUNCAT-PLA experiment, we showed that the mRNA indeed gets actively translated in the dendrites, and the rate of translation increases upon chemical LTP induction. Following this, I showed that disrupting CNIH-2 translation leads to a specific reduction in membrane insertion of GluA2-containing AMPARs, and the GluA1-homomers are not affected by the knockdown of CNIH-2. Finally, my simulation showed that the dynamics of an increase in CNIH-2 concentration by up-regulation of the local synthesis rate could explain the temporal dynamics of synaptic GluA2 changes.

5. Conclusion

5.1. Main results

In Chapter 1, I described the general physiology of biological neurons and how they process information in the brain. The information transfer between neurons occurs mainly a subcellular structures called synapses. These synapses are known to change the efficiency of information transmission via a cellular process called synaptic plasticity. One of the known forms of synaptic plasticity is long-term potentiation or LTP.

5.1.1. Data analysis tool

In Chapter 2, I discussed a novel computational tool called "SpyDen" for continuous and discrete molecular localization and analysis inside dendrites and dendritic spine compartments. I developed this tool with a fellow master's student, Jean P. Filling, and a fellow PostDoc, Maximilian F. Eggl. I also described my contribution to developing an algorithmic solution to trace the neuronal dendritic tree in fluorescent-based imaging data automatically. I extended this feature to fully segment dendrites. I further developed a feature to detect and analyze fluorescent bright puncta to get meaningful statistics such as the fraction of molecular localization in somata vs. dendrite and the dendritic distribution of molecules as a function of the location along the dendrites.

5.1.2. AMPAR trafficking

In Chapter 3, I disccused a mathematical model for the trafficking of endogenous GluA2-containing AMPARs under basal conditions. In this model, I included the experimentally reported transport mechanisms that shape AMPAR distribution along the dendritic tree. The plasma membrane receptors can move laterally via diffusion, and intracellularly, AMPAR-containing vesicles are transported using motor protein-based active transport. Another mechanism that can impact the availability of AMPARs is local synthesis. However, analysis of the experimental data demonstrated that *Gria1* and *Gria2* mRNAs, encoding the two most abundant AMPAR pore-forming subunits, GluA1 and GluA2, are predominantly translated in the somatic

compartment under basal conditions. This finding suggests that local translation of these subunits is unlikely to account for the reported increase in GluA2 concentration at distal dendritic locations.

On the other hand, GluA2 protein distribution remained constant in the first 100 μm in the data. This is in contradiction with previous modeling studies, which predicted that proteins, including AMPARs, that are predominantly translated in the soma and utilize purely passive diffusion as means of transport show an exponentially decaying profile with dendritic distance [58, 19, 17]. With a novel mathematical model described using a PDE, I could explain these seemingly inconsistent profiles of mRNA and protein distribution for AMPARs. My model predicted that a biased active transport in an anterograde direction could increase the protein concentration towards the distal tip, even without dendritic mRNA translation.

Next, I extended my model to capture the intricate trafficking dynamics of three population of AMPARs with distinct functional compartments, namely their concentrations in the cell cytoplasm, on the cell surface, and at the PSD using a system of three coupled PDEs. By solving this model at a steady state and fitting the various parameters of the model to experimental data, I could generate various insights into the kinetics of AMPAR trafficking under basal conditions. First, my analysis revealed that at baseline, the rate of endocytosis of GluA2-containing AMPARs was higher than its exocytosis rate, resulting in an intracellular pool of approximately 70% of its total concentration. Second, the exocytosis to endocytosis rate ratio was constant in the 100 μm dendritic length, indicating that exocytosis frequency is likely the same throughout the dendritic tree, or at least in the first 100 μm. Third, using the model and experimental data analysis, I could predict that almost 50% of the surface AMPARs are bound to the PSD structures, and the remaining 50% constitute the mobile fraction that can be exchanged with the bound receptors. This finding is also in-line with experimental reports that utilized single particle tracking and fluorescence recovery after photobleaching (FRAP) techniques and estimated the fraction of immobile AMPARs to be between 30-50% [164, 78].

5.1.3. Central role of local synthesis in AMPAR subtype dynamics

In Chapter 4, I started with describing the differences in plasticity response of AMPAR subtypes [148, 42], with GluA1 homomers exhibiting rapid surface insertion and accumulation in PSDs [129, 162], whereas GluA2-containing heteromeric AMPARs display comparatively

slower synaptic accumulation [129, 31]. Using my modeling approach, I showed that an immediate increase in exocytosis and a modest rise in the synaptic incorporation rate was sufficient to recapitulate the rapid and transient accumulation of GluA1 homomeric AMPAR. Similar short-lasting change in exocytosis rate was not enough to capture the slow GluA2 dynamics observed experimentally [31]. Instead, an exocytosis the rate that changed with time was required to reproduce experimental data.

I propose that this time-dependent exocytosis is driven by local CNIH-2 concentration, an auxiliary protein known to regulate AMPAR trafficking and their synaptic accumulation. I showed that *Cnih2* mRNA is well localized in the dendrite and undergoes local translation there. I further showed that cLTP increased their local translation rate within a few minutes. Then, I showed that shRNA knockdown of *Cnih2* mRNA reduced CNIH-2 protein that in turn decreased surface expression of GluA2-containing AMPAR specifically. Finally, incorporating a local upregulation of CNIH-2 translation in my GLuA2 model as a driver of exocytosis helped reproduce the kinetics and amplitude of experimental GluA2 data. This upregulation in my model needed to last for hours as a brief upregulation lasting for 10 minutes provided the kinetic match but not the amplitude. Finally, an equivalent increase in somatic CNIH-2 influx had minimal effect on AMPAR concentration, highlighting the crucial contribution of local translation.

Finally, my results indicate an alternative pathway for AMPAR delivery to the synapse. GluA1 homomers presumably follow the conventional secretory route, undergoing processing via the somatic Golgi apparatus (GA), resulting in AMPARs with mature glycosylation profiles sensitive to Endonuclease H treatment. Conversely, GluA2-containing heteromers, synthesized at the surface of the somatic ER, may bypass GA membranes and directly reach the neuronal plasma membrane in dendrites. This process appears to be mediated by the local synthesis of CNIH-2, producing AMPARs with Endonuclease H-resistant glycans, as previously demonstrated [74]. While the details of molecular interaction between AMPAR and their auxiliary subunits is still an active area of research, my results provide critical perspicuity into how distinct AMPAR populations are selectively incorporated into synapses under various conditions. This selective incorporation has important implications for therapeutic strategies to restore or modulate AMPAR synaptic transmission and plasticity, which are often disrupted in neurological and neurodegenerative diseases.

5.2. Perspective

My work has several limitations regarding essential components of AMPAR transport. One limitation of my work is that I did not consider the modulation of active transport by neuronal activity and calcium influx. Experimental work shows that synaptic influx of Ca^{2+} can arrest active transport of AMPAR-containing vesicles and lead to their accumulation near stimulated spine[72]. This accumulation of AMPAR near stimulated spines represents an elevated pool of new receptors that can be exocytosed to meet plasticity needs. Additionally, in my three-population model (introduced in section 3.5), I have only considered a net, biased active transport. My model can be extended to include the anterograde and retrograde motion separately to study active transport modulation in detail.

Another limitation of my work is that I did not consider the impact of spine geometry (for example, spine neck), which can influence plasticity outcomes via AMPAR trafficking [68, 19, 10]. The spine neck poses a bottleneck for synaptic entry of proteins and mRNAs. In the current version of the model, I simplified these geometric constraints by considering only a single parameter for synaptic incorporation of AMPAR. This simplification allowed me to keep my model mathematically tractable. To study the effect of spine geometry, my model can be extended to include the spine neck as an additional compartment. As previous studies have pointed out, the diffusive trafficking can differ between neuronal surface and cytoplasm [138]. Another important geometric consideration is the nanoscale organization of PSD. Experimental work shows that PSD consists of substructures of dense domains that anchor AMPAR and can also undergo re-organization upon synaptic plasticity induction. My model can be used to study this by considering multiple PSD compartments and changing the number of slots under plasticity conditions.

A main assumption I made in this thesis is the dendrites are cylindrical. Tapering in biological dendrites is crucial in signal transmission from dendrites to soma. Biological dendrites also show random fluctuations in their radius to the presence of other dendrites, axons, blood vessels, and astrocytes. Future extensions of my model can study the effect of decreasing radius using an effective velocity towards the beginning of the dendrite. The second main assumption I made is that each spine on the model dendrite is identical in terms of slot numbers and synaptic incorporation rate. Synaptic plasticity outcomes depend on the initial size of the spines [26]. I am currently studying how spine size variation leads to changes in synaptic plasticity. For

this, I am modifying my model to set the initial sizes of the spines by drawing them from a lognormal-like distribution as shown by experiments [136].

Since its discovery, understanding synaptic plasticity mechanisms has been the focus of neuroscience research. In this thesis, I have provided novel and important insights into the mechanisms behind LTP. Over the last five decades, several other forms of synaptic plasticity have been discovered. For example, LTD leads to the weakening of synapses. Interestingly, LTD induction causes the removal of AMPARs from synapses and the internalization of extrasynaptic AMPARs [98, 8]. As a next step, my model can also be used to study the LTD. To study the LTD dynamics, one can change the endocytosis rate and investigate the removal of receptors from the PSD and neuronal surface. Another prominent form of synaptic plasticity is homeostatic scaling, which leads to a multiplicative strengthening or weakening of all the weights of a neuron [170]. Interestingly, the homeostatic scaling leads to an increase or decrease in AMPAR content at all the synapses. My model can be further extended to study mechanisms of homeostatic scaling. Heterosynaptic plasticity is another form of synaptic plasticity in which stimulation of one or more synapses leads to plasticity in unstimulated synapses that are near the stimulated synapses [25, 177]. Previous modeling work suggests that heterosynaptic plasticity can occur through competition for a shared pool of resources [169] and synaptic-cross talk [25, 177]. My model can be further extended to study heterosynaptic plasticity by including intracellular signaling such as AMPAR phosphorylation and dephosphorylation by CaMK2a and Protein phosphatase 1 (PP1) AMPARs.

These other forms of plasticity are important as they are crucial for network dynamics. For example, heterosynaptic plasticity is hypothesized as a mechanism to prevent run-away dynamics through weight-normalization [176, 120]. Weight normalization suggests that if some of the neurons weights are potentiated, others should depotentiate to keep the sum of all weights constant. Similarly, homeostatic scaling is also proposed as a weight normalization mechanism where all the neurons weights are scaled up or down in a multiplicative manner [170, 169]

Overall, I propose that bridging molecular processes with biologically plausible plasticity rules offers a promising avenue for advancing our understanding of neural circuit development, memory formation, behavior, and higher cognitive functions.

Bibliography

[1] G. Aakalu, W. B. Smith, N. Nguyen, C. Jiang, and E. M. Schuman. Dynamic visualization of local protein synthesis in hippocampal neurons. *Neuron*, 30(2):489–502, 2001.

[2] H. Adesnik and R. A. Nicoll. Conservation of glutamate receptor 2-containing ampa receptors during long-term potentiation. *Journal of Neuroscience*, 27(17):4598–4602, 2007.

[3] J. Ahlers, D. Althviz Moré, O. Amsalem, A. Anderson, G. Bokota, P. Boone, J. Bragantini, G. Buckley, A. Burt, M. Bussonnier, A. Can Solak, C. Caporal, D. Doncila Pop, K. Evans, J. Freeman, L. Gaifas, C. Gohlke, K. Gunalan, H. Har-Gil, M. Harfouche, K. I. S. Harrington, V. Hilsenstein, K. Hutchings, T. Lambert, J. Lauer, G. Lichtner, Z. Liu, L. Liu, A. Lowe, L. Marconato, S. Martin, A. McGovern, L. Migas, N. Miller, H. Muñoz, J.-H. Müller, C. Nauroth-KreSS, J. Nunez-Iglesias, C. Pape, K. Pevey, G. Peña-Castellanos, A. Pierré, J. Rodríguez-Guerra, D. Ross, L. Royer, C. T. Russell, G. Selzer, P. Smith, P. Sobolewski, K. Sofiiuk, N. Sofroniew, D. Stansby, A. Sweet, W.-M. Vierdag, P. Wadhwa, M. Weber Mendonça, J. Windhager, P. Winston, and K. Yamauchi. napari: a multi-dimensional image viewer for Python, July 2023. URL https://doi.org/10.5281/zenodo.8115575.

[4] G. Akbalik, K. Langebeck-Jensen, G. Tushev, S. Sambandan, J. Rinne, I. Epstein, I. Cajigas, I. Vlatkovic, and E. M. Schuman. Visualization of newly synthesized neuronal RNA in vitro and in vivo using click-chemistry. *RNA Biol.*, 14(1):20–28, Jan. 2017.

[5] B. K. Andrasfalvy and J. C. Magee. Distance-dependent increase in AMPA receptor number in the dendrites of adult hippocampal CA1 pyramidal neurons. *J. Neurosci.*, 21 (23):9151–9159, Dec. 2001.

[6] M. Antal, Y. Fukazawa, M. Eördögh, D. Muszil, E. Molnár, M. Itakura, M. Takahashi, and R. Shigemoto. Numbers, densities, and colocalization of ampa-and nmda-type glutamate receptors at individual synapses in the superficial spinal dorsal horn of rats. *Journal of Neuroscience*, 28(39):9692–9701, 2008.

[7] A. Ö. Argunşah, E. Erdil, M. U. Ghani, Y. Ramiro-Cortés, A. F. Hobbiss, T. Karayannis, M. Çetin, I. Israely, and D. Ünay. An interactive time series image analysis software for dendritic spines. *Scientific Reports*, 12(1):12405, 2022.

[8] M. C. Ashby, A. Sarah, G. S. Ralph, J. Uney, G. L. Collingridge, and J. M. Henley. Removal of ampa receptors (ampars) from synapses is preceded by transient endocytosis of extrasynaptic ampars. *Journal of Neuroscience*, 24(22):5172–5176, 2004.

[9] M. C. Ashby, S. R. Maier, A. Nishimune, and J. M. Henley. Lateral diffusion drives constitutive exchange of ampa receptors at dendritic spines and is regulated by spine morphology. *Journal of Neuroscience*, 26(26):7046–7055, 2006.

[10] M. K. Bell, C. T. Lee, and P. Rangamani. Spatiotemporal modelling reveals geometric dependence of ampar dynamics on dendritic spine morphology. *The Journal of Physiology*, 601(15):3329–3350, 2023.

[11] A. Bellotti, J. Murphy, L. Lin, R. Petralia, Y.-X. Wang, D. Hoffman, and T. O'Leary. Paradoxical relationships between active transport and global protein distributions in neurons. *Biophys. J.*, 120(11):2085–2101, June 2021.

[12] D. Bissen, F. Foss, and A. Acker-Palmer. Ampa receptors and their minions: auxiliary proteins in ampa receptor trafficking. *Cellular and Molecular Life Sciences*, 76: 2133–2169, 2019.

[13] T. V. Bliss and T. Lømo. Long-lasting potentiation of synaptic transmission in the dentate area of the anaesthetized rabbit following stimulation of the perforant path. *J. Physiol.*, 232(2):331–356, July 1973.

[14] A. J. Borgdorff and D. Choquet. Regulation of ampa receptor lateral movements. *Nature*, 417(6889):649–653, 2002.

[15] S. Boudkkazi, A. Brechet, J. Schwenk, and B. Fakler. Cornichon2 dictates the time course of excitatory transmission at individual hippocampal synapses. *Neuron*, 82(4): 848–858, May 2014.

[16] A. M. Bourke, A. Schwarz, and E. M. Schuman. De-centralizing the central dogma: mrna translation in space and time. *Molecular Cell*, 83(3):452–468, 2023.

[17] P. Bressloff and J. Newby. Directed intermittent search for hidden targets. *New Journal of Physics*, 11(2):023033, feb 2009. doi: 10.1088/1367-2630/11/2/023033. URL https://doi.org/10.1088/1367-2630/11/2/023033.

[18] P. C. Bressloff and B. A. Earnshaw. Diffusion-trapping model of receptor trafficking in dendrites. *Phys. Rev. E*, 75:041915, Apr 2007. doi: 10.1103/PhysRevE.75.041915. URL https://link.aps.org/doi/10.1103/PhysRevE.75.041915.

[19] P. C. Bressloff and J. M. Newby. Stochastic models of intracellular transport. *Reviews of Modern Physics*, 85(1):135, 2013.

[20] P. J. Brockie, M. Jensen, J. E. Mellem, E. Jensen, T. Yamasaki, R. Wang, D. Maxfield, C. Thacker, F. Hoerndli, P. J. Dunn, et al. Cornichons control er export of ampa receptors to regulate synaptic excitability. *Neuron*, 80(1):129–142, 2013.

[21] N. Burnashev, H. Monyer, P. H. Seeburg, and B. Sakmann. Divalent ion permeability of ampa receptor channels is dominated by the edited form of a single subunit. *Neuron*, 8 (1):189–198, 1992.

[22] I. J. Cajigas, G. Tushev, T. J. Will, S. tom Dieck, N. Fuerst, and E. M. Schuman. The local transcriptome in the synaptic neuropil revealed by deep sequencing and high-resolution imaging. *Neuron*, 74(3):453–466, May 2012.

[23] J. Canny. A computational approach to edge detection. *IEEE Transactions on pattern analysis and machine intelligence*, pages 679–698, 1986.

[24] S. Cauzzo, E. Bruno, D. Boulet, P. Nazac, M. Basile, A. L. Callara, F. Tozzi, A. Ahluwalia, C. Magliaro, L. Danglot, et al. A modular framework for multi-scale tissue imaging and neuronal segmentation. *Nature Communications*, 15(1):4102, 2024.

[25] T. E. Chater and Y. Goda. My neighbour heterodeconstructing the mechanisms underlying heterosynaptic plasticity. *Current Opinion in Neurobiology*, 67: 106–114, 2021. ISSN 0959-4388. doi: https://doi.org/10.1016/j.conb.2020.10.007. URL https://www.sciencedirect.com/science/article/pii/S095943882030146X. Neurobiology of Learning and Plasticity.

[26] T. E. Chater, M. F. Eggl, Y. Goda, and T. Tchumatchenko. Competitive processes shape multi-synapse plasticity along dendritic segments. *Nature Communications*, 15(1):7572, 2024.

[27] L. Chen, D. M. Chetkovich, R. S. Petralia, N. T. Sweeney, Y. Kawasaki, R. J. Wenthold, D. S. Bredt, and R. A. Nicoll. Stargazin regulates synaptic targeting of ampa receptors by two distinct mechanisms. *Nature*, 408(6815):936–943, 2000.

[28] M. A. Chirillo, M. S. Waters, L. F. Lindsey, J. N. Bourne, and K. M. Harris. Local resources of polyribosomes and ser promote synapse enlargement and spine clustering after long-term potentiation in adult rat hippocampus. *Scientific reports*, 9(1):3861, 2019.

[29] D. Choquet and E. Hosy. AMPA receptor nanoscale dynamic organization and synaptic plasticities. *Curr. Opin. Neurobiol.*, 63:137–145, Aug. 2020.

[30] C. Ciolli Mattioli, A. Rom, V. Franke, K. Imami, G. Arrey, M. Terne, A. Woehler, A. Akalin, I. Ulitsky, and M. Chekulaeva. Alternative 3 utrs direct localization of functionally diverse protein isoforms in neuronal compartments. *Nucleic acids research*, 47 (5):2560–2573, 2019.

[31] V. Clavet-Fournier, C. Lee, W. Wegner, N. Brose, J. Rhee, and K. I. Willig. Pre-and postsynaptic nanostructures increase in size and complexity after induction of long-term potentiation. *iScience*, 27(1), 2024.

[32] L. Cognet, B. Lounis, and D. Choquet. Tracking receptors using individual fluorescent and nonfluorescent nanolabels. *Cold Spring Harbor Protocols*, 2014(2):pdb–prot080416, 2014.

[33] L. D. Cohen, R. Zuchman, O. Sorokina, A. Müller, D. C. Dieterich, J. D. Armstrong, T. Ziv, and N. E. Ziv. Metabolic turnover of synaptic proteins: kinetics, interdependencies and implications for synaptic maintenance. *PloS one*, 8(5):e63191, 2013.

[34] I. D. Coombs, D. Soto, M. Zonouzi, M. Renzi, C. Shelley, M. Farrant, and S. G. Cull-Candy. Cornichons modify channel properties of recombinant and glial ampa receptors. *Journal of Neuroscience*, 32(29):9796–9804, 2012.

[35] K. Czöndör and O. Thoumine. Biophysical mechanisms regulating ampa receptor accumulation at synapses. *Brain Research Bulletin*, 93:57–68, 2013.

[36] K. Czöndör, M. Mondin, M. Garcia, M. Heine, R. Frischknecht, D. Choquet, J.-B. Sibarita, and O. R. Thoumine. Unified quantitative model of ampa receptor trafficking at synapses. *Proceedings of the National Academy of Sciences*, 109(9):3522–3527, 2012. doi: 10.1073/pnas.1109818109. URL https://www.pnas.org/doi/abs/10.1073/pnas.1109818109.

[37] M. E. da Silva, M. Adrian, P. Schätzle, J. Lipka, T. Watanabe, S. Cho, K. Futai, C. J. Wierenga, L. C. Kapitein, and C. C. Hoogenraad. Positioning of ampa receptor-containing endosomes regulates synapse architecture. *Cell reports*, 13(5):933–943, 2015.

[38] E. Danielson and S. H. Lee. Synpanal: software for rapid quantification of the density and intensity of protein puncta from fluorescence microscopy images of neurons. *PloS one*, 9(12):e115298, 2014.

[39] N. Das, E. Baczynska, M. Bijata, B. Ruszczycki, A. Zeug, D. Plewczynski, P. K. Saha, E. Ponimaskin, J. Wlodarczyk, and S. Basu. 3dspan: An interactive software for 3d segmentation and analysis of dendritic spines. *Neuroinformatics*, pages 1–20, 2021.

[40] V. A. Derkach, M. C. Oh, E. S. Guire, and T. R. Soderling. Regulatory mechanisms of ampa receptors in synaptic plasticity. *Nature Reviews Neuroscience*, 8(2):101–113, 2007.

[41] N. L. Desmond and W. B. Levy. Changes in the numerical density of synaptic contacts with long-term potentiation in the hippocampal dentate gyrus. *Journal of Comparative Neurology*, 253(4):466–475, 1986.

[42] G. H. Diering and R. L. Huganir. The ampa receptor code of synaptic plasticity. *Neuron*, 100(2):314–329, 2018.

[43] D. C. Dieterich and M. R. Kreutz. Proteomics of the synapse–a quantitative approach to neuronal plasticity. *Molecular & Cellular Proteomics*, 15(2):368–381, 2016.

[44] J. B. Ding, K. T. Takasaki, and B. L. Sabatini. Supraresolution imaging in brain slices

using stimulated-emission depletion two-photon laser scanning microscopy. *Neuron*, 63 (4):429–437, 2009.

[45] P. G. Donlin-Asp, C. Polisseni, R. Klimek, A. Heckel, and E. M. Schuman. Differential regulation of local mRNA dynamics and translation following long-term potentiation and depression. *Proc. Natl. Acad. Sci. U. S. A.*, 118(13):e2017578118, Mar. 2021.

[46] D. B. Dorman, J. Jedrzejewska-Szmek, and K. T. Blackwell. Inhibition enhances spatially-specific calcium encoding of synaptic input patterns in a biologically constrained model. *Elife*, 7, Oct. 2018.

[47] A. R. Dörrbaum, L. Kochen, J. D. Langer, and E. M. Schuman. Local and global influences on protein turnover in neurons and glia. *Elife*, 7:e34202, 2018.

[48] M. Doyle and M. A. Kiebler. Mechanisms of dendritic mrna transport and its role in synaptic tagging. *The EMBO journal*, 30(17):3540–3552, 2011.

[49] B. A. Earnshaw and P. C. Bressloff. Biophysical model of ampa receptor trafficking and its regulation during long-term potentiation/long-term depression. *Journal of Neuroscience*, 26(47):12362–12373, 2006. ISSN 0270-6474. doi: 10.1523/JNEUROSCI.3601-06.2006. URL https://www.jneurosci.org/content/26/47/12362.

[50] B. A. Earnshaw and P. C. Bressloff. Modeling the role of lateral membrane diffusion in ampa receptor trafficking along a spiny dendrite. *Journal of computational neuroscience*, 25:366–389, 2008.

[51] J. Eberwine, K. Miyashiro, J. E. Kacharmina, and C. Job. Local translation of classes of mrnas that are targeted to neuronal dendrites. *Proceedings of the National Academy of Sciences*, 98(13):7080–7085, 2001.

[52] M. F. Eggl, S. Wagle, J. P. Filling, T. E. Chater, Y. Goda, and T. Tchumatchenko. Spyden: Automating molecular and structural analysis across spines and dendrites. *bioRxiv*, pages 2024–06, 2024.

[53] M. D. Ehlers. Reinsertion or degradation of ampa receptors determined by activity-dependent endocytic sorting. *Neuron*, 28(2):511–525, 2000.

[54] M. D. Ehlers, M. Heine, L. Groc, M.-C. Lee, and D. Choquet. Diffusional trapping of glur1 ampa receptors by input-specific synaptic activity. *Neuron*, 54(3):447–460, 2007.

[55] P. Ekaterina, V. Peter, D. Smirnova, C. Vyacheslav, and B. Ilya. Spinetool is an open-source software for analysis of morphology of dendritic spines. *Scientific Reports*, 13(1): 10561, 2023.

[56] H. Ewers, T. Tada, J. D. Petersen, B. Racz, M. Sheng, and D. Choquet. A septin-dependent diffusion barrier at dendritic spine necks. *PloS one*, 9(12):e113916, 2014.

[57] M. H. Fernholz, D. A. Guggiana Nilo, T. Bonhoeffer, and A. M. Kist. Deepd3, an open framework for automated quantification of dendritic spines. *PLOS Computational Biology*, 20(2):e1011774, 2024.

[58] Y. Fonkeu, N. Kraynyukova, A.-S. Hafner, L. Kochen, F. Sartori, E. M. Schuman, and T. Tchumatchenko. How mrna localization and protein synthesis sites influence dendritic protein distribution and dynamics. *Neuron*, 103(6):1109–1122.e7, 2019. ISSN 0896-6273. doi: https://doi.org/10.1016/j.neuron.2019.06.022. URL https://www.sciencedirect.com/science/article/pii/S0896627319305720.

[59] S. Fujii, H. Tanaka, and T. Hirano. Suppression of ampa receptor exocytosis contributes to hippocampal ltd. *Journal of Neuroscience*, 38(24):5523–5537, 2018.

[60] S. B. Garcia, A. P. Schlotter, D. Pereira, F. Polleux, and L. Hammond. Respan: an accurate, unbiased and automated pipeline for analysis of dendritic morphology and dendritic spine mapping. *bioRxiv*, pages 2024–06, 2024.

[61] A. M. Getz, M. Ducros, C. Breillat, A. Lampin-Saint-Amaux, S. Daburon, U. François, A. Nowacka, M. Fernández-Monreal, E. Hosy, F. Lanore, et al. High-resolution imaging and manipulation of endogenous ampa receptor surface mobility during synaptic plasticity and learning. *Science Advances*, 8(30):eabm5298, 2022.

[62] J.-F. Gilles, P. Mailly, T. Ferreira, T. Boudier, and N. Heck. Spot spine, a freely available imagej plugin for 3d detection and morphological analysis of dendritic spines. *F1000Research*, 13:176, 2024.

[63] C. Glock, A. Biever, G. Tushev, B. Nassim-Assir, A. Kao, I. Bartnik, S. tom Dieck, and E. M. Schuman. The translatome of neuronal cell bodies, dendrites, and axons. *Proceedings of the National Academy of Sciences*, 118(43):e2113929118, 2021.

[64] N. W. Gray, R. M. Weimer, I. Bureau, and K. Svoboda. Rapid redistribution of synaptic PSD-95 in the neocortex in vivo. *PLoS Biol.*, 4(11):e370, Nov. 2006.

[65] L. Groc and D. Choquet. Linking glutamate receptor movements and synapse function. *Science*, 368(6496):eaay4631, 2020.

[66] S. Y. Grooms, K.-M. Noh, R. Regis, G. J. Bassell, M. K. Bryan, R. C. Carroll, and R. S. Zukin. Activity bidirectionally regulates ampa receptor mrna abundance in dendrites of hippocampal neurons. *Journal of Neuroscience*, 26(32):8339–8351, 2006.

[67] E. S. Guire, M. C. Oh, T. R. Soderling, and V. A. Derkach. Recruitment of calcium-permeable ampa receptors during synaptic potentiation is regulated by cam-kinase i. *Journal of Neuroscience*, 28(23):6000–6009, 2008.

[68] R. Gupta and C. ODonnell. Dendritic spine neck plasticity controls synaptic expression of long-term potentiation. *bioRxiv*, pages 2023–01, 2023.

[69] A.-S. Hafner, P. G. Donlin-Asp, B. Leitch, E. Herzog, and E. M. Schuman. Local protein synthesis is a ubiquitous feature of neuronal pre- and postsynaptic compartments. *Science*, 364(6441):eaau3644, 2019. doi: 10.1126/science.aau3644.

[70] A. Hagberg, P. Swart, and D. S Chult. Exploring network structure, dynamics, and function using networkx. Technical report, Los Alamos National Lab.(LANL), Los Alamos, NM (United States), 2008.

[71] W. O. Hancock. Bidirectional cargo transport: moving beyond tug of war. *Nat. Rev. Mol. Cell Biol.*, 15(9):615–628, Sept. 2014.

[72] E. Hangen, F. P. Cordelières, J. D. Petersen, D. Choquet, and F. Coussen. Neuronal activity and intracellular calcium levels regulate intracellular transport of newly synthesized ampar. *Cell reports*, 24(4):1001–1012, 2018.

[73] J. G. Hanley. Actin-dependent mechanisms in ampa receptor trafficking. *Frontiers in cellular neuroscience*, 8:381, 2014.

[74] C. Hanus, H. Geptin, G. Tushev, S. Garg, B. Alvarez-Castelao, S. Sambandan, L. Kochen, A.-S. Hafner, J. D. Langer, and E. M. Schuman. Unconventional secretory processing diversifies neuronal ion channel properties. *elife*, 5:e20609, 2016.

[75] N. Harmel, B. Cokic, G. Zolles, H. Berkefeld, V. Mauric, B. Fakler, V. Stein, and N. Klöcker. Ampa receptors commandeer an ancient cargo exporter for use as an auxiliary subunit for signaling. *PloS one*, 7(1):e30681, 2012.

[76] K. He, L. Song, L. W. Cummings, J. Goldman, R. L. Huganir, and H.-K. Lee. Stabilization of ca2+-permeable ampa receptors at perisynaptic sites by glur1-s845 phosphorylation. *Proceedings of the National Academy of Sciences*, 106(47):20033–20038, 2009.

[77] D. O. Hebb. *The organization of behavior: A neuropsychological theory*. New York: John Wiley Sons, 1949.

[78] M. Heine, L. Groc, R. Frischknecht, J.-C. Béïque, B. Lounis, G. Rumbaugh, R. L. Huganir, L. Cognet, and D. Choquet. Surface mobility of postsynaptic ampars tunes synaptic transmission. *Science*, 320(5873):201–205, 2008.

[79] M. S. Helm, T. M. Dankovich, S. Mandad, B. Rammner, S. Jähne, V. Salimi, C. Koerbs, R. Leibrandt, H. Urlaub, T. Schikorski, and S. O. Rizzoli. A large-scale nanoscopy and biochemistry analysis of postsynaptic dendritic spines. *Nat. Neurosci.*, 24(8):1151–1162, Aug. 2021.

[80] J. M. Henley, E. A. Barker, and O. O. Glebov. Routes, destinations and delays: recent advances in ampa receptor trafficking. *Trends in neurosciences*, 34(5):258–268, 2011.

[81] B. E. Herring, Y. Shi, Y. H. Suh, C.-Y. Zheng, S. M. Blankenship, K. W. Roche, and R. A. Nicoll. Cornichon proteins determine the subunit composition of synaptic ampa receptors. *Neuron*, 77(6):1083–1096, 2013.

[82] V. A. Herzog, N. Fasching, and S. L. Ameres. Determining mRNA stability by metabolic RNA labeling and chemical nucleoside conversion. *Methods Mol. Biol.*, 2062:169–189, 2020.

[83] N. Hirokawa. Kinesin and dynein superfamily proteins and the mechanism of organelle transport. *Science*, 279(5350):519–526, 1998.

[84] N. Hirokawa and R. Takemura. Molecular motors and mechanisms of directional transport in neurons. *Nat. Rev. Neurosci.*, 6(3):201–214, Mar. 2005.

[85] F. J. Hoerndli, D. A. Maxfield, P. J. Brockie, J. E. Mellem, E. Jensen, R. Wang, D. M. Madsen, and A. V. Maricq. Kinesin-1 regulates synaptic strength by mediating the delivery, removal, and redistribution of ampa receptors. *Neuron*, 80(6):1421–1437, 2013.

[86] C. E. Holt and E. M. Schuman. The central dogma decentralized: new perspectives on rna function and local translation in neurons. *Neuron*, 80(3):648–657, 2013.

[87] N. Honkura, M. Matsuzaki, J. Noguchi, G. C. Ellis-Davies, and H. Kasai. The subspine organization of actin fibers regulates the structure and plasticity of dendritic spines. *Neuron*, 57(5):719–729, 2008.

[88] T. Hosokawa, D. A. Rusakov, T. Bliss, and A. Fine. Repeated confocal imaging of individual dendritic spines in the living hippocampal slice: evidence for changes in length and orientation associated with chemically induced ltp. *Journal of Neuroscience*, 15(8): 5560–5573, 1995.

[89] R. L. Huganir and R. A. Nicoll. Ampars and synaptic plasticity: the last 25 years. *Neuron*, 80(3):704–717, 2013.

[90] V. K. Inavalli, M. O. Lenz, C. Butler, J. Angibaud, B. Compans, F. Levet, J. Tønnesen, O. Rossier, G. Giannone, O. Thoumine, et al. A super-resolution platform for correlative live single-molecule imaging and sted microscopy. *Nature methods*, 16(12):1263–1268, 2019.

[91] M. Joensuu, P. Padmanabhan, N. Durisic, A. T. Bademosi, E. Cooper-Williams, I. C. Morrow, C. B. Harper, W. Jung, R. G. Parton, G. J. Goodhill, et al. Subdiffractional tracking of internalized molecules reveals heterogeneous motion states of synaptic vesicles. *Journal of Cell Biology*, 215(2):277–292, 2016.

[92] Y. Jung, J.-Y. Seo, H. G. Ryu, D.-Y. Kim, K.-H. Lee, and K.-T. Kim. Bdnf-induced local translation of glua1 is regulated by hnrnp a2/b1. *Science Advances*, 6(47):eabd2163, 2020.

[93] H. Kang and E. M. Schuman. A requirement for local protein synthesis in neurotrophin-induced hippocampal synaptic plasticity. *Science*, 273(5280):1402–1406, 1996.

[94] A. S. Kato, M. B. Gill, H. Yu, E. S. Nisenbaum, and D. S. Bredt. Tarps differentially decorate ampa receptors to specify neuropharmacology. *Trends in neurosciences*, 33(5): 241–248, 2010.

[95] M. Kneussel and W. Wagner. Myosin motors at neuronal synapses: drivers of membrane transport and actin dynamics. *Nature Reviews Neuroscience*, 14(4):233–247, 2013.

[96] M. L. Kokolaki, A. Fauquier, and M. Renner. Molecular crowding and diffusion-capture in synapses. *IScience*, 23(8), 2020.

[97] H.-B. Kwon and B. L. Sabatini. Glutamate induces de novo growth of functional spines in developing cortex. *Nature*, 474(7349):100–104, 2011.

[98] H.-K. Lee, K. Kameyama, R. L. Huganir, and M. F. Bear. Nmda induces long-term synaptic depression and dephosphorylation of the glur1 subunit of ampa receptors in hippocampus. *Neuron*, 21(5):1151–1162, 1998.

[99] H.-K. Lee, K. Takamiya, J.-S. Han, H. Man, C.-H. Kim, G. Rumbaugh, S. Yu, L. Ding, C. He, R. S. Petralia, et al. Phosphorylation of the ampa receptor glur1 subunit is required for synaptic plasticity and retention of spatial memory. *Cell*, 112(5):631–643, 2003.

[100] K. F. Lee, C. Soares, J.-P. Thivierge, and J.-C. Béïque. Correlated synaptic inputs drive dendritic calcium amplification and cooperative plasticity during clustered synapse development. *Neuron*, 89(4):784–799, 2016.

[101] S. H. Lee, C. Jin, E. Cai, P. Ge, Y. Ishitsuka, K. W. Teng, A. A. De Thomaz, D. Nall, M. Baday, O. Jeyifous, et al. Super-resolution imaging of synaptic and extra-synaptic ampa receptors with different-sized fluorescent probes. *Elife*, 6:e27744, 2017.

[102] M. Lemieux, S. Labrecque, C. Tardif, É. Labrie-Dion, É. Lebel, and P. De Koninck. Translocation of CaMKII to dendritic microtubules supports the plasticity of local synapses. *J. Cell Biol.*, 198(6):1055–1073, Sept. 2012.

[103] F. Levet, J. Tønnesen, U. V. Nägerl, and J.-B. Sibarita. Spinej: a software tool for quantitative analysis of nanoscale spine morphology. *Methods*, 174:49–55, 2020.

[104] T. P. Li, Y. Song, H. D. MacGillavry, T. A. Blanpied, and S. Raghavachari. Protein crowding within the postsynaptic density can impede the escape of membrane proteins. *J. Neurosci.*, 36(15):4276–4295, Apr. 2016.

[105] D.-T. Lin, Y. Makino, K. Sharma, T. Hayashi, R. Neve, K. Takamiya, and R. L. Huganir. Regulation of ampa receptor extrasynaptic insertion by 4.1 n, phosphorylation and palmitoylation. *Nature neuroscience*, 12(7):879–887, 2009.

[106] Z. Liu, L. D. Lavis, and E. Betzig. Imaging live-cell dynamics and structure at the single-molecule level. *Molecular cell*, 58(4):644–659, 2015.

[107] R. W. Livingstone, M. K. Elder, A. Singh, C. M. Westlake, W. P. Tate, W. C. Abraham, and J. M. Williams. Secreted amyloid precursor protein-alpha enhances ltp through the synthesis and trafficking of ca2+-permeable ampa receptors. *Frontiers in Molecular Neuroscience*, 14:660208, 2021.

[108] M. London and M. Häusser. Dendritic computation. *Annu. Rev. Neurosci.*, 28:503–532, 2005.

[109] J. C. Magee. Dendritic hyperpolarization-activated currents modify the integrative properties of hippocampal ca1 pyramidal neurons. *Journal of Neuroscience*, 18(19): 7613–7624, 1998.

[110] M. Masugi-Tokita, E. Tarusawa, M. Watanabe, E. Molnár, K. Fujimoto, and R. Shigemoto. Number and density of ampa receptors in individual synapses in the rat cerebellum as revealed by sds-digested freeze-fracture replica labeling. *Journal of Neuroscience*, 27 (8):2135–2144, 2007.

[111] S. Matsuda, W. Kakegawa, T. Budisantoso, T. Nomura, K. Kohda, and M. Yuzaki. Stargazin regulates ampa receptor trafficking through adaptor protein complexes during long-term depression. *Nature communications*, 4(1):2759, 2013.

[112] M. Matsuzaki, N. Honkura, G. C. Ellis-Davies, and H. Kasai. Structural basis of long-term potentiation in single dendritic spines. *Nature*, 429(6993):761–766, 2004.

[113] F. R. Maxfield and T. E. McGraw. Endocytic recycling. *Nature reviews Molecular cell biology*, 5(2):121–132, 2004.

[114] E. Mohr. Subcellular RNA compartmentalization. *Prog. Neurobiol.*, 57(5):507–525, Apr. 1999.

[115] M. J. I. Müller, S. Klumpp, and R. Lipowsky. Tug-of-war as a cooperative mechanism for bidirectional cargo transport by molecular motors. *Proceedings of the National Academy of Sciences*, 105(12):4609–4614, 2008. doi: 10.1073/pnas.0706825105. URL https://www.pnas.org/doi/abs/10.1073/pnas.0706825105.

[116] U. V. Nägerl and T. Bonhoeffer. Imaging living synapses at the nanoscale by sted microscopy. *Journal of Neuroscience*, 30(28):9341–9346, 2010.

[117] D. Nair, E. Hosy, J. D. Petersen, A. Constals, G. Giannone, D. Choquet, and J.-B. Sibarita. Super-resolution imaging reveals that AMPA receptors inside synapses are dynamically organized in nanodomains regulated by PSD95. *J. Neurosci.*, 33(32): 13204–13224, Aug. 2013.

[118] J. Newby and P. C. Bressloff. Local synaptic signaling enhances the stochastic transport of motor-driven cargo in neurons. *Physical Biology*, 7(3):036004, aug 2010. doi: 10.1088/1478-3975/7/3/036004. URL https://doi.org/10.1088/1478-3975/7/3/036004.

[119] N. Ofer, D. R. Berger, N. Kasthuri, J. W. Lichtman, and R. Yuste. Ultrastructural analysis of dendritic spine necks reveals a continuum of spine morphologies. *Developmental neurobiology*, 81(5):746–757, 2021.

[120] E. Oja. Simplified neuron model as a principal component analyzer. *Journal of mathematical biology*, 15(3):267–273, 1982.

[121] P. Opazo, S. Labrecque, C. M. Tigaret, A. Frouin, P. W. Wiseman, P. De Koninck, and D. Choquet. Camkii triggers the diffusional trapping of surface ampars through phosphorylation of stargazin. *Neuron*, 67(2):239–252, 2010.

[122] E. Osterweil, D. G. Wells, and M. S. Mooseker. A role for myosin vi in postsynaptic structure and glutamate receptor endocytosis. *The Journal of cell biology*, 168(2): 329–338, 2005.

[123] P. Padmanabhan, A. Kneynsberg, and J. Götz. Super-resolution microscopy: a closer look at synaptic dysfunction in alzheimer disease. *Nature Reviews Neuroscience*, 22 (12):723–740, 2021.

[124] H. Y. Park, A. R. Buxbaum, and R. H. Singer. Single mRNA tracking in live cells. *Methods Enzymol.*, 472:387–406, 2010.

[125] P. Park, T. M. Sanderson, M. Amici, S.-L. Choi, Z. A. Bortolotto, M. Zhuo, B.-K. Kaang, and G. L. Collingridge. Calcium-permeable ampa receptors mediate the induction of the protein kinase a-dependent component of long-term potentiation in the hippocampus. *Journal of Neuroscience*, 36(2):622–631, 2016.

[126] P. Park, H. Kang, T. M. Sanderson, Z. A. Bortolotto, J. Georgiou, M. Zhuo, B.-K. Kaang, and G. L. Collingridge. On the role of calcium-permeable ampars in long-term potentiation and synaptic tagging in the rodent hippocampus. *Frontiers in synaptic neuroscience*, 11:4, 2019.

[127] P. Park, J. Georgiou, T. M. Sanderson, K.-H. Ko, H. Kang, J.-i. Kim, C. A. Bradley, Z. A. Bortolotto, M. Zhuo, B.-K. Kaang, et al. Pka drives an increase in ampa receptor unitary conductance during ltp in the hippocampus. *Nature Communications*, 12(1):413, 2021.

[128] M. Passafaro, V. Piëch, and M. Sheng. Subunit-specific temporal and spatial patterns of ampa receptor exocytosis in hippocampal neurons. *Nature neuroscience*, 4(9):917–926, 2001.

[129] M. A. Patterson, E. M. Szatmari, and R. Yasuda. Ampa receptors are exocytosed in stimulated spines and adjacent dendrites in a ras-erk–dependent manner during long-term potentiation. *Proceedings of the National Academy of Sciences*, 107(36): 15951–15956, 2010. doi: 10.1073/pnas.0913875107. URL https://www.pnas.org/doi/abs/10.1073/pnas.0913875107.

[130] P. S. Pirbhoy, S. Farris, and O. Steward. Synaptic activation of ribosomal protein s6 phosphorylation occurs locally in activated dendritic domains. *Learning & Memory*, 23 (6):255–269, 2016.

[131] K. Plant, K. A. Pelkey, Z. A. Bortolotto, D. Morita, A. Terashima, C. J. McBain, G. L. Collingridge, and J. T. Isaac. Transient incorporation of native glur2-lacking ampa receptors during hippocampal long-term potentiation. *Nature neuroscience*, 9(5):602–604, 2006.

[132] M. Rabani, J. Z. Levin, L. Fan, X. Adiconis, R. Raychowdhury, M. Garber, A. Gnirke, C. Nusbaum, N. Hacohen, N. Friedman, I. Amit, and A. Regev. Metabolic labeling of RNA uncovers principles of RNA production and degradation dynamics in mammalian cells. *Nat. Biotechnol.*, 29(5):436–442, May 2011.

[133] V. Rangaraju, S. tom Dieck, and E. M. Schuman. Local translation in neuronal compartments: how local is local? *EMBO reports*, 18(5):693–711, 2017.

[134] A. Rodriguez, D. B. Ehlenberger, D. L. Dickstein, P. R. Hof, and S. L. Wearne. Automated three-dimensional detection and shape classification of dendritic spines from fluorescence microscopy images. *PloS one*, 3(4):e1997, 2008.

[135] M. Rosendale, D. Jullié, D. Choquet, and D. Perrais. Spatial and temporal regulation of receptor endocytosis in neuronal dendrites revealed by imaging of single vesicle formation. *Cell reports*, 18(8):1840–1847, 2017.

[136] N. Rößler, T. Jungenitz, A. Sigler, A. Bird, M. Mittag, J. S. Rhee, T. Deller, H. Cuntz, N. Brose, S. W. Schwarzacher, et al. Skewed distribution of spines is independent of presynaptic transmitter release and synaptic plasticity, and emerges early during adult neurogenesis. *Open Biology*, 13(8):230063, 2023.

[137] J. Russo, A. M. Heck, J. Wilusz, and C. J. Wilusz. Metabolic labeling and recovery of nascent RNA to accurately quantify mRNA stability. *Methods*, 120:39–48, May 2017.

[138] F. Sartori, A.-S. Hafner, A. Karimi, A. Nold, Y. Fonkeu, E. M. Schuman, and T. Tchumatchenko. Statistical laws of protein motion in neuronal dendritic trees. *Cell reports*, 33(7):108391, 2020.

[139] J. T. Savage, J. J. Ramirez, W. C. Risher, Y. Wang, D. Irala, and C. Eroglu. Synbot is an open-source image analysis software for automated quantification of synapses. *Cell Reports Methods*, 4(9), 2024.

[140] L. Schermelleh, A. Ferrand, T. Huser, C. Eggeling, M. Sauer, O. Biehlmaier, and G. P. Drummen. Super-resolution microscopy demystified. *Nature cell biology*, 21(1):72–84, 2019.

[141] J. Schindelin, I. Arganda-Carreras, E. Frise, V. Kaynig, M. Longair, T. Pietzsch, S. Preibisch, C. Rueden, S. Saalfeld, B. Schmid, et al. Fiji: an open-source platform for biological-image analysis. *Nature methods*, 9(7):676–682, 2012.

[142] C. Schmied, T. Soykan, S. Bolz, V. Haucke, and M. Lehmann. Synactj: easy-to-use automated analysis of synaptic activity. *Frontiers in Computer Science*, 3:777837, 2021.

[143] J. Schwenk, N. Harmel, G. Zolles, W. Bildl, A. Kulik, B. Heimrich, O. Chisaka, P. Jonas, U. Schulte, B. Fakler, et al. Functional proteomics identify cornichon proteins as auxiliary subunits of ampa receptors. *Science*, 323(5919):1313–1319, 2009.

[144] I. Segev. Dendritic processing. the handbook of brain theory and neural networks, 1995.

[145] B. Selvakumar, M. A. Jenkins, N. K. Hussain, R. L. Huganir, S. F. Traynelis, and S. H. Snyder. S-nitrosylation of ampa receptor glua1 regulates phosphorylation, single-channel conductance, and endocytosis. *Proceedings of the National Academy of Sciences*, 110 (3):1077–1082, 2013.

[146] S. I. Shah, H. L. Ong, A. Demuro, and G. Ullah. Punctaspecks: a tool for automated detection, tracking, and analysis of multiple types of fluorescently labeled biomolecules. *Cell calcium*, 89:102224, 2020.

[147] M. Sheng and C. C. Hoogenraad. The postsynaptic architecture of excitatory synapses: a more quantitative view. *Annu. Rev. Biochem.*, 76(1):823–847, 2007.

[148] S.-H. Shi, Y. Hayashi, J. A. Esteban, and R. Malinow. Subunit-specific rules governing ampa receptor trafficking to synapses in hippocampal pyramidal neurons. *Cell*, 105(3): 331–343, 2001.

[149] Y. Shi, Y. H. Suh, A. D. Milstein, K. Isozaki, S. M. Schmid, K. W. Roche, and R. A. Nicoll. Functional comparison of the effects of tarps and cornichons on ampa receptor trafficking and gating. *Proceedings of the National Academy of Sciences*, 107(37): 16315–16319, 2010.

[150] S. L. Shipman, B. E. Herring, Y. H. Suh, K. W. Roche, and R. A. Nicoll. Distance-dependent scaling of ampars is cell-autonomous and glua2 dependent. *Journal of Neuroscience*, 33(33):13312–13319, 2013.

[151] S. J. Singer and G. L. Nicolson. The fluid mosaic model of the structure of cell membranes: Cell membranes are viewed as two-dimensional solutions of oriented globular proteins and lipids. *Science*, 175(4023):720–731, 1972.

[152] M. S. Song, H. C. Moon, J.-H. Jeon, and H. Y. Park. Neuronal messenger ribonucleoprotein transport follows an aging l√©vy walk. *Nature Communications*, 9(1): 344, Jan 2018. ISSN 2041-1723. doi: 10.1038/s41467-017-02700-z. URL https://doi.org/10.1038/s41467-017-02700-z.

[153] O. Steward and E. M. Schuman. Protein synthesis at synaptic sites on dendrites. *Annu. Rev. Neurosci.*, 24(1):299–325, 2001.

[154] O. Steward and C. S. Wallace. mRNA distribution within dendrites: relationship to afferent innervation. *J. Neurobiol.*, 26(3):447–449, Mar. 1995.

[155] O. Steward, C. S. Wallace, G. L. Lyford, and P. F. Worley. Synaptic activation causes the mrna for the ieg arc to localize selectively near activated postsynaptic sites on dendrites. *Neuron*, 21(4):741–751, 1998.

[156] C. Straub and S. Tomita. The regulation of glutamate receptor trafficking and function by tarps and other transmembrane auxiliary subunits. *Current opinion in neurobiology*, 22(3):488–495, 2012.

[157] G. Stuart, N. Spruston, and M. Häusser. *Dendrites*. Oxford University Press, 2016.

[158] J. F. Sturgill, P. Steiner, B. L. Czervionke, and B. L. Sabatini. Distinct domains within PSD-95 mediate synaptic incorporation, stabilization, and activity-dependent trafficking. *J. Neurosci.*, 29(41):12845–12854, oct 2009.

[159] T. Sumi and K. Harada. Mechanism underlying hippocampal long-term potentiation and depression based on competition between endocytosis and exocytosis

of ampa receptors. *Scientific Reports*, 10(1):14711, Sep 2020. ISSN 2045-2322. doi: 10.1038/s41598-020-71528-3. URL https://doi.org/10.1038/s41598-020-71528-3.

[160] C. Sun, A. Nold, C. M. Fusco, V. Rangaraju, T. Tchumatchenko, M. Heilemann, and E. M. Schuman. The prevalence and specificity of local protein synthesis during neuronal synaptic plasticity. *Sci. Adv.*, 7(38):eabj0790, Sept. 2021.

[161] M. A. Sutton, H. T. Ito, P. Cressy, C. Kempf, J. C. Woo, and E. M. Schuman. Miniature neurotransmission stabilizes synaptic function via tonic suppression of local dendritic protein synthesis. *Cell*, 125(4):785–799, May 2006.

[162] H. Tanaka and T. Hirano. Visualization of subunit-specific delivery of glutamate receptors to postsynaptic membrane during hippocampal long-term potentiation. *Cell reports*, 1(4):291–298, 2012.

[163] S. J. Tang and E. M. Schuman. Protein synthesis in the dendrite. *Philosophical Transactions of the Royal Society of London. Series B: Biological Sciences*, 357(1420):521–529, 2002.

[164] C. Tardin, L. Cognet, C. Bats, B. Lounis, and D. Choquet. Direct imaging of lateral movements of AMPA receptors inside synapses. *EMBO J.*, 22(18):4656–4665, Sept. 2003.

[165] R. P. Tas, A. Chazeau, B. M. C. Cloin, M. L. A. Lambers, C. C. Hoogenraad, and L. C. Kapitein. Differentiation between oppositely oriented microtubules controls polarized neuronal transport. *Neuron*, 96(6):1264–1271.e5, Dec. 2017.

[166] R. D. Taylor, M. Heine, N. J. Emptage, and L. C. Andreae. Neuronal receptors display cytoskeleton-independent directed motion on the plasma membrane. *Iscience*, 10: 234–244, 2018.

[167] S. tom Dieck, L. Kochen, C. Hanus, M. Heumüller, I. Bartnik, B. Nassim-Assir, K. Merk, T. Mosler, S. Garg, S. Bunse, D. A. Tirrell, and E. M. Schuman. Direct visualization of newly synthesized target proteins in situ. *Nat. Methods*, 12(5):411–414, May 2015.

[168] S. Tomita, L. Chen, Y. Kawasaki, R. S. Petralia, R. J. Wenthold, R. A. Nicoll, and D. S. Bredt. Functional studies and distribution define a family of transmembrane AMPA receptor regulatory proteins. *J. Cell Biol.*, 161(4):805–816, May 2003.

[169] J. Triesch, A. D. Vo, and A.-S. Hafner. Competition for synaptic building blocks shapes synaptic plasticity. *eLife*, 7:e37836, sep 2018. ISSN 2050-084X. doi: 10.7554/eLife.37836. URL https://doi.org/10.7554/eLife.37836.

[170] G. G. Turrigiano, K. R. Leslie, N. S. Desai, L. C. Rutherford, and S. B. Nelson. Activity-dependent scaling of quantal amplitude in neocortical neurons. *Nature*, 391(6670):892–896, Feb. 1998.

[171] G. Tushev, C. Glock, M. Heumüller, A. Biever, M. Jovanovic, and E. M. Schuman. Alternative 3' UTRs modify the localization, regulatory potential, stability, and plasticity of mRNAs in neuronal compartments. *Neuron*, 98(3):495–511.e6, May 2018.

[172] A. Van Harreveld and E. Fifkova. Swelling of dendritic spines in the fascia dentata after stimulation of the perforant fibers as a mechanism of post-tetanic potentiation. *Experimental neurology*, 49(3):736–749, 1975.

[173] W. Vandenberghe, R. A. Nicoll, and D. S. Bredt. Interaction with the unfolded protein response reveals a role for stargazin in biosynthetic ampa receptor transport. *Journal of Neuroscience*, 25(5):1095–1102, 2005.

[174] I. Vidaurre-Gallart, I. Fernaud-Espinosa, N. Cosmin-Toader, L. Talavera-Martínez, M. Martin-Abadal, R. Benavides-Piccione, Y. Gonzalez-Cid, L. Pastor, J. DeFelipe, and M. García-Lorenzo. A deep learning-based workflow for dendritic spine segmentation. *Frontiers in Neuroanatomy*, 16, 2022.

[175] F. W. Vogel, S. Alipek, J.-B. Eppler, P. Osuna-Vargas, J. Triesch, D. Bissen, A. Acker-Palmer, S. Rumpel, and M. Kaschube. Utilizing 2d-region-based cnns for automatic dendritic spine detection in 3d live cell imaging. *Scientific Reports*, 13(1):20497, 2023.

[176] C. Von der Malsburg. Self-organization of orientation sensitive cells in the striate cortex. *Kybernetik*, 14(2):85–100, 1973.

[177] S. Wagle, N. Kraynyukova, A.-S. Hafner, and T. Tchumatchenko. Computational insights into mrna and protein dynamics underlying synaptic plasticity rules. *Molecular and Cellular Neuroscience*, 125:103846, 2023.

[178] S. Wagle, M. K. Kracht, A. Bührke, A. Acker-Palmer, N. Kraynyukova, A.-S. Hafner, E. M. Schuman, and T. Tchumatchenko. An integrative model of ampa receptor trafficking reveals the central contribution of local translation in subtype-specific kinetics. *bioRxiv*, 2025. doi: 10.1101/2025.02.08.637220. URL https://www.biorxiv.org/content/early/2025/02/08/2025.02.08.637220.

[179] W. Wagner, K. Lippmann, F. F. Heisler, K. V. Gromova, F. L. Lombino, M. K. Roesler, Y. Pechmann, S. Hornig, M. Schweizer, S. Polo, et al. Myosin vi drives clathrin-mediated ampa receptor endocytosis to facilitate cerebellar long-term depression. *Cell reports*, 28 (1):11–20, 2019.

[180] Y. Wang, C. Wang, P. Ranefall, G. J. Broussard, Y. Wang, G. Shi, B. Lyu, C.-T. Wu, Y. Wang, L. Tian, et al. Synquant: an automatic tool to quantify synapses from microscopy images. *Bioinformatics*, 36(5):1599–1606, 2020.

[181] Z. Wang, J. G. Edwards, N. Riley, D. W. Provance, R. Karcher, X.-d. Li, I. G. Davison, M. Ikebe, J. A. Mercer, J. A. Kauer, et al. Myosin vb mobilizes recycling endosomes and ampa receptors for postsynaptic plasticity. *Cell*, 135(3):535–548, 2008.

[182] R. J. Wenthold, R. S. Petralia, A. Niedzielski, et al. Evidence for multiple ampa receptor complexes in hippocampal ca1/ca2 neurons. *Journal of Neuroscience*, 16(6):1982–1989, 1996.

[183] A. H. Williams, C. O'Donnell, T. J. Sejnowski, and T. O'Leary. Dendritic trafficking faces physiologically critical speed-precision tradeoffs. *Elife*, 5, Dec. 2016.

[184] Y. Yang, X.-b. Wang, and Q. Zhou. Perisynaptic glur2-lacking ampa receptors control the reversibility of synaptic and spines modifications. *Proceedings of the National Academy of Sciences*, 107(26):11999–12004, 2010.

[185] Y. Youn, G. W. Lau, Y. Lee, B. K. Maity, E. Gouaux, H. J. Chung, and P. R. Selvin. Quantitative dna-paint imaging of ampa receptors in live neurons. *Cell Reports Methods*, 3(2), 2023.

[186] Y. Yu, L. M. Adsit, and I. T. Smith. Comprehensive software suite for functional analysis and synaptic input mapping of dendritic spines imaged in vivo. *Neurophotonics*, 11(2): 024307–024307, 2024.

[187] Z. Zhou, A. Liu, S. Xia, C. Leung, J. Qi, Y. Meng, W. Xie, P. Park, G. L. Collingridge, and Z. Jia. The c-terminal tails of endogenous glua1 and glua2 differentially contribute to hippocampal synaptic plasticity and learning. *Nature neuroscience*, 21(1):50–62, 2018.

List of Publications

My PhD research work led to the following publications:

- **Surbhit Wagle**, Nataliya Kraynyukova, Anne-Sophie Hafner, Tatjana Tchumatchenko. "Computational insights into mRNA and protein dynamics underlying synaptic plasticity rules" *Molecular and Cellular Neuroscience* 125 (2023): 103846. [177]

- Maximilian F. Eggl*, **Surbhit Wagle***, Jean P. Filling*, Thomas E. Chater, Yukiko Goda, and Tatjana Tchumatchenko. "SpyDen: Automating molecular and structural analysis across spines and dendrites". *bioRxiv*, (2024): 2024-06. *: co-first authors [52]

- **Surbhit Wagle**, Maximilian K. Kracht, Anne Bührke, Amparo Acker-Plamer, Nataliya Kraynyukova, Anne-Sophie Hafner, Erin M. Schuman, and Tatjana Tchumatchenko. "An integrative model of AMPA receptor trafficking reveals the central contribution of local translation in subtype-specific kinetics". *bioRxiv*, (2025): 2025-02. [178]

A. Appendix A

A.1. Adjusting dendritic path and width calculation

Here, I describe how to improve the optimal path and dendritic width calculation. The user should adjust the threshold so that the signal-to-noise ratio (SNR) is optimal before providing the start and end points of the dendrite. Empirically, I observed a median threshold to work better Fig. A.1. However, one should be careful not to keep the threshold too high such that the segments of the dendrite are removed. The best solution is to try different threshold values and choose one that gives a high SNR with the full dendrite visible.

In figure Fig. A.1&D., I show how threshold value impacts the middle axis path.

Once the optimal path is calculated, SpyDen allows further optimization of dendritic width calculations. For this, two sliders are provided. First is the smoothness factor. The raw width values calculated using 2, can be abrupt due to missing edges or spine edges. Hence, SpyDen uses a sliding window averaging to smoothen the dendritic width. This is based on the fact that dendrites do not abruptly broaden or become narrower. The smoothness factor helps adjust the size of the sliding window. The optimal value for this factor depends on the image resolution and quality. However, once the optimal value for this factor is found, SpyDen automatically uses the optimal value for other images for the same dataset.

The second factor is the thickness factor. This factor broadens or narrows down the width in a multiplicative manner. This is included to allow users to estimate the actual width of the dendrite. For example, if the dendrites were labeled using immunolabeling of MAP2 (which is a microtubular protein) instead of GFP fill, then the actual width of the dendrite is proportional to the MAP2 signal. This factor takes care of the proportionality and can produce the absolute width.

In Fig. A.1.G&H., I show the impact of these two factors on the dendritic width calculation. Finally, I summarize the benefit of using SpyDen compared to other tools in Table A.3.

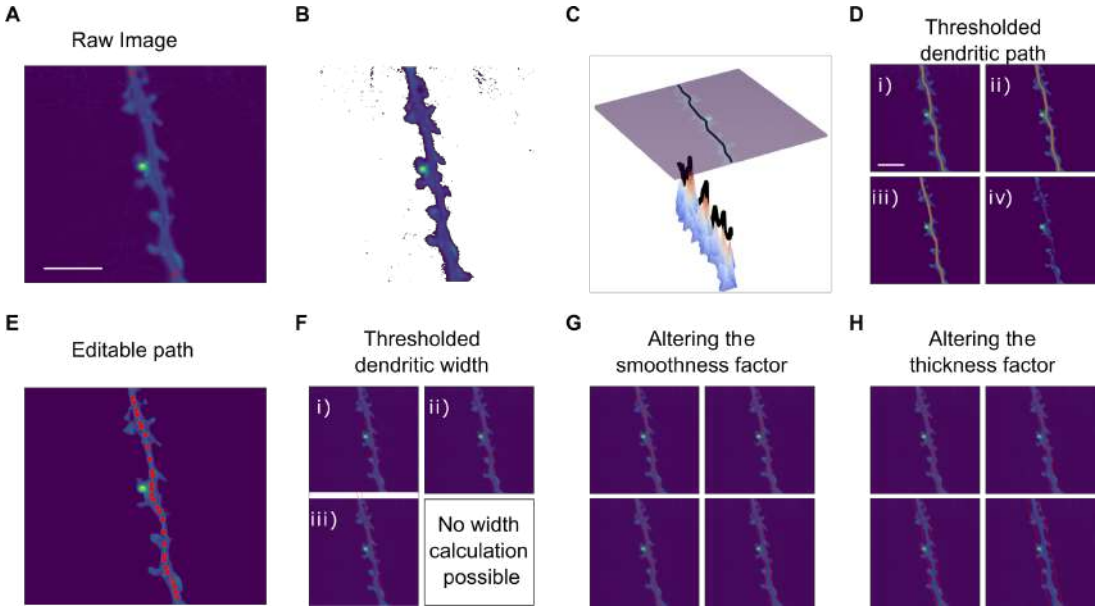

Figure A.1.: **Median threshold on the raw image allows optimization of medial axis paths for the dendrites and dendritic width calculation. A)** An example image, along with start and end points (marked in red), is provided to the pipeline for medial axis path calculation. **B)** SpyDen generates a filtered image (using default threshold value) that has a better signal-to-noise ratio. **C)** SpyDen generates a weighted matrix (see 3D plot) for the filtered image to calculate the shortest path that traverses the highest points. These highest points represent the center of the dendrite. **D)** Adjusting the threshold values can lead to more or less features getting filtered out. The updated dendritic paths (marked with the orange line). Each of the 4 sub-images (*i* to *iv*) depicts the optimal path for higher threshold values. Note that case *iv)* filtered too much of the dendrite out (with a very high threshold value), and so no optimal path was found. **E)** The user can edit the generated path using the nodes (highlighted by the red circles) by dragging them and or adding/deleting new nodes. **F)** The medial axis path can calculate dendritic width (red lines on either side of the dendrite) for a selected threshold value. A very high threshold can lead to the removal of the actual dendritic segment, and hence, a width calculation is not possible, as shown in *iv*. **G)-H)** Users can tune parameters to adjust dendritic width calculation. These parameters include the smoothness factor in (G), which determines the length of the sliding window to calculate the average width. A higher smoothness factor results in larger sliding windows and less abrupt width values. The second parameter is the width thickness factor (H), which multiplies the outward pointing normals by a set value. Altering these values can have a substantial effect on the calculated width and allow for a significant amount of flexibility for the user. The threshold dendritic with from *F*iii) was used. Figure adapted from [52].

A.2. Algorithms

Here, I write the pseudocode for the algorithmic procedure used for calculating the median axis path.

Algorithm 1 Finding of the dendritic medial axis path

Require: : Image of dendrite and spines, I, threshold t, start point ρ_s and end point p_e

Perform a threshold of I with value t to obtain a binarised image E of dendrite and spines.
for each pixel e_{ij} with pixel coordinates ij in E **do**
    if e_{ij} == 1 **then**
        create a node n_{ij} in the Graph G. ij are the preserved coordinates of the nodes.
    end if
end for
Cost map for shortest path
for every node n_{ij} in G **do**
    $n_{i'j'}$ is nearest neighbour with $i'j' \in \{(i+1)j, i(j+1), (i+1)(k+1), ...\}$(8 combinations)
    if $n_{i'j'}$ exists **then**
        create edge $e_{iji'j'}$ between nodes n_{ij} and $n_{i'j'}$ with value $|(i-i', j-j')|$ (1 or $\sqrt{2}$) in Graph G
    end if
end for
Cost Map for following boundaries
Make a copy G' of G and set incrementer for every node $i_{i'j'}$
Make a copy G'' of G'
while nodes $n''_{i''j''}$ exist in G'' **do**
    for all nodes $n''_{i''j''}$ in G'' **do**
        if number of edges for $n''_{i''j''} < 8$ **then** remove node $n''_{i''j''}$ and corresponding edges
        end if
        if $n_{i''j''}$ in G'' **then**
            set $i_{i'j'} = i_{i'j'} + 1$
        end if
    end for
end while
invert assigned values $i_{i'j'}$ in G'
Cost Graph $C = \lambda\, G + \eta\, G'$ with $\lambda + \eta = 1$
Perform Dijkstra algorithm on C from node p_s to p_e to obtain medial axis path which penalises walking on boundaries.

Here, I write the pseudocode for the algorithmic procedure used for calculating the dendritic width.

Algorithm 2 Finding of the dendritic width

Require: : Image, I, Set of spatially ordered dendritic points on the medial axis path , $\vec{d}$, Canny edge variance, σ

1: Perform a canny image detection on I and generate a Boolean matrix C of the contour of the dendrite
2: Create a place holder array W for the width data of size length($\vec{d}$) x 4
3: incrementer $i = 0$
4: **for** each point d_i in $\vec{d}$ **do**
5: Create a boolean matrix E of an ellipse ϵ with the center d_i
6: Minor axis in the direction of the next neighbor d_{i+1} with a fixed radius of $r_{min} = 2$ Pixel
7: For the major axis radius I set an incrementer $r_{maj} = 1$ Pixel and a counter $c = 0$
8: **while** sum(Intersection(C, E) < 1 or $c < 30$ **do**
9: Create a new E with $r_{maj} = 1.2 \cdot r_{maj}$
10: $c = c + 1$
11: **end while**
12: The angle of the ellipse can be calculated with $a = arcsin((d_{i+1} - d_i)_x r_m in/(r_{min}))$
13: W_i = (d_i, r_{min}, r_{maj}, a)
14: i = i + 1
15: **end for**
16: A Maximum increase condition of the width within two neighbours of the medial axis path is applied
17: From W the boolean mask of the segmented dendrite can be obtained

A.3. Structure of the SpyDen output

SpyDen stores the output in multiple file formats including .csv and .json for the statistics and .npy and .ROI for the ROIs. These multiple output formats are used so that the output can be exported into other tools for further analysis.

▶ Dendrite analysis output file

In Table A.1, I describe the output file structure that stores the statistics on dendrites

Dendrite_Channel_0.csv	
Column Name	**Definition**
Dendrite: d	pair of x,y coordinates of the point along the medial axis of dendrite
Width of ell.	width of the calculated ellipse at point x,y
Timestep t (Luminosity (mid.))[a]	Fluorescent intensity of the point on the medial axis at timestep t
Timestep t (Luminosity (ell.))[a]	Mean fluorescent intensity of all the pixels within the dendritic width (calculated using the ellipse approach) at timestep t

Table A.1.: Output file contains measurements for individual dendritic ROIs. [a] a separate column is added for each time step. A separate file is created for each channel as well.

▶ Puncta analysis output file

In Table A.1, I describe the output file structure that stores the statistics on puncta detected in the dendrite, spines, and soma.

dend_puncta.csv and soma_puncta.csv	
Column Name	**Definition**
Id	Unique identification number assigned to each punctum.
channel	Number of channels for which the punctum is located on
RoiId	Identification number of the dendritic ROI to which the punctum belongs
snapshot	Time point in a time series data to which the punctum belongs
location	Pair of x,y coordinate on the image for the punctum
radius	Radius of the circular punctum
max	Maximum fluorescent intensity of the punctum
min	Minimum fluorescent intensity of the punctum
mean	Mean fluorescent intensity of the punctum
std	Standard deviation of fluorescent intensities of the punctum.
median	Median fluorescent intensity of the punctum
distance	Distance from the start of dendritic ROI along the ROI

Table A.2.: output file containing measurements for individual punctum from puncta detection pipeline

Package Name	Codebase	ROI creation (Dendrites/ Spines/Puncta)	ROI Stata (Dendrites/ Spines/Puncta)	Multi-channel	Time-series	GUI	Exe-cutable	Man-ual edits	Output formats	2D/3D	Last up-load (date)
SpyDen	Python	SA / A / A	✓/ ✓/ ✓	✓	✓	✓	✓	S, DI	.json,.csv, .roi,.npy	2D	Jul 2024
Neurobits [171]	MATLAB	M / M / A	✗/ ✗/ ✓	✓	✗	✗	✗	✗	.csv	2D	Jun 2018
StarSearch	MATLAB	M / M / A	✗/ ✗/ ✓	✓	✗	✗	✗	✗	.csv	2D/3D	Mar 2022
SynPAnal [38]	Java	M / M / A	✓/ ✓/ ✓	✓	✗	✓	✓	S,DI	.xlsx	2D	Mar 2015
Punctaspecks [146]	MATLAB	✗/ ✗/ A	✗/ ✗/ ✓	✓	✓	✓	✗	S	.csv	2D	May 2020
DeepD3 [57]	Python	A / A / ✗	✗/ ✗/ ✗	✗	✗	✓	✓	S	.tif,.roi, .hdf5	2D/3D	Mar 2024
SpineS [7]	MATLAB	A / A /✗	✗/✓/✗	✗	✓	✓	✗	DI	.mat,.csv	3D	Aug 2022
Spot Spine [62]	Java	✗/ SA / ✗	✗/✓/✗	✗	✗	✓	✓	S,DI	.swc,.csv	3D/2D	Jun 2024
AUTOTUNE [186]	MATLAB	SA / SA / ✗	✓/✓/✗	✗	✓	✓	✗	S	.mat	2D	Jun 2024
SpineTool [55]	Python	✗/ A /✗	✗/✓/✗	✗	✗	✗	✗	DI	.off, .csv	3D	Jul 2023
RESPAN [60]	Python	A / A / ✗	✗/✓/✗	✗	✓	✓	✓	✗	.csv	3D/2D	Aug 2024
SENPAI [24]	MATLAB	A / A /✗	✓/✓/✗	✗	✗	✓	✗	✗	.mat	3D	Mar 2024
DeepSpine-Tool [174]	Python	A / A /✗	✓/✓/✗	✗	✓	✓	✓	✗	.tif	3D	Mar 2022
SpineJ [103]	Java	A / A / ✗	✗/✓/✗	✗	✓	✓	✓	DI	.roi	2D	Mar 2020
SynQuant [180]	Java	A / A / ✗	✓/✓/✗	✓	✗	✓	✓	✗	.roi	2D/3D	Jul 2020
3dSpAn [39]	C++	A/A/✗	✗/✓/✗	✗	✗	✓	✓	S	.csv,.tiff, .img	3D	Jul 2022
SynActJ [142]	Java	✗/ A /✗	✗/✓/✗	✗	✓	✓	✓	✗	.csv	2D	Dec 2021
SynBot [139]	ImageJ Macro	✗/ A / ✗	✗/ ✓/ ✗	✓	✗	✓	✓	✗	.csv, .tif	2D	Dec 2024

Table A.3.: A non-exclusive list of tools that offer analysis of dendrite, spine, and puncta. I considered tools published from 2015 to 2024. Abbreviations: SA: Semi-Automated (requiring minimal manual input); A: Automated (without requiring any manual input), M: Manual; S: Sliders, DI: Direct Intervention; ✗: Not supported, ✓: Supported

A.4. Parameter values used for various models

In this section, I describe the range of parameter values reported for the different trafficking methods involved in AMPAR trafficking. In Table A.4, are the values based on published experimental literature and model fitting. In Table A.5, I list the parameter values used for GluA1 homomeric AMPAR. These values were obtained from the previous model of GluA1 AMPARs and experimental measures. The values I used for CNIH-2 protein and *Cnih2* mRNA model are described in Table A.6 and Table A.7, respectively.

Parameter (symbol, units)	**GluAs**[a]		**Reference(s)**
Velocity of active transport (V_p, μm/s)	1.		[72]
Diffusion rates (D_s, D_c, μm^2/s)	0.01 - 1		[61, 9, 91]
exocytosis rate (β, s^{-1})	1.3×10^{-3}		[37]
Number of slots (ω)	60		[117]
Exit from PSD rate(γ, s^{-1})	1.1×10^{-3} - 2.3×10^{-2}		[54, 101]
Parameter (symbol,units)	**GluA2**	**GluA1**	**References(s)**
half-life ($T_{1/2}$, days)	1.95-3.12	0.5-4.35	[47, 33]
endocytosis rate (α, s^{-1})	5.89×10^{-4}	4.94×10^{-4}	[135]
Incorporation into PSD rate (η, s^{-1})	0.0007	0.0003	our model for GluA2 and [68] for GluA1

Table A.4.: Experimentally reported parameters measured in dendrites of hippocampal cultured neurons; a) includes values that are comparable for both GluA1/2 subunits or if the value is reported only for one of the subunits.

Parameter (symbol, units)	**Value**	**References(s)**
D_s, D_c (μm^2/s)	0.1	[14]
V_p (μm/s)	1×10^{-4}	our study
λ_c (s^{-1})	1.8×10^{-6} ($T_{1/2} = 4.53$ days)	[47, 33]
λ_s (s^{-1})	0	our study
α (s^{-1})	5×10^{-4}	[135]
β (s^{-1})	8.5×10^{-4}	[59]
η (s^{-1})	3×10^{-4}	[68]
γ (s^{-1})	2.3×10^{-2}	[54, 101]

Table A.5.: Parameter values used for steady-state, baseline model of GluA1-homomeric AMPARs.

Parameter (symbol, units)	Value	References(s)
D_p (μm^2/s)	1.5	[14]
V_p (μm/s)	0	our study
K_p (s^{-1})	1.4×10^{-6} ($T_{1/2} = 5.6$ days)	[47]
β_p (s^{-1})	0.01	our study
J_{Pin} (protein $\mu m/s$)	0.01	our study

Table A.6.: Parameter values used for steady-state, baseline model of CNIH-2 protein.

Parameter (symbol, units)	Value	References(s)
D_R (μm^2/s)	3.43×10^{-3}	[14]
v_R (μm/s)	2.1×10^{-3}	our study
K_R (s^{-1})	1.9×10^{-5} ($T_{1/2} = 10$ hours)	[47]
J_{Rin} (mRNA $\mu m/s$)	0.003	our study

Table A.7.: Parameter values used for steady-state, baseline model of *Cnih2* mRNA.

A.5. Steady state solution for the total AMPA receptors density on a finite domain

In the neurons, AMPAR is primarily produced in the soma under basal conditions and is transported along the dendrites via active intracellular transport as well as diffusion within both the plasma membrane and intracellular compartments. This dynamics of a protein (ρ) along the dendrites can be described using PDEs:

$$\frac{\partial \rho(x,t)}{\partial t} = D\frac{\partial^2 \rho(x,t)}{\partial x^2} - V\frac{\partial \rho(x,t)}{\partial x} - \lambda\rho(x,t). \tag{A.1}$$

The LHS in this equation represents the time-dependent changes in protein concentration. The terms on the RHS represent diffusion (D), active transport (V), and degradation (λ), respectively. To solve this equation at equilibrium, I can set the time-dependent term on the LHS to 0 and rewrite the Eq. A.1 as an ODE:

$$0 = D\frac{d^2 \rho(x,t)}{dx^2} - V\frac{d\rho(x,t)}{dx} - \lambda\rho(x,t). \tag{A.2}$$

The Eq. A.2 can be solved analytically using two boundary conditions. For this, I assume that the concentration of the protein (ρ) satisfies the boundary conditions

$$V\rho - D\frac{d\rho}{dx}\bigg|_0 = J_{influx} \tag{A.3}$$

$$V\rho - D\frac{d\rho}{dx}\bigg|_L = 0, \tag{A.4}$$

whereby $J_{influx} > 0$ is the rate of protein influx in the dendrite from the soma and Eq. A.4 means that no proteins come out of the dendritic tip located at a distance L from the soma.

The steady-state solution of the Eq (Eq. A.1) (i.e., solution under the assumption $\frac{\partial\rho(x,t)}{\partial t} = 0$) is a sum of two exponential functions

$$\rho(x) = C_1 e^{-K_1 x} + C_2 e^{-K_2 x} \tag{A.5}$$

whereby $K_{1,2} = \frac{-V \pm \sqrt{V^2+4D\lambda}}{2D}$. We compute the constants C_1, C_2 using the boundary conditions in (Eq. A.3), (Eq. A.4) and obtain the steady state dendritic distribution of the protein

$$\rho(x) = \frac{J_{influx}}{e^{-K_1 L} - e^{-K_2 L}} \left(\frac{e^{-K_2 x - K_1 L}}{V + DK_2} - \frac{e^{-K_1 x - K_2 L}}{V + DK_1} \right). \tag{A.6}$$

A.6. Steady state solution for the three population model

To derive the steady-state solutions of the model in Eq. 3.6 - Eq. 3.8, I assumed that the time derivatives of the functions ρ_s, ρ_c and ρ_{psd} are equal to 0 and obtain the following system of ODE

$$D_c\frac{d^2\rho_c}{dx^2} - V_p\frac{d\rho_c}{dx} - \lambda_c\rho_c - \beta\rho_c + \alpha\rho_s = 0 \tag{A.7}$$

$$D_s\frac{d^2\rho_s}{dx^2} - \lambda_s\rho_s - \alpha\rho_s + \beta\rho_c - \eta\rho_s(\omega - \rho_{psd}) + \gamma\rho_{psd} = 0 \tag{A.8}$$

$$\eta\rho_s(\omega - \rho_{psd}) - \gamma\rho_{psd} = 0. \tag{A.9}$$

The relation in Eq. A.9 implies that the steady-state of the synaptic proteins (ρ_{psd}) is related to the steady-state concentration of the proteins in the cell membrane,i.e.:

$$\rho_{psd}(x) = \eta\rho_s\omega/(\eta\rho_s(x) + \gamma) \tag{A.10}$$

Combining Eq. A.8 and Eq. A.9,I reduce the system in Eq. A.7-Eq. A.9 to two ODEs

$$\begin{aligned} D_c\frac{d^2\rho_c}{dx^2} - V_p\frac{d\rho_c}{dx} + \alpha\rho_s - \beta\rho_c - \lambda_c\rho_c = 0 \\ D_s\frac{d^2\rho_s}{dx^2} + \beta\rho_c - \alpha\rho_s - \lambda_s\rho_s = 0. \end{aligned} \tag{A.11}$$

Using the substitution $L_c = \frac{d\rho_c}{dx}$, $L_s = \frac{d\rho_s}{dx}$ I transform the system of two ODEs of the second order to the system of four first-order ODEs

$$\begin{aligned} \frac{d\rho_s}{dx} &= L_s \\ \frac{d\rho_c}{dx} &= L_c \\ D_s\frac{dL_s}{dx} &= \alpha\rho_s + \lambda_s\rho_s - \beta\rho_c \\ D_c\frac{dL_c}{dx} &= V_pL_c + \beta\rho_c + \lambda_c\rho_c - \alpha\rho_s. \end{aligned} \tag{A.12}$$

This system of equations can be solved with four boundary conditions. For this, I assumed that the functions ρ_c and ρ_s fulfill the following boundary conditions:

$$\begin{aligned} \left.\frac{d\rho_s}{dx}\right|_L &= 0 \\ V_p\rho_c - D_c\left.\frac{d\rho_c}{dx}\right|_L &= 0. \end{aligned} \tag{A.13}$$

This boundary condition is based on the fact that both surface and cytoplasmic receptors don't escape the dendrite at the tip of the dendrite.

Next, I assume that the proteins ρ_c produced in the soma are released in the cytoplasm, the surface at $x = 0$ with a constant influx rate J_{cin} J_{sin} respectively, i.e.,

$$\begin{aligned} D_s\left.\frac{d\rho_s}{dx}\right|_0 &= J_{sin} \\ V_p\rho_c - D_c\left.\frac{d\rho_c}{dx}\right|_0 &= J_{cin}, \end{aligned} \tag{A.14}$$

here, $J_{cin} > 0$ and $J_{sin} = 0$ were used for simulations as I assumed no direct flux into the surface from the soma and the receptors are directly exocytosed in the dendrites. Finally, I used the *solve_bvp* function of Python language to numerically solve the Eq. A.12.

A.7. Time-dependent solution of the AMPA receptor trafficking model

To study plasticity-dependent changes in AMPAR concentration in different compartments (for both GluA1 homomeric and GluA2-containing heteromeric receptors), I used the original time-dependent model in Eq. 3.6-Eq. 3.8 and compute its solution numerically. To this end, I discretize the spatial variable of the PDE ($\Delta x = 1\ \mu$m) and transform the system of PDE into a system of ODEs

$$\begin{aligned}
\frac{d\rho_c}{dt} &= \frac{D_c}{(\Delta x)^2}\left(\rho_{c,i+1} - 2\rho_{c,i} + \rho_{c,i-1}\right) - \frac{V_p}{\Delta x}\left(\rho_{c,i+1} - \rho_{c,i}\right) - (\lambda_c + \beta)\rho_{c,i} + \alpha P_{s,i} \\
\frac{d\rho_s}{dt} &= \frac{D_s}{(\Delta x)^2}\left(\rho_{s,i+1} - 2\rho_{s,i} + \rho_{s,i-1}\right) - (\lambda_s + \alpha)\rho_{s,i} + \beta\rho_{c,i} - \eta\rho^j_{s,i}(\omega - \rho^j_{psd,i}) + \gamma\rho^j_{psd,i} \\
\frac{d\rho_{psd}}{dt} &= \eta\rho^j_{s,i}(\omega - \rho^j_{psd,i}) - \gamma\rho^j_{psd,i}.
\end{aligned}$$

I determine ρ_s, ρ_c at all intermediate spatial nodes ($i = 1, ..., L-1$). For the boundary nodes ($i = 0, L$), I use the boundary conditions Eq. A.13-Eq. A.14 at $x = 0$ and $x = L$ as I assume that these boundary conditions are satisfied at all time. Using the boundary conditions, I can write the discretized equation for the boundary nodes as:

$$\begin{aligned}
\left.\frac{d\rho_c}{dt}\right|_0 &= \left(\frac{D_c}{\Delta x^2} - \frac{V_p}{\Delta x}\right)\rho_{c,1} - \left(\frac{D_c}{\Delta x^2} + \lambda_c + \beta\right)\rho_{c,0} + \frac{J_{cin}}{\Delta x} + \alpha\rho_{s,0} \\
\left.\frac{d\rho_s}{dt}\right|_0 &= \frac{D_s}{\Delta x^2}\rho_{s,1} - \left(\frac{D_s}{\Delta x^2} + \lambda_s + \alpha\right)\rho_{s,0} + \frac{J_{sin}}{\Delta x} + \beta\rho_{c,0} - \eta\rho_{s,0}(\omega - \rho_{psd,0)+\gamma\rho_{psd,0}} \\
\left.\frac{d\rho_c}{dt}\right|_L &= \frac{D_c}{\Delta x^2}\rho_{c,L-1} - \left(\frac{D_c}{\Delta x^2} + \frac{V_P^2}{D_c} + \frac{V_P}{\Delta x} + \lambda_c + \beta\right)\rho_{c,L} + \alpha\rho_{s,L} \\
\left.\frac{d\rho_s}{dt}\right|_L &= \frac{D_s}{\Delta x^2}\rho_{s,L-1} - \left(\frac{D_s}{\Delta x^2} + \lambda_s + \alpha\right)\rho_{s,L} + \beta\rho_{c,L} - \eta\rho_{s,L}(\omega - \rho_{psd,L)+\gamma\rho_{psd,L}}.
\end{aligned}$$

Next, I used the scipy.solve_ivp function to compute ρ_c and ρ_s with the explicit Runge-Kutta method of order 5(4).

A.8. Trafficking dynamics and steady state distribution of CNIH-2 mRNA

The production, degradation, and transport dynamics of *Cnih2* mRNA molecules can be described by the model proposed in [58]

$$\frac{\partial R_{CNIH-2}(x,t)}{\partial t} = D_R \frac{\partial^2 R_{CNIH-2}(x,t)}{\partial x^2} - v_R \frac{\partial R_{CNIH-2}(x,t)}{\partial x} - k_R R_{CNIH-2}(x,t). \quad \text{(A.15)}$$

First, I determine the steady state distribution for the equation Eq. A.15. Setting the time-derivative to 0, I obtain

$$0 = D_R \frac{d^2 R_{CNIH-2}(x)}{dx^2} - v_R \frac{dR_{CNIH-2}(x)}{dx} - k_R R_{CNIH-2}(x). \quad \text{(A.16)}$$

The general solution, $R^{Den}_{CNIH2-ss}$, of the equation Eq. A.16 reads

$$R^{Den}_{CNIH2-ss}(x) = C_1 e^{-\lambda_{R1} x} + C_2 e^{-\lambda_{R2} x} \quad \text{(A.17)}$$

where $\lambda_{R1,2} = (-v_R \pm \sqrt{v_R^2 + 4 D_R k_R})/(2 D_R)$.

We calculate the constants C_1, C_2 using the following boundary conditions:

$$\begin{aligned} v_R R_{CNIH-2} - D_R \frac{dR_{CNIH-2}}{dx}\bigg|_0 &= (v_R + D_R\lambda_{R1})C_1 + (v_R + D_R\lambda_{R2})C_2 = -J_{Rin} \\ v_R R_{CNIH-2} - D_R \frac{dR_{CNIH-2}}{dx}\bigg|_L &= (v_R + D_R\lambda_{R1})C_1 e^{-\lambda_{R1}L} + (v_R + D_R\lambda_{R2})C_2 e^{-\lambda_{R2}L} = 0, \end{aligned} \quad \text{(A.18)}$$

and derive the steady state distribution $R^{Den}_{CNIH2-ss}(x)$. Here J_{Rin} is the constant rate of influx of mRNA from soma into the dendrite. The second boundary condition describes the no-flux boundary condition. We obtain

$$\begin{aligned} R^{Den}_{CNIH2-ss}(x) = &\left(\frac{J_{Rin} e^{-\lambda_{R2}L}}{(v_R + D_R\lambda_{R1})(e^{-\lambda_{R1}L} - e^{-\lambda_{R2}L})} \right) e^{-\lambda_{R1} x} \\ &+ \left(\frac{J_{Rin} e^{-\lambda_{R1}L}}{(v_R + D_R\lambda_{R2})(e^{-\lambda_{R2}L} - e^{-\lambda_{R1}L})} \right) e^{-\lambda_{R2} x}. \end{aligned} \quad \text{(A.19)}$$

A.9. Trafficking dynamics and steady state distribution of CNIH-2 protein

The CNIH-2 protein model considers the CNIH-2 somatic translation rate, local dendritic translation rate, diffusion, and active transport. Hence, I can use the protein trafficking model introduced in [58] for CaMK2a protein to model the CNIH-2 protein dynamics. I obtain

$$\frac{\partial \rho_{CNIH-2}(x,t)}{\partial t} = D_P \frac{\partial^2 \rho_{CNIH-2}(x,t)}{\partial x^2} - v_P \frac{\partial \rho_{CNIH-2}(x,t)}{\partial x} - k_P \rho_{CNIH-2}(x,t) + \beta_P R^{Den}_{CNIH2-ss}(x). \tag{A.20}$$

First, I determine the steady state of the equation Eq. A.20 by setting the time-derivative to 0

$$0 = D_P \frac{d^2 \rho_{CNIH-2}(x)}{dx^2} - v_P \frac{d\rho_{CNIH-2}(x)}{dx} - k_P \rho_{CNIH-2}(x) + \beta_P R^{Den}_{CNIH2-ss}(x). \tag{A.21}$$

The general solution $P^{Den}_{CNIH2-ss}$ of the equation Eq. A.21 reads

$$P^{Den}_{CNIH2-ss}(x) = C_1 e^{-\lambda_{P1} x} + C_2 e^{-\lambda_{P2} x} + C_3 e^{-\lambda_{R1} x} + C_4 e^{-\lambda_{R2} x} \tag{A.22}$$

whereby

$$\begin{aligned}
\lambda_{P1/2} &= \frac{-v_P \pm \sqrt{v_P^2 + 4 D_P k_P}}{2 D_p} \\
C_3 &= \frac{-\beta_P J_{Rin} e^{-\lambda_{R2} L}}{(D_P \lambda_{R1}^2 + v_P \lambda_{R1} - k_P)(v_R + D_R \lambda_{R1})(e^{-\lambda_{R1} L} - e^{-\lambda_{R2} L})} \\
C_4 &= \frac{-\beta_P J_{Rin} e^{-\lambda_{R1} L}}{(D_P \lambda_{R2}^2 + v_P \lambda_{R2} - k_P)(v_R + D_R \lambda_{R2})(e^{-\lambda_{R2} L} - e^{-\lambda_{R1} L})}
\end{aligned}$$

We use the following boundary conditions to obtain the constants C_1 and C_2 in Eq. Eq. A.22

$$\begin{aligned}
v_P \rho_{CNIH-2} - D_P \frac{d\rho_{CNIH-2}}{dx}\bigg|_0 &= (v_P + D_P \lambda_{P1}) C_1 + (v_P + D_P \lambda_{P2}) C_2 \\
&\quad + (v_P + D_P \lambda_{R1}) C_3 + (v_P + D_P \lambda_{R2}) C_4 = -J_{Pin} \\
v_P \rho_{CNIH-2} - D_P \frac{d\rho_{CNIH-2}}{dx}\bigg|_L &= (v_P + D_P \lambda_{P1}) C_1 e^{-\lambda_{P1} L} + (v_P + D_P \lambda_{P2}) C_2 e^{-\lambda_{P2} L} \\
&\quad + (v_P + D_P \lambda_{R1}) C_3 e^{-\lambda_{R1} L} + (v_P + D_P \lambda_{P2}) C_4 e^{-\lambda_{R2} L} = 0
\end{aligned} \tag{A.23}$$

The final steady state CNIH2 protein distribution reads

$$
\begin{aligned}
\rho^{SS}_{Cnih2}(x) = & \\
& - \left(\frac{\frac{(v_P+D_P\lambda_{R1})\beta_P}{D_P\lambda_{R1}^2+v_P\lambda_{R1}-k_P}\left(e^{-\lambda_{P2}L}-e^{-\lambda_{R1}L}\right)+J_{Pin}e^{-\lambda_{P2}L}}{(v_P+D_P\lambda_{P1})(e^{-\lambda_{P1}}-e^{-\lambda_{P2}L})} \right. \\
& \left. + \frac{\frac{(v_P+D_P\lambda_{R2})\beta_P}{D_P\lambda_{R2}^2+v_P\lambda_{R2}-k_P}\left(e^{-\lambda_{P2}L}-e^{-\lambda_{R2}L}\right)}{(v_P+D_P\lambda_{P1})(e^{-\lambda_{P1}}-e^{-\lambda_{P2}L})} \right) e^{-\lambda_{P1}x} \\
& + \left(\frac{\frac{(v_P+D_P\lambda_{R1})\beta_P}{D_P\lambda_{R1}^2+v_P\lambda_{R1}-k_P}\left(e^{-\lambda_{P1}L}-e^{-\lambda_{R1}L}\right)+J_{Pin}e^{-\lambda_{P1}L}}{(v_P+D_P\lambda_{P2})(e^{-\lambda_{P1}}-e^{-\lambda_{P2}L})} \right. \\
& \left. + \frac{\frac{(v_P+D_P\lambda_{R2})\beta_P}{D_P\lambda_{R2}^2+v_P\lambda_{R2}-k_P}\left(e^{-\lambda_{P1}L}-e^{-\lambda_{R2}L}\right)}{(v_P+D_P\lambda_{P2})(e^{-\lambda_{P1}}-e^{-\lambda_{P2}L})} \right) e^{-\lambda_{P2}x} \\
& - \frac{-\beta_P J_{Rin}e^{-\lambda_{R2}L}}{(D_P\lambda_{R1}^2+v_P\lambda_{R1}-k_P)(v_R+D_R\lambda_{R1})(e^{-\lambda_{R1}L}-e^{-\lambda_{R2}L})}e^{-\lambda_{R1}x} \\
& - \frac{-\beta_P J_{Rin}e^{-\lambda_{R1}L}}{(D_P\lambda_{R2}^2+v_P\lambda_{R2}-k_P)(v_R+D_R\lambda_{R2})(e^{-\lambda_{R2}L}-e^{-\lambda_{R1}L})}e^{-\lambda_{R2}x}.
\end{aligned}
\tag{A.24}
$$

A.10. Time-dependent solution of CNIH-2 subunit trafficking model

How does the concentration of CNIH-2 evolve in our model dendrite over time? To calculate the spatiotemporal distribution of CNIH-2 protein ($\rho_{CNIH-2}(x,t)$), I return to the original partial differential equation of CNIH-2 Eq. A.20. To simulate the spatiotemporal dynamics of CNIH-2 during basal state and upon cLTP induction, I first discretized the spacial variable (x) of the model and converted PDE to a time-dependent ODE

$$\frac{d\rho_{CNIH-2}}{dt} = D_P\left(\frac{\rho_{CNIH-2,i+1} - 2\rho_{CNIH-2,i} + \rho_{CNIH-2,i-1}}{\Delta x^2}\right) - v_P\left(\frac{\rho_{CNIH-2,i+1} - \rho_{CNIH-2,i}}{\Delta x}\right) - k_P\rho_{CNIH-2,i} + \beta_P R^{Den}_{CNIH-2-ss,i}.$$

I computed coefficients corresponding to P_i, P_{i-1} and P_{i+1} and rewrote the last equation as

$$\frac{d\rho_{CNIH-2}}{dt} = \left(\frac{D_P}{\Delta x^2} - \frac{v_P}{\Delta x}\right)\rho_{CNIH-2,i+1} - \left(\frac{2D_P}{\Delta x^2} - \frac{v_P}{\Delta x} + k_P\right)\rho_{CNIH-2,i} + \left(\frac{D_P}{\Delta x^2}\right)\rho_{CNIH-2,i-1} + \beta_P R^{Den}_{CNIH-2-ss,i} \tag{A.25}$$

Now I could determine P at all intermediate nodes ($i = 1, ...L-1$) except the boundary nodes $i = 0, L$. For the boundary nodes, I used boundary conditions at $x = 0$ and $x = L$

$$D_P\frac{\rho_{CNIH-2,0} - \rho_{CNIH-2,-1}}{\Delta x} - v_P\rho_{CNIH-2,0} = -J_{pin}$$
$$D_P\frac{\rho_{CNIH-2,L+1} - \rho_{CNIH-2,L}}{\Delta x} - v_P\rho_{CNIH-2,L} = 0.$$

and determined the temporal evolution of the CNIH-2 protein at the boundary points and obtained the differential equations

$$\left.\frac{d\rho_{CNIH-2}}{dt}\right|_0 = \left(\frac{D_P}{\Delta x^2} - \frac{v_P}{\Delta x}\right)\rho_{CNIH-2,1} - \left(\frac{D_P}{\Delta x^2} + k_P\right)\rho_{CNIH-2,0} + \frac{J_{Pin}}{\Delta x} + \beta_P R^{Den}_{CNIH-2-ss,0} \tag{A.26}$$

$$\left.\frac{d\rho_{CNIH-2}}{dt}\right|_L = \left(\frac{D_P}{\Delta x^2}\right)\rho_{CNIH-2,L-1} - \left(\frac{D_P}{\Delta x^2} + \frac{v_P^2}{D_P} - \frac{v_P}{\Delta x} + k_P\right)\rho_{CNIH-2,L} + \beta_P R^{Den}_{CNIH-2-ss,L}. \tag{A.27}$$

Finally, I used the $solve\_ivp$ function of the scipy Python library to integrate the ODEs in Eqs. (Eq. A.25 - Eq. A.27) and calculated $\rho_{CNIH-2}(x,t)$.

A.11. CNIH-2 local-translation upregulation upon plasticity and exocytosis of GluA2-containing AMPARs

For simulating chemical LTP-driven, I step-increased the local translation rate (β_P) to 500 times the basal rate throught the model dendrite. This step increase lasted for 10 minutes (in case of brief stimulation) 2 hours (in case of prologned stimulation). I chose the duration of prologned stimulation based on the previous reports of translation up-regulation, which peaks at 30 minutes and is observable at 2 hours following LTP induction [28, 130]. After simulation time, the local translation rate was reset to the basal level. For increased somatic flux simulation, I increased the in-flux rate J_{pin} to 500 times the basal influx. Again, after 2 hours of simulation time, I reset the influx to baseline.

Next, I considered the local concentration of CNIH-2, a direct regulator of GluA2-containing AMPAR exocytosis. Hence, for plasticity simulations, the AMPAR exocytosis rate is changed proportional to the change in CNIH-2 concentration. More precisely, I normalized the CNIH-2 concentration after plasticity induction by the baseline concentration of CNIH-2 and multiplied it by the basal exocytosis rate.

$$\beta(x,t) = \beta(x,0) \times \frac{\rho_{CNIH-2}(x,t)}{\rho^{ss}_{CNIH-2}(x)} \tag{A.28}$$

Here, $\beta(x,t)$ is the value of the rate of exocytosis across the full dendrite over the complete simulation time.

A.12. Fitting models to the data

▶ Fitting mRNA data

To estimate the drop in *Gria1*, *Gria2*, *Cnih2* and *CamK2a* mRNA density along a dendritic branch, I performed automatic optimization of the binned empirical data (bin size = 7.5 μm)

and an exponential function of the form $f(x) = A * e^{-Bx}$, where f represents the distribution of the mRNA along a line dendrite. Independent variable x corresponds to the location on the dendrite. I fitted the A (> 0) and B (> 0) *minimize* function of *lmfit* python package for nonlinear least square minimization between the data and the model prediction.

▶ Fitting paramters for total GluA2 model

I automatically optimized the first 100 μm dendritic distribution over the two-dimensional parameter space (diffusion rate D and active transport velocity V) to fit the experimental data. For both experimental data and model, a binning (bin size = 5 μm) and normalization by the first bin value were done before the optimization. The fitting was done using the *minimize* function of *lmfit* python package for nonlinear least square minimization between the data and the model. I note that in all of my simulations, I assumed the length of the model dendrite to be $L = 500\mu m$ and then performed the fitting.

▶ Exocytosis rate for the extended model

To calculate the net exocytosis rate at a steady state, I computed the ratio of total surface GluA2 fluorescence ($\int_0^L \rho_s(x)dx$) to the total intracellular GluA2 fluorescence ($\int_0^L \rho_c(x)dx$). As per my calculations below, this ratio is equal to the ratio of the rate of exocytosis to endocytosis. The following proof shows that this ratio is indeed equal to the ratio between the exocytosis and endocytosis rates (β/α). Integrating the steady-state solution in Eq. A.11 from 0 to L, I obtain

$$0 = \left[D_c \frac{\partial \rho_c}{\partial x} - V_p \rho_c\right]\Big|_0^L + \alpha \int_0^L \rho_s dx - (\beta + \lambda_c) \int_0^L \rho_c dx \tag{A.29}$$

$$0 = \left[D_s \frac{\partial \rho_s}{\partial x}\right]\Big|_0^L - (\alpha + \lambda_s) \int_0^L \rho_s dx + \beta \int_0^L \rho_c dx \tag{A.30}$$

Using the boundary conditions from (Eq. A.13 - Eq. A.14), I obtain

$$\int_0^L \rho_c dx = \frac{J_{cin}}{\lambda_c} \quad \int_0^L \rho_s dx = \frac{\beta J_{cin}}{\alpha \lambda_c}$$

Hence, I compute the ratio between the exocytosis and endocytosis rates

$$\frac{\beta}{\alpha} = \frac{\int_0^L \rho_s dx}{\int_0^L \rho_c dx} \tag{A.31}$$

Here, I used the endocytosis rate as described in Table A.4. For the GluA1-homomer version of the model, I used a ratio of 1.7 to obtain the exocytosis rate. This ratio was reported in [59].

► **Fitting D_s, D_c and V_P for full GluA2 model**

The exocytosis rate was calculated using the above-mentioned method before fitting the global transport parameters, D_S, D_c, and V_P, which were optimized as mentioned above for the total GluA2 model. In Fig. A.2.A, I show the best-fitted distribution against experimental data and compare it against the upper and lower values of the diffusion and active transport parameters. In Fig. A.2.B-.D, I show the distribution in the full length of $500\mu m$. The best-fitted model showed an $\approx$ 250% increase in dendritic concentration at the dendritic tip. As expected, a fast diffusion rate and active transport lead to a huge accumulation towards the distal tip In Fig. A.2.C. Whereas a purely diffusive transport led to a fast decay of concentration such that the concentration dropped to 0 at $\approx 300\mu m$.

► **Fitting η for three population GluA2 model**

First, I fixed all the other parameters in my model and then estimated the parameter η. To fit the incorporation rate η in my three population model, I calculated the mean ratio of ρ_{psd} and ρ_s over the first 60μm length of the model used $minimize$ function to reduce the difference between this ratio and the mean surface synaptic enrichment calculated from the data.

► **Baseline model of GluA1-homomeric AMPARs**

To generate the steady-state trafficking dynamics of GluA1-containing AMPARs, I used the three population models described using the partial differential equations described in Eq. 3.6-Eq. 3.8 and used values for transport parameters based on previous models of SEP-GluA1, described in Table A.5.

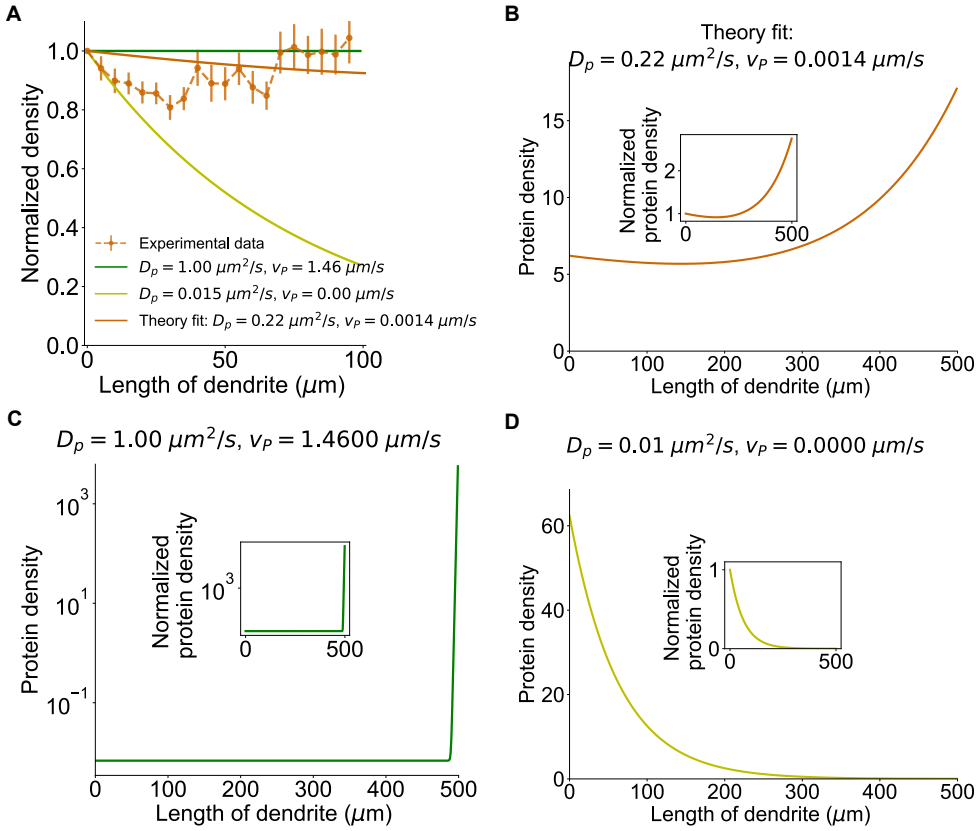

Figure A.2.: **Fitting of GluA2 model to experimental data**

A) Binned distribution of Glua2 subunit of AMPAR, slow and fast transport distribution, and theory fit distribution. **B)-D)** steady-state, dendritic distribution of Glua2-containing AMPAR (surface+intracellular) for three different sets of transport parameters. The degradation and the somatic flux parameters were set to $\lambda_P = 2.57 * 10^{-6}\ s^{-1}$, $J_{Pin} = 0.01$ proteins/s. The insets contain the dendritic concentration normalized at the starting point of the primary dendrite ($x = 0$). The figure is adapted from [178]

A.13. Estimation of trafficking parameters from published live-cell fluorescent imaging data

► **Endocytosis rates under basal condition**

Live-cell studies investigating receptor internalization, report endocytosis frequency in units of events per μm^2 per minute, as endocytosis is thought of a sudden loss of fluorescent intesity of surface receptor. For more details, see [135].

I converted the endocytosis frequency to a rate per second unit for my model. For this, I multiplied the reported frequency by the number/concentration of receptors per vesicle and the area of the ROIs.

[135] report endocyotis frequency as $2.5 \pm 0.4 * 10^{-3}$ events $\mu m^{-2} min^{-1}$ for GluA2 and $2.1 \pm 1.1 * 10^{-3}$ events $\mu m^{-2} min^{-1}$ for GluA1 AMPAR. They measured this frequency in a circular ROI of radius 300 nm. Also, the estimated number of AMPARs per vesicle is 50 [110, 6]. using these values, I obtained the mean endocytosis rates:

$$\frac{2.5 * 10^{-3} * \pi * (0.3)^2 * 50}{60} = 5.89 * 10^{-4} s^{-1}$$
$$\frac{2.1 * 10^{-3} * \pi * (0.3)^2 * 50}{60} = 4.94 * 10^{-4} s^{-1}$$

for GluA2 and GluA1 AMPA receptors, respectively.

A.14. Experimental procedures

A detailed description of the methods used to prepare the hippocampal cultures, see [12, 1, 167]. Since the data were acquired on mouse and rat neurons from two different collaborations, I am providing the details on the experiments for them separately.

► **mouse cultured hippocampal neurons**

Dissociated hippocampal neuron cultures were prepared from embryonic day E16.5-18.5 mouse embryos (C57Bl/6N; Charles River Laboratories). The hippocampi were dissected in pre-chilled dissection medium (Hanks balanced salt solution (HBSS) with 1% GlutaMax, 1% HEPES, 1% Pen/Strep), digested in 1ml Papain for 15min at 37řC, washed twice in pre-warmed DMEM

medium (Dulbeccos modified Eagle medium (DMEM) with 10% fetal bovine serum (FBS)) and twice in pre-warmed NB+ medium (Neurobasal medium supplemented with 2mM Glutamax, 77.7mM D-Glucose). Neurons were then gently dissociated with a fire-polished Pasteur pipette, centrifuged for 5min at 71 g, and finally plated at $30 - 40$ x 10^3 $cells/cm^2$ on poly-D-lysine coated coverslips placed in a 24-well plate. Neurons were kept in NB++ medium (Neurobasal medium supplemented with 2mM Glutamax, 77.7mM D-Glucose, and 1:50 B27) at 37řC and 5% CO2 for 14 days until fixation. Animal experiments were approved by the Hessian authorities.

► **Transfection**

For subsequent staining, neurons were transfected with a plasmid expressing GFP at 11 days in vitro (DIV) using calcium phosphate transfection. Neurons were transfected by adding 15ţl 2x HeBs buffer (274mM NaCl, 10mM KCl, 1.4mM Na_2HPO_4 x $7H_2O$, 15mM D-Glucose, 42mM HEPES) with 15ţl DNA and calcium solution (2 ţg of DNA in 250 mM $CaCl_2$ solution) per well at DIV11 after plating. The conditioned culture medium was replaced with 400 ţl of NB+ medium before adding the DNA mixture. After incubation for 10 min at 37řC under 5% CO_2, the neurons were washed three times with NB+, which had been pre-incubated at 37řC under 5% CO_2, and the conditioned NB++ medium was added back to the cells.

► **Immunostaining, image acquisition and analysis.**

Coverslips with attached neurons (DIV 14) were washed and fixed once at room temperature DPBS containing calcium and magnesium before being fixed in 4% paraformaldehyde in PBS (pH = 7.4) containing 4% of sucrose for 10 minutes on ice. Afterward, neurons were washed with NH4Cl for 10 min on ice, blocked in blocking buffer (2% BSA/4% NDS/PBS) for 30 min at room temperature, and incubated over three days with mouse anti-GluA2 antibody (1:500, Millipore) at 4řC and labeled with donkey-anti-mouse Cy3 (1:500, Jackson Immuno Research) overnight at 4řC. For the visualization of extra- and intracellular GluA2, neurons were subsequently permeabilized for 5 min in 0.4% Triton X-100 in PBS, blocked for 30 min, incubated overnight with the same mouse anti-GluA2 (1:500) and chicken anti-GFP (1:1000, Abcam), and labeled with donkey anti-mouse Cy5 (1:500, Jackson Immuno Research) and donkey anti-chicken Alexa 488 (1:500, Jackson Immuno Research) overnight at 4řC. Image acquisition.

Hippocampal neurons were imaged using Leica TCS SP5 confocal microscopes and 63x oil objectives (NA 1.4). Z stacks spanning the entire volume of neurons were obtained, and channels were separated and collapsed to a sum intensity projection in ImageJ. Manual annotation of the dendritic tree using a segmented line tool and somata using polygonal ROIs was performed. The signal intensity profile in dendritic ROIs was measured using a constant width, and integrated density was calculated for somatic ROIs.

► **Rat cultured neurons.**

Please see [1] for details on obtaining dissociated rat hippocampal cultures. Briefly, dissected hippocampi from postnatal day 0-1 rat pups of either sex (Sprague-Dawley strain; Charles River Laboratories) were obtained and dissociated with papain (Sigma) and plated at a density of 40×10^3 cells/cm^2 on poly-D-lysine coated glass-bottom Petri dishes (MatTek). Neurons were maintained and matured in a humidified atmosphere at 37řC and 5% CO_2 in growth medium (Neurobasal-A supplemented with B27 and GlutaMAX-I, life technologies) for 18-21 days in vitro (DIV) to ensure synapse maturation. All experiments complied with national animal care guidelines and the guidelines issued by the Max Planck Society and were approved by local authorities. For transfection, DIV7-11 neurons were transfected using Effectene (Qiagen), as previously described. Transfected cells were maintained until DIV19 for experiments.

► **In situ hybridization in cultured neurons.**

Using the QuantiGene ViewRNA kit from Affymetrix (now Thermo Fisher Scientific), mostly following the provider's instructions, in situ hybridization was performed. Briefly, cells at DIV 18-24 were fixed for 20 min at room temperature using a 4% paraformaldehyde (PFA) solution (4% paraformaldehyde, 2.5% Sucrose, in lysine-phosphate buffer). The Proteinase K treatment was omitted to preserve the integrity of the dendrites. After permeabilization using the provider's detergent buffer for 2 min, cells were directly incubated for 3h at 40řC with detection probes. Incubations with pre-amplification, amplification, and detection probes were reduced to 40 minutes each. After completion of in situ hybridization, cells were washed with PBS and incubated in blocking buffer (4% goat serum in PBS) for 1hr. Neurons were subsequently processed for immunofluorescence using standard methods as described below.

► **Immunofluorescence in cultured neurons.**

All steps were performed at room temperature unless stated otherwise. Glass bottom dishes with attached neurons (DIV 18-21) were fixed in paraformaldehyde 4% in lysine phosphate buffer pH 7.4 containing 2.5% sucrose for 15-20 min. For simple immunofluorescence, neurons were permeabilized for 10 min in PBS + 0.5% Triton-X 100. After 2 quick washes in PBS, neurons were incubated in a blocking buffer (4% goat serum in PBS) for 30 min. Then, the neurons were incubated for 1 hr or overnight with primary antibodies, and after 3 washes of 5 min, they were incubated for 1.5 hr with secondary antibodies. We used the following antibodies: guinea pig anti-MAP2 (Synaptic Systems, 1:2000), mouse anti-biotin (Sigma, 1:1000), rabbit anti-biotin (Cell Signaling, 1:1000), mouse anti-Puromycin (Kerafast, 1:2500), homemade rabbit anti-Puromycin (1:250), homemade anti-GluA1 N-terminal domain (targeted sequence QWRTSDSRDHTRVDWKRPKC; KO validated by western blot) (fixed sample 1/500; live-labeling 1/200), mouse anti-GluA2 N-terminal domain from Eric Gouaux previously used in Nair et al., 2013 (fixed sample 1/100; live-labeling 1/500), rabbit anti-CNIH-2 (Synaptic Systems, 1/200), homemade rabbit anti-TARP Gamma-8 C-terminal domain (targeted sequence PGTLSKEAAASNTNT, 1/200; the antibody staining co-localizes with synaptic protein Bassoon and shows strong extrasynaptic labeling).

► **Chemical long-term potentiation (cLTP).**

The original medium of cultured neurons was replaced for 5 min by artificial cerebrospinal fluid (ACSF) at 37řC to induce chemical LTP. In the control condition, the ACSF contained Ca2+ (2 mM) and Mg2+ (2 mM) and was supplemented with B27 and MEM Amino Acids (50X) (Thermo Fisher Scientific). In the cLTP-induction condition, the ACSF differed from the control-ACSF as follows: Ca2+ (3 mM), Mg2+ (0 mM), glycine (200 μM), picrotoxin (100 μM). After the 5 min induction, the cells were placed in a growth medium containing either methionine (Met) or L-Azidohomoalanine (AHA) at 4 mM for 1 hr.

► **Fluorescence non-canonical amino acid tagging.**

To investigate the distribution of newly synthesized proteins, we used a recently developed method combining fluorescence non-canonical amino acid tagging with the proximity ligation assay (FUNCAT-PLA) [167]. Cultured neurons were incubated for 1 hr with a growth medium,

where met was replaced by AHA (4 mM). In control conditions, the growth medium contained Met (4 mM) and no AHA.

► **Puromycylation.**

The sites of synthesis of AMPAR components were determined utilizing a recently developed method combining puromycylation and proximity ligation assay (Puro- PLA) [167]. Cultured neurons were labeled with 10 μM puromycin (Sigma- Aldrich) for 2 min. In control experiments, cells were treated with 40 μM of the protein synthesis inhibitor anisomycin (Sigma-Aldrich) for 30 min prior to and during puromycin labeling.

► **Proximity ligation assay.**

Anti-puromycin or anti-biotin antibodies (in case of AHA metabolic labeling) in combination with protein-specific antibodies against our proteins of interest were used for the detection of newly synthesized proteins by proximity ligation ([167]). We utilized Duolink reagents (Sigma) and adhered to the protocol provided by the manufacturer with some modifications described below. We periodically used rabbit PLAplus and mouse PLAminus probes amplification and label probe binding. Briefly, after we washed the primary antibodies 3 times in PBS, PLA probes were applied in 1:10 dilution in PBS with 4% goat serum for 1 h at 37 řC, washed several times with wash buffer A (0.01 M Tris, 0.15 M NaCl, 0.05% Tween 20) and incubated for 30 min with the ligation reaction containing the circularization oligos and T4 ligase prepared according to the manufacturer's recommendations (Duolink Detection reagents Red, Sigma) in a prewarmed humidified chamber at 37řC. Amplification and label probe binding were performed after further washes with wash buffer A with the amplification reaction mixture containing Phi29 polymerase and the fluorophore-labeled detection oligo prepared according to the manufacturer's recommendations (Duolink Detection reagents Red, Sigma) in a prewarmed humidified chamber at 37 řC for 100 min. Amplification was stopped by three washes in wash buffer B (0.2 M Tris, 0.1 M NaCl, pH 7.5). For better signal stability, cells were kept in wash buffer B at 4řC until imaging.

► **Image acquisition and analysis.**

images of the cultured cells were acquired using Zeiss LSM780/880 confocal microscopes using a 63x oil objective NA 1.4 and a 40x oil objective NA 1.3. Z-stacks spanning the entire volume of imaged neurons were obtained.

A.15. List of abbreviations

AIS Axon initial segment 1

AMPAR α-amino-3-hydroxy-5-methyl-4-isoxazolepropionic acid receptor iii

ANN Artificial Neural Network 20

CaMK2a Ca2+ calmodulin-dependent protein kinase II 8

CNIH-2 Cornichon family AMPA receptor auxiliary protein 2 iv

CNS Central Nervous System 3

FISH Fluorescence *in situ* hybridization 28

FRAP Fluorescence recovery after photobleaching 8

FUNCAT Fluorescence non-canonical amino acid tagging 9

GUI Graphical User Interface 20

LTD Long-term depression 6

LTP Long-term potentiation 6

ODE Ordinary differential equation 45

PDE Partial differential equation 45

PLA Proximation ligation assay 9

PP1 Protein phosphatase 1 85

PNS Peripheral Nervous System 3